

University of Denver

Digital Commons @ DU

Electronic Theses and Dissertations

Graduate Studies

1-1-2019

Synergistic Environmental Aging of Glass Reinforced Polymer Composites

Tianyi Lu
University of Denver

Follow this and additional works at: <https://digitalcommons.du.edu/etd>



Part of the [Materials Science and Engineering Commons](#)

Recommended Citation

Lu, Tianyi, "Synergistic Environmental Aging of Glass Reinforced Polymer Composites" (2019). *Electronic Theses and Dissertations*. 1674.

<https://digitalcommons.du.edu/etd/1674>

This Dissertation is brought to you for free and open access by the Graduate Studies at Digital Commons @ DU. It has been accepted for inclusion in Electronic Theses and Dissertations by an authorized administrator of Digital Commons @ DU. For more information, please contact jennifer.cox@du.edu, dig-commons@du.edu.

SYNERGISTIC ENVIRONMENTAL AGING OF GLASS REINFORCED POLYMER
COMPOSITES

A Dissertation

Presented to

the Faculty of the Daniel Felix Ritchie School of
Engineering and Computer Science
University of Denver

In Partial Fulfillment

of the Requirements for the Degree

Doctor of Philosophy

by

Tianyi Lu

August 2019

Advisor: Dr. Maciej Kumosa

©Copyright by Tianyi Lu 2019

All Rights Reserved

Author: Tianyi Lu
Title: SYNERGISTIC ENVIRONMENTAL AGING OF GLASS REINFORCED
POLYMER COMPOSITES
Advisor: Dr. Maciej Kumosa
Degree Date: August 2019

Abstract

Synergistic effects involved in the environmental degradation of Glass Reinforced Polymer (GRP) composites were examined and a novel synergistic aging model was proposed in this study. Six GRPs based on glass fibers with four different polymer resins and six pure polymer thermoplastic resins were exposed either individually or in combination to ultraviolet (UV) radiation, water condensation and elevated temperature for approximately 1000 h. The composites and polymers were monitored for weight changes as a function of time and their surfaces were examined after the tests using optical and scanning electron microscopes (SEM). Photodegradation of the polymer matrices was analyzed by Fourier Transform Infrared Spectroscopy (FTIR) techniques. A comparison of weight changes of polymer composites degraded by UVA and UVB was also presented.

It has been shown that the selected aging conditions created noticeable synergistic effects causing extensive erosion of the polymer matrices of the tested composites which appeared to be much stronger under the combined actions than under individual exposures. However, synergetic aging of pure polymers was not as obvious as in the tested GRPs with the exception of the PVC resin. Based on the synergistic aging mechanisms observed on the surfaces of the tested GRPs, a new model of synergistic aging of polymers under UV and water condensation was proposed. The model includes numerical simulations of UV radiation, numerical simulations of hydrodynamic effects,

and complex particle removal analyses. In the UV radiation modelling part of the simulations, flat and sinusoidal polymer surfaces were numerically modeled for their UV damage as a function of UV intensity, surface topography, and exposure time. The results showed that UV damage on uneven polymer surfaces reduces their surface roughness making them planar and that the degradation rates are the largest at the tips of the local heights of the surfaces. This was subsequently verified experimentally by exposing neat epoxy specimens to UV and by precisely monitoring their surface topography as a function of time. In the hydrodynamic portion, viscous shear stresses generated by slowly moving water were determined on uneven polymer surfaces as a function of surface morphology, flow rates, and volumetric forces.

In the particle removal portion of the analysis, a new micro-particle removal mechanism was suggested by comparing the adhesion forces calculated using the Johnson-Kendall-Roberts (JKR) model and the Hamaker approach with the drag forces created by slow water flows. Subsequently, the particle removal mechanism was verified on an inclined unidirectional glass/epoxy surface with randomly distributed epoxy particles subjected to a gravitational flow of water. It has been shown that the movement of polymer particles on polymer/composite surfaces depends very strongly on particle sizes, water velocity and surface morphology.

The analysis of adhesion forces between particles and polymer surfaces was further enhanced by introducing the surface roughness effects for both the polymer surfaces and the particles. The interactions were simulated by using the Rumpf, Rabinovich, Kumar, and the modified Rabinovich models as a function of nano roughness and micro roughness of substrate surfaces, nano roughness of micro roughness

of particles, particle size and the number of contact points. Adhesion forces between irregular particles and irregular surfaces were also analyzed for their effects on the critical sizes of particle which could be removed from different rough surfaces by shear stresses generated by slowly moving water. It has been shown that the polymer surfaces with irregular nano/micro structure characteristics significantly reduced their interactions with deposited rough particles. The critical sizes of rough particles that could be removed by water flows were found to be significantly smaller than for smooth particles removed from flat surfaces.

Acknowledgements

Though only my name appears on the cover of this dissertation, many people have contributed to this work. I owe my gratitude to all those people who have made this dissertation possible and because of whom my graduate experience has been one that I will cherish forever.

My deepest gratitude is to my advisor, Professor Maciej Kumosa for the continuous support of my Ph.D. I have been amazingly fortunate to have a guide who gave me the freedom to explore on my own and at the same time, the guidance to recover when my steps faltered. His patience and support helped me overcome many crisis situations and to finish my dissertation. I would like to express my appreciation to Professor Yun-bo Yi for his invaluable guidance. He has been always there to listen and give advices. I am deeply grateful to him for the long discussions that helped me sort out the technical details of my modeling work.

I would like to thank all my lab colleagues for their valuable guidance. I would particularly like to single out my friend, Dr. Euripides Solis-Ramos, I want to thank you for your excellent cooperation and for all of the SEM assistance I was given to complete my research and further my dissertation. I would also like to express my sincere thanks to Dr. Paul Predecki for his insightful comments and constructive criticisms in polymer field. Last but not least, I would also like to thank my parents for their wise counsel and sympathetic ear. You are always there for me. Also, thanks so much to my friends (Jian Qiu, Sabuj Khadk, Bruce Allen, etc.). We were not only able to support each other by deliberating over our problems and findings, but also happily by talking about things other than just our research.

Table of Contents

Abstract	ii
Chapter 1: General Introduction	1
Chapter 2: Literature Review.....	6
2.1 Introduction to composites and their aging issues	7
2.1.1 Glass fiber-reinforced polymer matrix composites.....	8
2.1.2 Polymer composite degradation.....	14
2.2 Environmental aging of polymers and PMCs.....	18
2.2.1 Experimental aging of polymer materials.....	19
2.2.2 Environmental aging models of polymer materials	24
2.4 Thesis statement.....	32
2.5 Publications.....	33
2.6 Disclaimer.....	35
Chapter 3. Synergistic Environmental Degradation of Glass Reinforced Polymer Composites.....	37
3.1 Previous work	37
3.2 Introduction.....	38
3.4 Environmental testing and analysis	39
3.5. Tested composites and specimen preparation.....	41
3.6 Aging results and discussions	42
3.6.1 Surface erosion.....	42
3.6.2 Mass changes	45
3.7 Synergistic aging effects in GRPs.....	48
3.7.1 Comparison between individual and combined exposures	48
3.7.2 Summary observations of surface degradation of all tested GRP composites under synergistic aging	50
3.7.3 Summary of chemical reactions during synergistic aging of polymers	52
3.7.4 Preliminary synergistic aging model	54
3.8 Comparison of degradation by UVB and UVA	55
3.9 Surface yellowing	56
3.10 Summary	57
Chapter 4. Polymer Degradation under UV and Water Condensation	59
4.1 Polymer photodegradation	59
4.1.1 FTIR analysis on selected GRPs.....	60
4.1.2 Possible photodegradation mechanisms in VE polymer under UV. 63	
4.2 Synergistic aging of pure polymers	65
4.5 Summary	67
Chapter 5. UV Degradation Model for Polymers and Polymer Matrix Composites	69

5.1 Introduction.....	70
5.2 Fundamentals of proposed UV degradation model	72
5.3 Experimental estimation of UV damage parameters	77
5.4 Simulations of UV radiation on polymeric surfaces.....	82
5.4.1 Radiation angle effect on flat surfaces.....	82
5.4.2 UV radiation damage of sinusoidal surfaces	83
5.4.3 Surface amplitude and frequency shape effects.....	87
5.5 Verification of the proposed UV degradation model.....	90
5.6 Summary	94
 Chapter 6. Particle Removal Mechanisms in Synergistic Aging of Polymers and GRP Composites under Combined UV and Water Movement	 95
6.1 Introduction.....	96
6.2 Interaction of particles with substrates	98
6.3 Particle removal by hydrodynamics.....	101
6.4 Simulation of hydrodynamic effects on flat and wavy surfaces	103
6.5 Particle removal simulations and preliminary verifications	108
6.5.1 Adhesive forces for small epoxy particles on wet epoxy surfaces	108
6.5.2 Explanation of particle removal in Fig. 3.13 from [14].....	110
6.5.3 Predictions of particle movements on smooth inclined surface caused by moving water	111
6.6 Experiment verification of particle removal by hydrodynamic effects	112
6.7 Summary	116
 Chapter 7. General Discussion; Effect of Surface Roughness of both Particles and Substrates on Particle Removal; Critical Evaluation of Proposed Particle Removal Mechanism and its Actual Effect on Synergistic Aging of Polymers	 117
7.1 Introduction.....	118
7.2 Adhesion and Van der Waals force	119
7.3.1 Application the Rumpf model.....	122
7.3.2 Application the Rabinovich model	124
7.4 Comparison of the Rumpf, Rabinovich, and Hamaker models	131
7.5 Limitations of the Rumpf, Rabinovich, and Hamaker models and their potential improvements.....	134
7.6 Adhesion forces between irregular particles and irregular surfaces	138
7.7 Predictions of irregular particle movements on uneven surface caused by moving water	145
7.7 Summary	147
 Chapter 8: Conclusions.....	 149
 References.....	 154
 Appendix: Acronyms and symbols.....	 167

List of Tables

Table 2. 1. Chemical compositions of E-glass and ECR-glass [29].	11
Table 2. 2. Advantages and disadvantages of using thermoset and thermoplastic matrices [22].	13
Table 2. 3. Photon energy distributions by various wavelengths.	16
Table 2. 4. Bond strength in polyatomic molecules [36][37].	17
Table 3.1. Tested GRPs	41
Table 4.1. The characteristic absorption bands of the VE in the spectra.	62
Table 5.1. Physical parameters required for the UV radiation simulations.	82
Table 5.2. Comparison of surface roughness of unexposed and exposed to UV epoxy surfaces after 1000h.	91
Table 6.1. Total weight changes with standard deviations for six different GRP composites (A-F) tested in [14] individually under UV for 1000h at 80 °C followed by water condensation at 60 °C also for 1000h (Individual Exposures) and under combined 16 hours of UV exposure at 80 °C followed by 8 hours of water condensation at 60 °C for 1000 hours (Cyclic Exposures).	96
Table 6.2. Adhesion and gravitational forces, and buoyancies for epoxy particles of different sizes determined from the DMT and JKR models.	109
Table 6.3. Particle size distribution analyses; maximum Ferret's diameters.	115
Table 7.1. Adhesion forces from the Rumpf model for different asperity sizes compared with the predictions using the JKR and Hamaker methods.	124
Table 7.2. Parameters used in the simulations using the Rabinovich model.	127
Table 7.3. Values used in calculations.	132
Table 7.4. Parameters used in simulations using the modified Rabinovich model.	137
Table 7.5. Parameters used in the comparative study.	142

List of Figures

Figure 1.1. Main stages of UV/water degradation process	2
Figure 2. 1. Classification of composites [26].	8
Figure 2. 2. Classification and physical properties of various glass fibers [22]	9
Figure 2. 3. Characteristic group for epoxies [1].	14
Figure 2. 4. The diglycidyl ether of bisphenol A (DGEBA) [32].	14
Figure 2. 5. A photon initiates the degradation of a segment of the coating, which is volatilized or washed away. The adjacent polymer coating can either be sensitized or hardened against further photon-initiated degradation.	26
Figure 2. 6. Schematic illustration (cross section view) of epoxy–amine coating during exposure to ultraviolet (UV) radiation and humidity. On the surface of the coating, a thin oxidation zone is formed, where the degradation takes place.	30
Figure 3.1. Inside of the Q-LABQUV/SPRAY/RP chamber equipped with fluorescent UV lamps.	39
Figure 3.2. Typical surface characteristics of A and D composites after 1000 hours of exposure to dry hot UV.	43
Figure 3.3. SEM images of exposed surfaces after 1000 hours of UV radiation for Vinyl ester Epoxy ECR-Glass 1 – Composite A; a) low magnification at $\times 300$ and b) high magnification at $\times 1500$	43
Figure 3.4. SEM images of exposed surfaces after 1000 hours of condensation for Vinyl ester Epoxy ECR-Glass 1 – Composite A. a) low magnification at $\times 300$ and b) high magnification at $\times 1500$	44
Figure 3.5. SEM images of exposed surfaces after 1000 hours of UV and condensation for Vinyl ester Epoxy ECR– Composite A.	45
Figure 3.6. Weight changes for six composites under UV radiation as a function of time.	46
Figure 3.7. Weight changes for six composites under water condensation as a function of time.	47
Figure 3.8. Weight changes for six composites under cyclic UV and water condensation as a function of time.	47
Figure 3.9. Weight changes for six composites tested under cyclic UV/condensation and the sums of weight changes under individual UV and condensation conditions with time.	50
Figure 3.10. Averaged weight changes with standard deviations for six composites tested under individual UV and water condensation, cyclic UV and condensation, and the averaged sums of weight changes from the individual exposures as a function of time. .	50
Figure 3.11. SEM images of unidirectional GPRs; before exposure (left), after UV radiation (middle) and after cyclic UV & moisture condensation (right); a) Vinyl ester	

Epoxy with ECR-Glass 2, b) Polyester ECR-Glass 2, c) Epoxy ECR-Glass 2 and d) PU ECR-Glass 2.....	52
Figure 3.12. Schematic illustration of polymer sample during exposure to UV radiation and humidity.	52
Figure 3.13. Material is exposed to the UV radiation (a), then small particles are formed on the surface, which are then washed away by water flow (b).	54
Figure 3. 14. Surface degradation of ECR glass vinyl ester epoxy composite after UVB and water condensation; a) unexposed, b) 500 hours, c) 1000 hours and d) 1500 hours. 56	
Figure 3.15. Weight changes for ECR-2 glass/vinyl ester epoxy composite under cyclic UVA & water condensation vs. under UVB & water condensation.....	56
Figure 3.16. Yellowing of specimens after 1000 hours UV radiation.	57
Figure 4.1. Structure of VE monomer.	60
Figure 4.2. Structure of VE resin.	60
Figure 4.3. FTIR spectra of as received, exposed two days and four days vinyl ester epoxy ECR-Glass 1 fiber composite.	62
Figure 4.4. Compounds with hydroxyl groups, hydroperoxides and peroxide structures resulted during irradiation of VE resin.	63
Figure 4.5. The photo-oxidative degradation mechanism of VE resin.	64
Figure 4.6. Weight changes for six polymers under UV radiation as a function of time. 65	
Figure 4.7. Weight changes for six polymers under cyclic UV and water condensation as a function of time.	66
Figure 4.8. SEM images of pure PVC polymer; a) before exposure, b) after UV radiation and c) after cyclic UV & moisture condensation.	67
Figure 5.1. SEM images of unidirectional ECR-glass/epoxy composite; a) after UV radiation and b) after cyclic UV & moisture condensation [14].....	71
Figure 5.2. Schematics of incident beam direction on a sinusoidal surface.	76
Figure 5.3. Average weight changes of epoxy polymer composite (a) and PVC (b) samples at 80 °C with and without UV.....	80
Figure 5.4. Estimated weight changes of epoxy composite and PVC polymer samples by UV radiation condition for 1000 hours after subtracting the 80 °C heat effect in Fig. 5.3.	81
Figure 5.5. Thickness reduction rates with respect to time under different radiation angles (in degree).	83
Figure 5.6. Initial stages of UV degradation of a sinusoidal polymeric surface subjected to UV at 90 °.....	84
Figure 5.7. Complete UV degradation of a sinusoidal polymeric surface subjected to UV at 90 °.....	84
Figure 5.8. Thickness degradation at three different locations of the sinusoidal surface. 85	
Figure 5.9. Examples of severe oscillations in the solution caused by the numerical instability.....	86

Figure 5.10. Schematics of six surfaces; a) three surfaces with the same frequency but different amplitudes and b) three surfaces with the same amplitude but different frequencies.	88
Figure 5.11. Simulated RMS roughness values of three surfaces with different amplitudes as a function of UV radiation time.....	89
Figure 5.12. Simulated RMS roughness values of three surfaces with different frequencies as a function of UV radiation time.	89
Figure 5.13. Surface topographies of unexposed (left) and UV exposed (right) for 1000h surfaces of the epoxy specimens. Inserts show magnified SEM images of their surface topographies.	93
Figure 5.14. Representation of planarization effect after UV exposure.	93
Figure 6.1. Particle removal mechanisms in laminar flow: (a) lifting; (b) sliding; and (c) rolling.....	101
Figure 6.2. The effect of surface morphology on water flow velocities for 0 mm, 0.02mm, and 0.2 mm surface amplitudes all with a frequency of 20 1/s.....	104
Figure 6.3. Viscous stresses along three surfaces with three different surface profiles: flat (a), sinusoid low amplitude (b) and sinusoidal large amplitude (c).....	104
Figure 6.4. Streamlines of water flow for 0.02 and 0.2 mm amplitudes.	106
Figure 6.5. Maximum and minimum viscous stress locations for 0.02 mm surface amplitudes.	107
Figure 6.6. The effect of volumetric forces on 45 ° and 90 ° inclined surfaces.	107
Figure 6.7. The effect of surface profile amplitude and surface inclination on the average viscous shear stresses.....	108
Figure 6.8. Critical size of particle which could be removed by different average shear stresses caused by volumetric forces.	112
Figure 6.9. Initial particle distribution before water cleaning test.....	113
Figure 6.10. Schematics of particle distributions (a) before and (b) after water cleaning experiments.	113
Figure 6.11. SEM images of remaining particles after water flow; (I) mostly small particles, (II) combination of small and large particles, and (III) agglomerates of mostly large particles.....	115
Figure 7.1. a) Schematic illustration of a water droplet on primary asperities and secondary asperities in a micro/nano structure surface and b) a SEM image of a micropapillae with nanobranches [138].....	119
Figure 7.2. Schematics of hemispheres and spherical caps.	120
Figure 7.3. Nano/micro roughness structure on the surface of a lotus leaf [139].	121
Figure 7.4. Schematics of particle-surface interfacial contacts illustrating the effect of surface roughness on the adhesion of particles to various surfaces, (a) particle size greater than distance between two peaks, (b) particle size smaller than distance between two	

peaks, (c) particle on flat surface, and (d) particle interlock with rough substrate surface.	122
Figure 7.5. Schematic illustration of the geometry proposed by Rumpf for the interaction of an adhering particle with a rough surface. Diagram depicts a hemispherical asperity of radius r and origin at the surface interacting along the y axis with a spherical adhering particle.....	123
Figure 7.6. Schematic illustration of the geometric model used to calculate adhesion forces using the Rabinovich model.....	125
Figure 7.7. Schematics of all interactions between a sphere and a hierarchical structured surface.....	126
Figure 7.8. Predictions of sphere/secondary asperity, sphere/primary, and sphere/substrate interactions.....	128
Figure 7.9. Adhesion forces for different particle sizes calculated using the Rabinovich model.....	129
Figure 7.10. Schematic diagram of particle-rough surface interaction with particle radii	129
Figure 7.11. Predictions of adhesion forces for an epoxy sphere with irregular surfaces as a function of $rms1$ and $rms2$. R is $10\ \mu m$	130
Figure 7.12. (a) Predictions of adhesion forces for an epoxy sphere with the irregular surfaces as a function of R and $rms2$ and (b) cross-section view of (a) at $rms2 = 1nm$.	131
Figure 7.13. Comparison between the Rumpf, Rabinovich and Hamaker models for adhesion forces between an epoxy substrate and a $10\ \mu m$ epoxy sphere separated by $H_0 = 0.4\ nm$	133
Figure 7.14. (a) Schematic diagram of particle-rough surface interaction ($rms1 > R$). Particle interaction between hilly portion; (b) Schematic diagram of particle-rough surface interaction ($rms1 > R$). Particle interaction between valley portion; (c) Schematic diagram of particle and valley portion of primary asperity showing multiple interactions of adhering particle and secondary asperities. Here r is comparable to R ; (d) Schematic diagram of particle-rough surface interaction ($rms1 < R$). [144].....	136
Figure 7.15. Adhesion forces for different particles sizes calculated with the modified Rabinovich model with different numbers of contacts.	137
Figure 7.16. Schematics of a particle-surface interfacial contact, (a) particle size greater than the distance between two peaks, (b) particle size smaller than the distance between two peaks, (c) particle size similar to the distance between two peaks.	139
Figure 7.17. Schematics of a rough particle (submerged-sphere roughness) and a rough substrate (submerged-sphere roughness) [145].	140
Figure 7.18. Comparison between adhesion forces obtained from the Rumpf, Rabinovich, Hamaker, and modified Rabinovich models for an epoxy substrate and a $10\ \mu m$ epoxy particle separated by H_0 equals to $0.4\ nm$. $Rms4$ is $60\ nm$	143
Figure 7.19. Comparison between adhesion forces obtained from the Rumpf, Rabinovich, Hamaker, and the modified Rabinovich models for an epoxy substrate and a $10\ \mu m$ epoxy particle separated by H_0 equals to $0.4\ nm$. $Rms2$ is $60\ nm$	144

Figure 7.20. Predictions of adhesive forces using the modified Rabinovich model between irregular particles and irregular surfaces as a function of nanoscale rms particle and rms surface.	145
Figure 7.21. Critical sizes of particles which could be removed from different rough surfaces by shear stresses from slowly moving water. Modified Rabinovich model.	146
Figure 7.22. Critical sizes of particles which could be removed by lifting from different rough surfaces subjected to gravitational water flow. Various models.	147

Chapter 1: General Introduction

Glass Reinforced Polymer (GRP) Composites, as a subclass of a much larger group of Polymer Matrix Composites (PMCs), have received increasing attention due to their advantages such as superior mechanical performances, which allows them to be excellent substitutes for metallic and other materials. Another significant benefit is the controllable tailoring of GRPs, which makes it possible for them to meet specific requirements for various applications [1]. Glass fibers usually have excellent properties like high strength, flexibility, stiffness and resistance to chemical corrosion [2]. The polymer matrix, either thermoset or thermoplastic, binds the fibers together and helps create the material's strength and stiffness characteristics [3]. This thesis concentrates on the long-term performance of GRPs subjected to extreme environmental aging conditions.

In general, GRPs have been widely used in the electronics, aerospace, automotive, marine, and construction industries. They have been replacing various traditional materials such as woods, metals, ceramics, and plastics because of their lightweight, high strength and lower cost. However, PMCs and their subclass GRPs also have limitations, for example, the long-term structural stability and durability. Some outdoor applications of GRPs have been restricted due to complex degradation mechanisms developed under extreme environmental conditions, such as high temperature, ultraviolet (UV) radiation,

moisture, ozone and chemically corrosive environments [3]. As GRPs can be damaged by aggressive in-service conditions, the expected lifetime and their long-term reliability are not always certain. Therefore, the lifetime or residual time prediction of GRPs in service becomes a critical issue for their successful applications. Most current environmental aging models are limited to do simulations with only one individual degradation factor, such as individual UV light, elevated temperature, water diffusion and others [5][6][8][9]. For UV radiation models, most current investigations focus on the degradation of polymer coatings and use statistical approaches (reliability theory) to develop cumulative damage models [10][11][12]. There are few studies concentrated on environmental aging models which consider synergistic degradation mechanisms and combined influences of damaging conditions [13][14][15][16][17][18][19]. In this work, based on the synergistic aging mechanisms observed in artificially environmental degradation experiments, a new model of polymers degradation under UV and water condensation was proposed. According to the damage hypothesis, the synergistic environmental aging model consists of two consecutive processes including Part (A) UV radiation damage formation on polymer surfaces and Part (B) cleaning UV damage on polymer surface by water, as presented in Fig. 1.1.

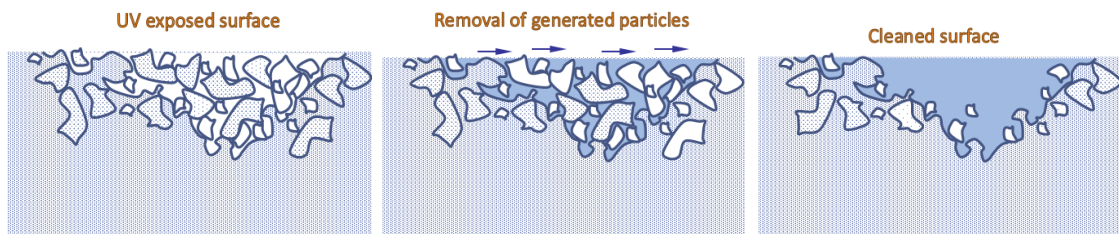


Figure 1.1. Main stages of UV/water degradation process

When commercially available polymers and polymer composites are subjected to UV radiation, photooxidation is one of the main degradation mechanism that can occur on the material surface. Photooxidation that initiates with the absorption of UV photons by chromophores i.e. hydroperoxides, catalyst residues, carbonyls, and unsaturated molecules containing double and triple bonds, and/or rings [21] is very complex. In this research, the UV dosage accumulative method was adopted to build a UV radiation model. This UV radiation model combines the energies of UV photons absorbed by an exposed polymer surface with the possibility of damage formation on material surface to produce a quantitative degradation process. This physical approach is more applicable to the simulation of the aging process of polymer materials in general compared to chemical methods because there is no need of step-by-step photodegradation reactions to be considered. In this research, flat and sinusoidal epoxy polymer surfaces were numerically simulated for their UV damage as a function of UV intensity, surface topography, and exposure time. This was subsequently verified experimentally by exposing neat epoxy specimens to UV in the air at 80 °C for 1000 hours and by precisely monitoring their surface topography as a function of time.

The damaging effect of water on polymer composites, on the other hand, is not as harsh as degradation just by UV radiation even at elevated temperatures. It has been observed that under the combined UV/ water condensation conditions, the main role of water is to remove the particles generated by UV (Fig.1.1) from the GRP surfaces and to expose the underlying virgin polymer to the next UV cycle. Therefore, hydrodynamic effects simulated by finite element methods and a particle removal model calculated by

the Johnson-Kendall-Roberts (JKR) method are added to the synergistic degradation study to explain the accelerated aging under the cyclic UV/water condensation condition. This simulation was also experimentally verified and then used to determine the manner in which micro-polymer particles are moved by slowly moving water on UV damaged polymer and GRP composite surfaces.

A comprehensive discussion including a general comparison of adhesion forces between spherical particles and irregular particles on nano/micro rough surfaces simulated using the Rumpf, Rabinovich, Hamaker, and the modified Rabinovich models is presented in Chapter 7. According to the simulation results based on the four models, nanoscale asperities distributed on the polymer surfaces will significantly reduce the interactions between particles and rough surfaces by diminishing the contact area. When particles also become rough, nanoscale asperities of particles are much more influential on adhesion forces than nanoscale asperities of substrates. In addition, the critical size of particles which could be removed by water flows from rough surfaces was found to be significantly smaller compared to flat surfaces.

This study is one of the main research projects of the National Science Foundation Center for High Voltage/Temperature Materials and Structures at University of Denver and was requested by several industrial sponsors interested in the synergistic environmental aging of GRPs and its computational simulations under extreme aging conditions. The main goal of the study was to simulate the synergistic aging processes in polymers and GRPs under aggressive environmental conditions, especially under UV &

water condensation as a function of time and temperature. The study was performed at the University of Denver between 2014 and 2018.

Chapter 2: Literature Review

This literature review is divided into two parts. Firstly, the fundamental concepts of GRPs, classification, and the main applications of GRPs are introduced. A general overview of the degradation of GRPs caused by aggressive environments is presented. Although GRPs exhibit various intrinsic advantages over more traditional materials, long-term structural stability and durability of these materials are still causing concerns. Secondly, environmental degradation of polymer composites used outdoor has become a complicated issue related to UV radiation, moisture, ambient temperature, service time, interfaces between fiber and matrix, additives, chemical composition and even crosslinking density of the matrix. The simulations of synergistic aging caused by those factors are very complex and difficult. Therefore, a comprehensive literature review of developed environmental aging models of polymers is critical for the proper understanding of complex degradation process in polymers. This is presented in chapter 2.2.

Photodegradation and oxidative degradation will occur on polymers or polymer composites surface when they are subjected to strong UV radiation in air. Thermal degradation and moisture degradation of polymer materials will occur when they are subjected to elevated temperature, rain or mist. All these environmental factors will work individually or in combination to cause the loss of sustained performance of polymeric

products. Furthermore, these environmental degradations will result in complicated physical and chemical reactions and unpredictable variables related to those reactions, which eventually make synergistic aging simulation very difficult.

2.1 Introduction to composites and their aging issues

Composite generally can be defined as a combination of two or more chemically and physically different phases separated by a distinct interface [21]. The different materials work together to provide more unique properties or useful structures, which are not attainable by any of the components alone [23]. Usually, we can identify different constituents within one composite as they do not dissolve or blend into each other [24].

Specific composites can be designed to satisfy general or extreme service conditions by properly selecting their constituent phases, their distributions, their proportions, their morphologies, as well as the structure and composition of the interface between constituents [23]. Due to this wonderful ability, composites are manufactured to optimize chemical, physical and mechanical properties. For instance, optimization of thermal (softening and melting points, thermal expansion /thermal conduction, specific heat), electrical (electrical conductivity/electrical permittivity, dielectric loss), and acoustical properties [1].

Composites can be classified on the basis of their matrix material. Hence, the main classes are metal matrix composites (MMCs), ceramic matrix composites (CMCs),

and polymer matrix composites (PMCs) (Fig. 2.1) [25]. The classifications according to types of reinforcement are particulate composites, fibrous composites, and laminate composites [26][27].

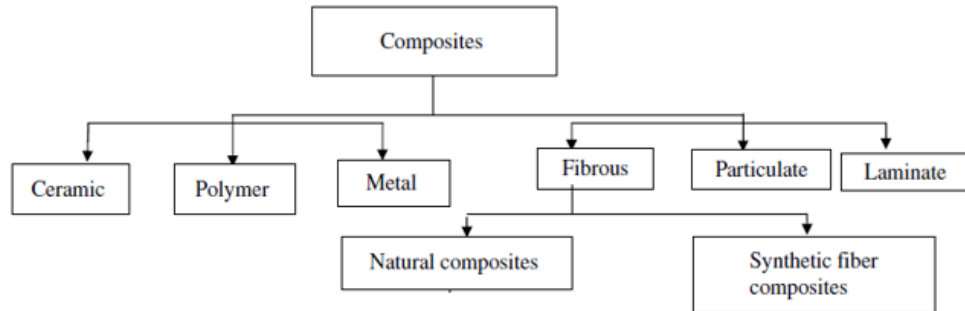


Figure 2. 1. Classification of composites [26].

2.1.1 Glass fiber-reinforced polymer matrix composites

GRP composites are constitutive of a reinforcing material, here, glass fiber embedded in a polymer matrix. Usually, GRPs can be classified according to the type of glass fibers as well as type of polymer matrices. Glass fibers have a high strength-to-weight ratio and pound-for-pound are stronger than steel in the lengthwise direction [1]. The polymers can be divided into two main classifications: thermoplastic and thermoset polymers, and both of them have been widely used.

Glass fibers: Most glass fibers are amorphous mixtures which comprise a silica (SiO_2) network, with additions of oxides of calcium, boron, sodium, iron, and aluminum [28]. These filaments of glass fiber are extruded from dies in diameters ranging from 5-20 μm after heating the mixtures to a melting state [21]. By far, glass fiber is the most

popular means of reinforcing plastic. Compared to other reinforcing fibers such as carbon fibers, glass fibers are not as strong or as rigid as carbon fiber, but they are much cheaper and significantly less brittle when used in composites. Various types of glass fibers have been developed during the last decades, such as A-glass, E-glass, S-glass and R-glass [21]. The major classification of various glass fibers and physical properties are shown in Fig. 2.2.

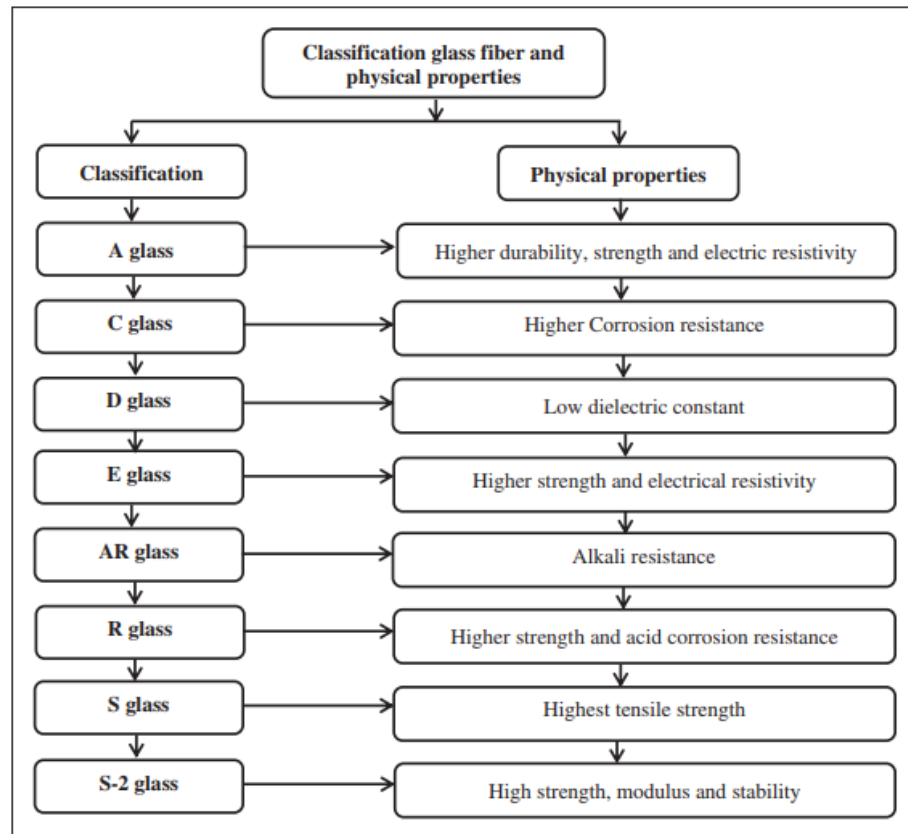


Figure 2. 2. Classification and physical properties of various glass fibers [21]

In this study, all tested GRPs and pure polymers were directly subjected to several aggressive conditions, including high humidity (97%) and elevated temperature (80 °C)

conditions. Hence, water erosion and thermal degradation of fibers become an important issue. Generally, glass fibers perform very well in thermal resistance but not very well in water resistance [22]. In experimental tests, two types of glass fibers, E-glass and ECR-glass fibers were embedded in thermosetting resins to prepare different reinforcement GRPs. The environmental aging results may be varied because of different glass fibers were used, which we should consider carefully.

E-glass (Electrical) and ECR-glass (Electrical Corrosion Resistance) are two main fibers broadly used in composite dielectrics. They help increase mechanical strength and provide high electrical insulating properties at the same time. E-glass was developed as a second form of glass fibers, named after its electrical insulation properties. This type was the first to be produced in filaments and today still forms more than 90% of all glass fibers produced worldwide for glass fiber-reinforced composites. ECR-glass is a modified E glass with improved corrosion resistance. It is boron-free and contains 2.9% ZnO. ZnO increases acid resistance [29]. Table 2.1 shows the chemical compositions of E-glass and ECR-glass.

Table 2. 1. Chemical compositions of E-glass and ECR-glass [29].

	E-glass	ECR-glass
Examples	Control	Control
SiO ₂ , wt%	59.45	58.1
Al ₂ O ₃ , wt%	12.29	11.5
CaO, wt%	23.55	21.7
MgO, wt%	2.55	2.0
TiO ₂ , wt%	1.10	2.8
Na ₂ O, wt%	0.90	1.0
ZnO, wt%	–	2.9
Li ₂ O, wt%	–	–
Fe ₂ O ₃ , wt%	0.25	0.1
RO (CaO + MgO)	26.10	23.7
SiO ₂ /RO	2.28	2.45
Log₃ FT, °C	1258	1235
Liquidus, °C	1173	1166
Delta T, °C	85	69
Reference/Ex.	[13, 14]	[32, 33]

Note: B₂O₃ is 0-10 % in E-glass according to ASTM D578-05 [147].

At the same time, the matrix material can serve to uniformly distribute the applied load, and transfer the loads to the fibers. In addition, some properties of composite materials mainly depend on the characteristics of the matrix material.

Polymer matrices: The matrix usually comprises 30%–40% by volume of a composite structure, which normally determines the resistance of the PMC to most of the aging processes that eventually cause the failure of the structure. These processes include impact damage, delamination, water absorption, chemical attack, and high-temperature creep. Thus, the matrix is typically the weak link in the PMC structure.

According to classification, the polymers are mainly divided into thermosets and thermoplastics.

At present, the plastic consumption for matrices is roughly estimated at:

- 60–65% of thermosets. The unsaturated polyester share is estimated at 85%, that of epoxies 10% and the remaining 5% for all the other thermosets.

- 35–40% of thermoplastics, particularly polypropylene but also polyester and advanced thermoplastics such as polyetherimide, PEEK, etc. [30]

Thermosetting resins have chemically cross-linked or three-dimensional network structures with covalent bonds with all molecules. They cannot be reshaped once solidified by cross-linking [21]. The most commonly used examples are epoxy, polyesters, and vinyl ester resins [28]. Different from thermosets, thermoplastic resins are not cross-linked, and they can be reshaped and softened by heat. Examples include polyethylene (PE), polypropylene (PP), nylons, polycarbonate (PC), polyamide-imides, polyether ether ketone (PEEK), etc. [21]. Advantages and drawbacks of using thermoset and thermoplastic resins are shown in Table 2.2.

Table 2. 2. Advantages and disadvantages of using thermoset and thermoplastic matrices [21].

Application	Property	Thermoset Matrix	Thermoplastic Matrix
Matrix	Formulation	Complex	More Simple
	Melt Viscosity	Low (at the Beginning)	Rather High
	Fibre Impregnation	Comparably Easy	Very Difficult
	Cost	Low to Medium	Low to High
Prepreg	Tack/Drape	Good	Comparably Low
	Shelf Life	Very Poor	Good
Composite	Processing Cycle	Very Long	Short to Long
	Processing Temperature and Pressure	Moderate	High
	Size of Products	Can be Very Large	Small to Medium
	Resistance to Solvents	Good	Poor to Good
	Damage Tolerance	Poor to Excellent	Fair to Good
	Resistance to Creep	Good	Not Known
	Interlaminar Fracture		
	Toughness	Low	High
	Ease of Fabrication	Labour Intensive	Less Labour Intensive

The studied materials including six types of thermoplastics (high-density PE, Ultra-high-molecular-weight PE, PC, PEEK, PVC, Nylon) and four types of thermoset resins (vinyl ester epoxy, polyester, epoxy, polyurethane). Here, epoxy resin was selected as an example to be introduced in detail.

Epoxy resins, also known as polyepoxides are a class of reactive pre-polymers and polymers which contain epoxide groups (an oxygen atom bonded with two carbon atoms) (Figure 2.3). The epoxy in the tested GRP epoxy composite investigated in this study is one of the most common epoxy resins called Bisphenol-A Epoxy resin (Figure 2.4). In Fourier Transform Infrared (FTIR) spectra, epoxy resin can be characterized with

its peaks at 890 cm^{-1} to 910 cm^{-1} attributed to an epoxy group. A hydroxyl group is indicated by a broad band at 4000 cm^{-1} [31].

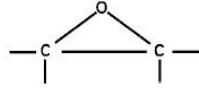


Figure 2. 3. Characteristic group for epoxies [1].

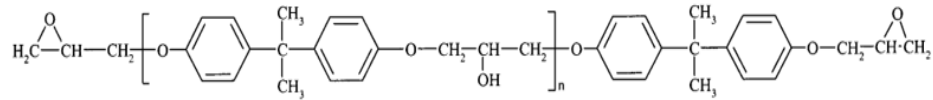


Figure 2. 4. The diglycidyl ether of bisphenol A (DGEBA) [32].

As matrices used in GRP composites, epoxy resins have many advantages. Usually, they have excellent mechanical properties, lower shrinkage during cure, resistance to numerous organic solvents, good adhesion to most fiber, etc. They have also drawbacks, including sensitivity to moisture and susceptibility to UV degradation (chalking) [33].

2.1.2 Polymer composite degradation

The maximum service time of a commercial composite product is always hard to determine, therefore the ability to predict its failure rate would be highly beneficial and significant. However, computational simulations can be quite difficult due to the extremely complicated degradation mechanisms that may occur in GRPs when subjected to aggressive environments. In this study, UV radiation, moisture, and thermal stability are selected to be the environmental factors used in the experimental tests.

UV radiation: UV radiation has a wavelength between 280 and 400 nm (UVA: 400-315 nm and UVB: 315-280 nm), and the energy associated with these wavelengths is comparable the bond dissociation energies of the polymeric materials. Hence, these wavelengths can dissociate the molecular bonds in polymers and may lead to the degradation of the materials [34]. UV-induced degradation usually includes a loss of surface gloss, surface discoloration, chalking, flaking of surface resin, pitting, microcracking, and a severe loss of resin in GRP composites [35]

To fundamentally understand the probability of these degradation mechanisms, whether they will occur or not, we need to compare the energies of incident UV photons and bond strength in the polymer. By applying the photon energy formula through Eq. 2.1, we can calculate the energy of UV photons at different wavelengths, as shown in Table. 2.3.

$$E = Nhf = \frac{Nhc}{\lambda} = \frac{119586}{\lambda} \left[\frac{kJ}{mol} \right] \quad \text{Eq. 2.1}$$

where:

- E energy of radiation of a given wavelength
- N Avogadro's number = 6.022×10^{23} in mol⁻¹
- h Plank's constant = 6.626×10^{-34} J s
- f frequency of radiation
- c velocity of light = 2.998×10^8 m/s
- λ wavelength of radiation in nm

Table 2. 3. Photon energy distributions by various wavelengths.

Wavelength(nm)	280	290	320	350	380	400
each photon (eV)	4.43	4.27	3.88	3.54	3.32	3.10
energy (KJ/mole)	427	412	374	342	320	299

The conversion factors are: 1kJ/mole = 0.010365eV/bond

If the photon energy is equal to or greater than the bond strength (i.e. bond dissociation energy) then bond breakage can take place. By comparing the data in Table 2.3 with that in Table 2.4, it can be seen that the energy of some UV photons is comparable to the dissociation energies of some specific polymer covalent bonds. For example, the energy of UV photons at 320 nm wavelength is 374 KJ/mole almost equal to the dissociation energy of C-C bond (376 KJ/mole). Generally, all chain scission caused by UV exposure is a result of oxidation initiated by high energy photon radiation. Hydroperoxides are one significant intermediate which may result in chain scission and crosslinking.

Table 2. 4. Bond strength in polyatomic molecules [36][37].

Bond	Bond Strength* (dissociation energy) (kJ/mole)	Bond strength (eV/bond)	Bond Energy** (kJ/mole)	Molecule	Bond Length* (nm)
C-C	376	3.9	348	CH ₃ -CH ₃	0.154
C=C	733	7.6	615	H ₂ C=CH ₂	0.13
C≡C	965	10	812	HC≡CH	0.12
C-H	439	4.55	415	H-CH ₃	0.11
C-N	298	3.09	292	C ₆ H ₅ CH ₂ -NH ₂	0.15
C-O	277	2.87	350	CH ₃ - OC(CH ₃)CH ₂	0.14
C=O	532	5.51	725	O=CO	0.12
C-F	472	4.89	441	F-CH ₃	0.14
C-Cl	350	3.63	328	Cl-CH ₂ Cl	0.18
O-H	437	4.53	463	H-OCH ₃	0.1
O-O	157	1.63	143	CH ₃ O-OCH ₃	0.15
O-Si	536	5.56	432	HO-Si(CH ₃) ₃	0.16
N-H	383	3.97	391	H-N(CH ₃) ₂	0.1
N-O	175	1.81	175	CH ₃ O-NO	0.12
F-F	158	1.64	158	F-F	0.14
H-H	436	4.52	436	H-H	0.074

Diffusivity and moisture: pure polymers and GRPs have quite different diffusivity and moisture properties due to the participation of glass fibers. The fiber/matrix interfaces are believed to be a pathway for the rapid diffusion of water into the GRPs. Moisture inside a polymer composite leads to chemical and mechanical degradation [58]. Elevated temperature and high humidity environment may even accelerate the hydrolysis and dissolution of interphase substances, and further increase the degradation process. Long-term moisture absorption leads to the degradation of mechanical properties [39][39][41][41][148-152] of GRPs which significantly reduce the service life of GRP structures and components. A study indicates that E-glass/vinyl ester

composites showed 60% and 10% reductions in tensile strength and stiffness, respectively, after submersion in fresh water for about 2 years [41]. In contrast to GRP composites, pure polymers without fibers exhibit better resistance to hygrothermal aging because of low diffusive rates.

Thermal stability: GRPs are sensitive to temperature variations as a result of induced thermal stresses between the fibers and polymer matrix due to their distinct thermal expansion coefficients [42]. At elevated temperature differential thermal expansion of the fiber and matrix may lead to the formation of microcracks at the fiber/polymer interface [44]. In this study, the maximum temperature used in tests is 80 °C, and all of GRPs have high glass transition temperatures (> 120 °C). Therefore, regardless of their effects on mechanical strength, it is not necessary to consider the decomposition process of GRPs during UV radiation and thermal tests, at least, under 80 °C.

2.2 Environmental aging of polymers and PMCs

In this research, environmental aging of polymer materials is a combination issue which is related to UV radiation, water condensation and elevated temperature. Among all those environmental conditions, it was observed that the combination of UV and water condensation resulted in the most severe degradation of composites than under individual hot dry UV or individual hot water condensation [13]. Hygrothermal conditions (hot water condensation) or hot dry UV may also speed up aging rates but were not as serious

as the combination of UV and water condensation. Therefore, it was concluded that UV radiation and water condensation performed in a synergistic manner which accelerated the degradation of polymer composites. Moreover, as the main goal of this research is to set up novel models to simulate the synergistic environmental aging process of polymer materials, experimental and modeling studies of UV radiation and water condensation have been widely searched in this literature review.

2.2.1 Experimental aging of polymer materials

For UV radiation, the degradation starts at the outer surface of the polymeric materials which is exposed to the UV light. If the light penetration is limited to the surface only then it may result in surface discoloration only, and if the degradation penetrates through the bulk of the material then it can result in degradation in mechanical properties of the polymer materials [45]. The extent of degradation of the material under the exposure of UV radiation depends on the type of polymer and the duration of exposure [46][47]. UV radiation can cause either random chain scission or an increase in cross-linking density in the polymers and consequently leads to variations in brittleness and reduction in material strength [48].

For moisture degradation in GRPs, water molecules diffuse through the material which promotes matrix plasticization, degradation of interfacial strength and differential swelling. The combination of the time-dependent weakening of the interfaces with the high differential swelling stresses promotes crack formation along the interfaces and

cause additional water uptake in the newly created empty volumes. Hygrothermal aging, refers to the synergistic aging under moisture and elevated temperature environment, and can further accelerate moisture diffusion [49].

Fritz Larsson [50] studied the effect of UV light on the mechanical properties of Kevlar 49 composites. Their results elucidated that the degradation depends on the thickness of the composite. They postulated that only 0.13 mm thick specimens were found to be affected by UV exposure and their strength retained 60% after 1000 h exposure. No degradation effect on 0.25 mm and 0.50 mm thick laminates was observed.

W. B. Liao et al. [51] observed that the damage due to UV radiation is higher when the composites are exposed to air than in a near-vacuum system. Their results showed that the weight loss of the glass/epoxy system was larger than that of the graphite/epoxy system. They also observed that surface erosion occurred on all specimens irradiated by UV radiation in SEM images.

B. Mailhot et al. [52] studied the degradation of an epoxy (DGEBA)/amine (diamine) resin under photolytic conditions in the absence and presence of oxygen. Their FTIR and UV-Vis analysis revealed that the photoproducts detected during the degradation result from the oxidation of the DGEBA part, of the crosslinks. During irradiation, the yellowing phenomenon was mainly due to the formation of a quinone methide structure.

R. Scaffaro et al. [53] measured the combined effects of humidity, temperature, mechanical stress, and UV exposure on the creep behavior of polyamide. Their results indicated that all the conditions which affect the possibility of the sample to crystallize, such as the presence of water, a temperature above the glass transition or a moderate decrease of the molecular weight, can cause an increase of the creep rates. The UV exposure accelerated both degradation processes and resulted in a final higher creep value of the deformation.

D. E. Mouzakis et al. [16] investigated the combined action of temperature, humidity and UV radiation on polyesters and polyester composites in an environmental chamber. Their experimental data revealed that the polymer matrix became stiffer in an irreversible way after exposure. Scanning electron microscopy (SEM) studies revealed that some microcracks had occurred on the surface of the specimens

E. C. Botelho et al. [54] investigated the effects of hygrothermal exposure, UV radiation, salt spray and thermal shock aging on the thermomechanical behavior of GF-reinforced by poly ether-imide (PEI) composites. Slight changes were observed both in glass transition temperature and in thermal expansion coefficient as a result of the environmental conditioning used.

A. P. C. Barbosa et al. [55] investigated the effects of aging on carbon fiber-epoxy samples exposed to alternating cycles of water condensation at 50 °C and UVA radiation

at 80 °C for 3 months. Changes within the material are evidenced by mass loss, fiber exposure, chemical alterations, increased crack density and fiber buckling in fractured specimens after mechanical testing.

J. Nicholas et al. [56] investigated the accelerated aging effects on a thermoset polyurethane composite material. A combined hygrothermal and ultraviolet (UV) chamber was used in an accelerated aging procedure to simulate temperate climate conditions. They found that the rate of color change and the total change in color for the fiber reinforced composite was much less than that of pure polyurethane. And the average retraction of the surface polymer was 30 µm at 1000 h of exposure to the accelerated aging environment.

A. S. Rios et al. [57] evaluated the mechanical, thermal and morphological behavior during accelerated aging in three thicknesses of composite plates used in wind turbines. Their results showed that the degradation primarily reduced the mechanical properties of the thinner composites, exhibiting fiber-matrix debonding in some damaged specimens after 180 days of exposure.

I.B.C.M. Rocha et al. [58] investigated material degradation effects caused by hygrothermal aging in composite and neat epoxy specimens for a fiber and resin system representative of the material used in wind turbine blades. Static and fatigue properties were measured and comparisons made on samples before and after immersion in hot

water (50 °C) for 4800 hours. Material degradation in composite specimens as measured through mechanical tests was not only dependent on the water uptake but also on immersion time, with shear strength reductions of up to 36% and fatigue life up to three orders of magnitude shorter. For resin specimens, a degradation level of approximately 17% was observed, both in tension and in bending.

Marialaura Clausi et al. [59] investigated the effects generated by exposure to UV-C radiation on nanocomposite films made of graphene nanoplatelets dispersed in an epoxy matrix. Their results showed that UV-C irradiation selectively degrades the polymer matrix of the nanocomposite films, giving rise to more conductive and hydrophobic layers due to exposure of the graphene component of the composite material.

N. Guermazi et al. [60] studied the environmental durability of three bidirectional laminated composites (glass-epoxy, carbon-epoxy and hybrid laminated bidirectional composites) dedicated to hygrothermal conditions. It could be concluded from the data that it was possible to suggest that water temperature could be the major factor in material degradation in all GRPs. The reduction in mechanical properties was caused by matrix plasticization due to the moisture and essentially the temperature.

2.2.2 Environmental aging models of polymer materials

UV radiation with high energy photons induced the chain scissions and crosslinking of polymer chains in GRPs [48]. Water may be chemically or physically involved in the degradation reactions. Oxygen in air and elevated temperature will also accelerate the aging process. Therefore, mathematical simulations become very difficult. Complicated physical and chemical aging mechanisms and various environmental input variables should be considered. Most current environmental aging simulations for polymer materials are restricted to one individual degradation factor such as elevated temperature, moisture diffusion, UV radiation and others [5-10]. Few works have focused on synergistic degradation under multiple aging conditions involving UV. In the following section, the most important recent studies have been reviewed of environmental aging simulations for polymer materials, including degradation caused by individual or combinations of UV, high temperature, water and time.

J. W. Martin [11][12][19] presented a stochastic model and partially validated for predicting the service life of a nominal population of polymethyl methacrylate films subjected to photolytic degradation. His model had a firm basis in the principles of photochemistry and extensive application in the biological community. The primary inputs into the model were dosage and material damage. Eq. 2.2 was used to calculate the total effective dosage, the total number of absorbed photons that contribute to the photodegradation of a material during an exposure period.

$$D_{\text{total}}(t) = \int_0^t \int_{\lambda_{\text{min}}}^{\lambda_{\text{max}}} E_o(\lambda, t) (1 - 10^{-A(\lambda, t)}) \phi(\lambda) d\lambda dt \quad \text{Eq. 2.2}$$

where λ_{min} and λ_{max} are minimum and maximum photolytically effective wavelengths (units: nm); $A(\lambda, t)$ is absorbance of the sample at specified UV-visible wavelength and at time t (units: dimensionless); $E_o(\lambda, t)$ is incident spectral UV-visible radiation dose to which a polymeric material is exposed to at time t (units: J cm^{-2}); t is elapsed time (units: s). $D_{\text{total}}(t)$ is total effective dosage (units: J) and $\phi(\lambda)$ is spectral quantum yield (dimensionless) defined by (Eq. 2.3):

$$\phi(\lambda) = \frac{\text{No. of molecules undergoing degradation at wavelength } \lambda}{\text{No. of quanta of wavelength } \lambda \text{ absorbed by the polymer}} \quad \text{Eq. 2.3}$$

Usually $\phi(\lambda)$ values observed for solid polymers exposed to UV radiation are typically two to three orders of magnitude less than 1, indicating that most absorbed UV radiation is dissipated as heat.

B. Hinderliter et al. [10][61][62] created a Monte Carlo model to predict surface coating degradation and used the results to predict the change in the coating properties with lifetime. Their model predicted qualitative changes of system properties based on various theoretical and empirical models which took surface profile properties and related them to measurable system properties, such as gloss, relative fracture toughness, and wetting contact angle. Fig. 2.5 schematically explained the UV aging process using the Monte Carlo method. Their model consisted of a coating layer divided into small boxes, and within any grid was only one material constituent. A single material was assigned to

each grid location at the beginning of the computer simulation. Each material was assigned a probability, p , that all incident photon would remove that small grid of material (Figure 2.5). The unsupported polymer fragments would be expected to be removed by processes such as rain or wind.

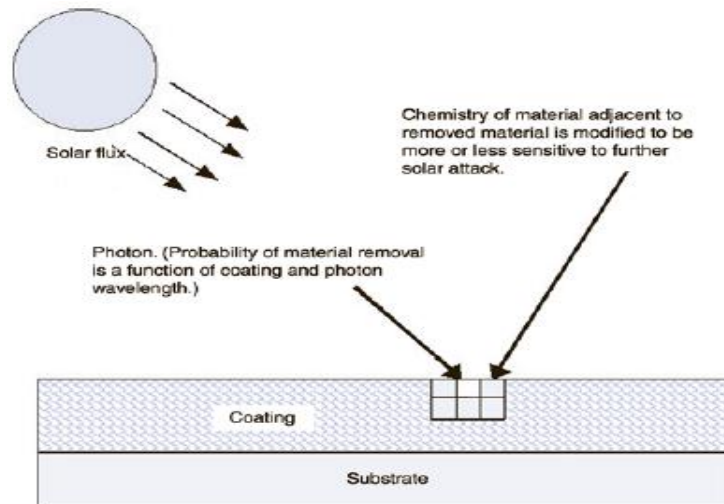


Figure 2. 5. A photon initiates the degradation of a segment of the coating, which is volatilized or washed away. The adjacent polymer coating can either be sensitized or hardened against further photon-initiated degradation.

The number, N , of polymer fragments removed from a particular location in the area of a coating may be calculated as follows (Eq. 2.4). In a consistent environment where the degradation process does not change, all the factors may be considered as part of a rate parameter, K/time . Thus the number of fragments removed proceeds linearly with exposure time, t .

$$\begin{aligned}
N = & \text{Average number of pieces removed at a point on the coating} = \text{Flux of photons at that position} \left[\frac{\text{photons}}{\text{time}} \right] \\
& \times \text{Absorption} \left[\frac{\text{photons absorbed per polymer segment volume}}{\text{photons incident on the segment area}} \right] \times \text{quantum efficiency of creating a polymer fragment} \\
& \left[\frac{\text{probability}}{\text{photon absorbed}} \right] \times \text{probability that the polymer segment is removed prior to recombination into the existing polymer} \\
& \times \text{exposure time, } t[\text{e.g. years}] = Kt
\end{aligned}
\tag{Eq. 2.4}$$

M. Evans [8] modified the statistical degradation model used by Guseva et al. for estimating the service life of polyurethane coatings under the combination of UV and water condition. His model was able to predict naturally weathered degradation curves by extrapolation from short term accelerated test results. It was found that when this model was applied to the naturally weathered data, gloss loss followed a generalized gamma distribution, rather than the Weibull distribution identified by Guseva et al. Equation 2.5, a log-linear relationship, is one of the main equations used in these studies.

$$\alpha = \exp \left[\lambda_0 + \lambda_1 \frac{1}{RV_1} + \lambda_2 \ln(V_2) + \lambda_3 V_3 \right]
\tag{Eq. 2.5}$$

where α is the characteristic life (the time by which there is approximately a 63% chance of failure), R is the universal gas constant ($8.314 \text{ J mol}^{-1} \text{ K}^{-1}$), V_1 the temperature (K), V_2 the UV irradiance at 340 nm [$\text{W}/(\text{m}^2 \text{ nm})$] and V_3 the aerosol stress which was treated as an indicator variable taking the discrete value of zero when no aerosol was applied and unity otherwise.

E. Guzmán et al. [63] established a macroscopic model following the pattern of a Prony series to quantify the effects of different environmental factors on the aging of carbon fiber reinforced plastics (CFRP) aging. Their model showed that the evolution of

mass and elastic properties over the time exhibited an asymptotic exponential increasing (or decreasing) pattern over the time. Again, one of the main equations used in these studies is shown in Eq. 2.6. This expression is a model expressing an exponential decay (or rise) of the constitutive properties of the samples subjected to accelerated aging.

$$y = \frac{Y}{Y_0} = 1 + \sum_i a_i \phi_i(x_1, x_2, x_3) (1 - e^{-n/10^{b_i}})$$

$$\phi_0 = (1 - x_1)(1 - x_2)(1 - x_3)$$

$$\phi_1 = x_1(1 - x_2)(1 - x_3)$$

$$\phi_2 = (1 - x_1)x_2(1 - x_3)$$

$$\phi_3 = (1 - x_1)(1 - x_2)x_3$$

$$\phi_{12} = x_1x_2(1 - x_3)$$

$$\phi_{13} = x_1(1 - x_2)x_3$$

$$\phi_{23} = (1 - x_1)x_2x_3$$

$$\phi_{123} = x_1x_2x_3$$

Eq. 2.4

where each function $\Phi(x_1, x_2, x_3)$ represents a series of samples under a given set of environmental conditions: temperature (x_1), relative humidity (x_2) and UV radiation (x_3). Physically, the identified constant coefficients α_i are the final asymptotic values of the loss/gain, and 10^{b_i} are the corresponding time constants (in number of cycles).

T. Fang et al. [64] established a nonlinear constitutive model for the whole hygrothermal aging process of natural fiber reinforced composites. Their model accounted for elastic and inelastic deformation, diffusion of water and hydrolysis, and considered the effects of matrix cracking, fiber-matrix interfacial debonding and changes in the microstructure of natural fibers. Equation 2.7 was the main equation they used to predict weight change of PMCs under hygrothermal conditions.

$$\frac{W_t}{W_{\max}} = (1 - e^{-k_c t}) - [\xi]_{t \rightarrow \infty} t + k_{\xi}^{-1} (\xi|_{t=0} - \xi|_{t \rightarrow \infty}) (1 - e^{-k_{\xi} t})$$

Eq. 2.5

where W_{\max} is the maximum weight gain for water absorption of composite samples. The first term on the right side represents the weight gain due to water absorption, while the second term represents the weight loss caused by hydrolysis reaction.

K. A. Wood et al. [65] explored the mass loss behavior of acrylic latex paint, using the framework of a simple conceptual model distinguishing different environmental factors to the photochemical mass loss rate. Their model indicated that the constant mass loss rate predicted was 3 - 4 times higher than the measured value. The main equation they used in the simulation is given in Eq. 2.8.

$$M' = \Sigma \int_0^Z dz \int d\lambda \phi(\lambda) I(\lambda, z) \quad \text{Eq. 2.6}$$

where M' is mass loss rate, Σ means total exposed surface area of the coating; λ is wavelength of light; $\phi(\lambda)$ is the quantum efficiency, i.e., mass loss rate/unit volume/unit light intensity at λ . $z = 0$ is the top (exposed) surface, and $z = Z$ is the bottom surface of the film. I is intensity of UV radiation.

Søren Kiil [9][66] developed a mathematical model to describe environmental aging mechanisms of epoxy-amine coatings when they were exposed to ultraviolet radiation and humidity at a constant temperature. Their model included photoinitiated oxidation reactions, intra-film oxygen permeability, water absorption and diffusion, reduction of crosslink density, absorption of ultraviolet radiation, a radical scavenger reaction, and simulated the transient development of an oxidation zone. The results

showed that the degradation rate of the non-stabilized coating was influenced significantly by the diffusion rate of oxygen in the oxidation zone, whereas light absorption by the photoproducts formed was only a secondary effect. The degradation process is schematically shown in Fig. 2.6.

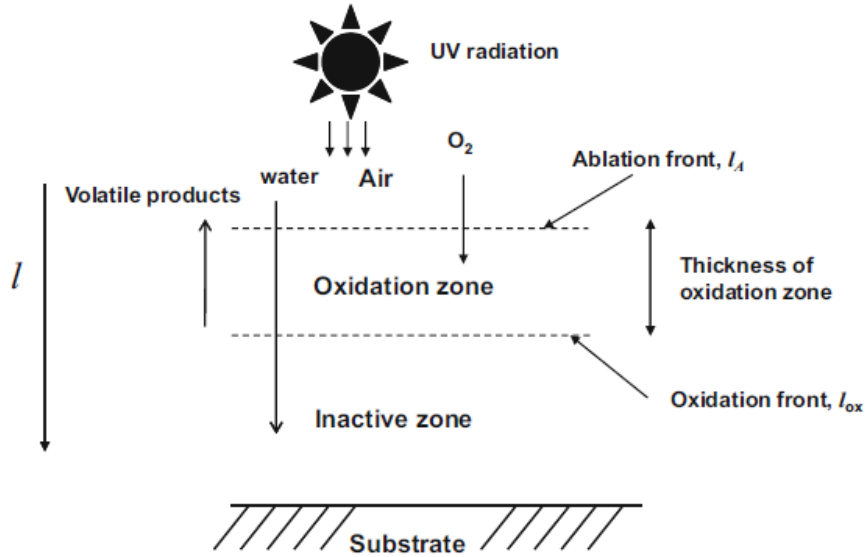


Figure 2. 6. Schematic illustration (cross section view) of epoxy-amine coating during exposure to ultraviolet (UV) radiation and humidity. On the surface of the coating, a thin oxidation zone is formed, where the degradation takes place.

Their model estimated the mass loss and matrix ablation of a coating, as well as oxygen and solid phase concentration profiles in the oxidation zone at all values of time.

The main equation they used is Eq. 2.9.

$$\frac{\Delta m}{m_o} = \frac{M_{W,water} A}{m_o} \int_{l_A}^{l_o} C_w dl - \frac{l_A A \rho_F}{m_o} - \frac{A \rho_F}{m_o} \int_{l_A}^{l_{ox}} \epsilon dl + \frac{A M_{w,O_2}}{m_o} \int_{l_A}^{l_{ox}} C_{carbonyl} dl$$

Eq. 2.7

where the first term on the right takes into account weight gain from water absorption, the second ablation, and the third term includes weight loss in the oxidation zone (formation of porosity due to coating degradation). Oxygen fixation to the resin is the fourth term. The simulation is one of very few mechanistic models based on mathematical descriptions of the physical and chemical phenomena taking place in coatings during exposure.

Based on all of the above environmental aging models, it is noted that the predictive simulations can be divided into two categories: (1) statistical (empirically based) approaches and (2) mechanistic models (chemical or physics based fundamental models).

The mechanistic models are based on mathematical descriptions of the physical and chemical degradation mechanisms taking place in polymers during exposure. Any level of complexity can, in principle, be obtained, but if the model contains too many unknown parameters it is not practical to use. Therefore, there are very few mechanistic models available. From the above literature searching, S. Kiil and K. A. Wood's fundamental models are two examples. On the other hand, mechanistic models can be used to suggest potential improvements in accelerated test procedures by identifying the key events in coating degradation and evaluating accelerated coating exposure conditions. This method is helpful to understand polymer aging but the time and effort involved in producing such a predictive model is a formidable challenge.

Empirically based approaches are also useful. These models are based on either a statistical approach leading to cumulative damage models, or quantitative mechanistic models, based on knowledge of the underlying degradation mechanisms. As mentioned above, Martin firstly started the statistically based approach with developing a stochastic model for the degradation of polymer films. Later Hinderliter and Croll used a statistical Monte Carlo approach to simulate coating degradation. These models are very useful to guide standards development and for building accelerated testing around a failure mode in each material. However, they also have drawbacks when they are applied to a synergistic aging condition rather than an individual condition; the synergistic prediction would have significant uncertainty associated with it [9].

2.4 Thesis statement

Based on the synergistic environmental aging of GRP composites observed in the experimental tests performed in this graduate research and Tianyi Lu's Master thesis completed in August 2014, a novel highly transformative model consisting of UV radiation and hydrodynamic effects was proposed to simulate the synergistic aging processes observed in the composites. Both the UV radiation damage model of polymers and the hydrodynamic model of polymer particle removal from UV damaged surfaces were experimentally verified. Importantly, a new particle removal model was suggested by considering adhesion forces between irregular particles and irregular surfaces by considering the modified Rabinovich model.

2.5 Publications

This dissertation is based on the following published documents:

A. MS Thesis

T. Lu, Degradation of high voltage glass fiber-reinforced polymer matrix composites by aggressive environmental conditions, University of Denver, Denver Colorado, August 2014.

B. Journal papers

1. T. Lu, E. Solis-Ramos, Yun-Bo Yi, M. Kumosa. Synergistic environmental degradation of glass reinforced polymer composites, *Polym. Degrad. Stab.* 131 (2016) 1-8.
2. T. Lu, E. Solis-Ramos, Y. Yi, M. Kumosa. Particle removal mechanisms in synergistic aging of polymers and glass reinforced polymer composites under combined UV and water, *Compos. Sci. Technol.* 153 (2017) 273-281.
3. T. Lu, E. Solis-Ramos, Y. Yi, M. Kumosa. UV degradation model for polymers and polymer matrix composites, *Polym. Degrad. Stab.* 154 (2018) 203-210.

C. Reports at HVT meetings; published in formal NSF approved HVT report

1. T. Lu, E. Solis-Ramos, Y. Yi, M. Kumosa. Synergistic aging of affordable polymer matrix composites, University of Denver, Denver Colorado, October 2015.
2. T. Lu, E. Solis-Ramos, Y. Yi, M. Kumosa. Synergistic aging of affordable polymer matrix composites, University of Illinois Urbana-Champaign, Champaign Illinois, May 2016.
3. T. Lu, E. Solis-Ramos, Y. Yi, M. Kumosa. Synergistic effects in environmental degradation of glass and basalt fiber composites, Michigan Technological University, Houghton Michigan, October 2016.
4. T. Lu, E. Solis-Ramos, Y. Yi, M. Kumosa. Synergistic effects in environmental degradation of glass and basalt composites, University of Denver, Denver Colorado, May 2017.
5. T. Lu, E. Solis-Ramos, Y. Yi, M. Kumosa, Synergistic effects in environmental degradation of glass and basalt composites, University of Connecticut, Storrs Connecticut, October 2017.

D. Posters at HVT meetings

1. T. Lu, E. Solis-Ramos, Y. Yi, M. Kumosa. Synergistic aging model of glass fiber reinforced polymer matrix composites by aggressive environmental conditions, University of Denver, Denver Colorado, October 2015.

2. T. Lu, E. Solis-Ramos, Y. Yi, M. Kumosa. Synergistic aging model of glass fiber reinforced polymer matrix composites, University of Illinois Urbana-Champaign, Urbana-Champaign Illinois, May 2016.
3. T. Lu, E. Solis-Ramos, Y. Yi, M. Kumosa. Synergistic effects in environmental degradation of glass and basalt fiber composites, Michigan Technological University, Houghton Michigan, October 2016.
4. T. Lu, E. Solis-Ramos, Y. Yi, M. Kumosa. Aging of polymers under combined UV and water condensation: particle removal mechanism, University of Denver, Denver Colorado, May 2017.
5. T. Lu, E. Solis-Ramos, Y. Yi, M. Kumosa. UV degradation model for polymers and polymer matrix composites, University of Connecticut, Storrs Connecticut, October 2017.
6. T. Lu, E. Solis-Ramos, Y. Yi, M. Kumosa. Synergistic aging model of glass fiber reinforced polymer matrix composites by aggressive environmental conditions, University of Illinois Urbana-Champaign, Urbana-Champaign Illinois, May 2018.

2.6 Disclaimer

During the course of his MS and PhD studies, Mr. T. Lu has closely collaborated with the following members of the HVT Center:

1. Dr. Euripides Solis-Ramos – coauthor of papers, reports and posters. In addition, Dr. Solis- Ramos helped Mr Lu with all of scanning electron microscope (SEM)

material characterization, surface topography analysis and experimental verifications of UV radiation model polymers.

2. Dr. Y. Yi – co-author of papers and reports, co-supervision/advising.
3. Dr. M. Kumosa – advisor, supervisor, coauthor of all papers, reports and posters.

Chapter 3. Synergistic Environmental Degradation of Glass Reinforced Polymer Composites

3.1 Previous work

In Tianyi Lu's Master's Dissertation entitled "Degradation of high voltage glass fiber-reinforced polymer matrix composites by aggressive environmental conditions" completed in August 2014, environmental degradation of various GRP composites with different polymer matrices and glass fibers was experimentally investigated. The composites were subjected to UV radiation, water condensation, and a nitric acid solution as a function of temperature. The composites were evaluated for their resistance to aging under UV, temperature, water and acids as a function of time, and the most important aging mechanisms in the composites were identified. Some of the composites had surface coatings applied. An interesting synergistic aging mechanism was also discovered. Then, in the subsequent two years after completing the MS thesis, the synergistic aging of the GRP composites was further investigated and supported by a new combined model of synergistic aging in the presence of UV, moisture condensation and elevated temperature. This chapter presents a summary of the previous aging work, a comprehensive examination of synergistic degradation of GRP composites, and the fundamentals of the synergistic aging model proposed in [13][67].

3.2 Introduction

Numerous studies have focused on the environmental degradations of PMCs in general, and more specifically, aging of GRP composites caused by a large variety of aggressive environments. Some of the most recent studies can be found in Refs. [5,6,7,68,69,70]. Very few of them, however, have dealt with the synergistic effects of aging of polymers and GRPs under combinations of several aging conditions [70][71][72]. Since this work is concerned with synergistic aging of a group of commercially available GRPs under combined UV radiation, moisture, temperature and time, an emphasis is made here to evaluate the research progress made so far in this very important area of polymer and polymer based composite science.

The UV components of sunlight which reach the ground are in the range of 280 - 400 nm [72]. The energy of ground reaching UV photons is comparable to the dissociation energies of polymer covalent bonds [20][74][75] resulting in a loss of surface gloss, surface discoloration, chalking, flaking of surface resin, pitting, microcracking, and a severe loss of resin [71][72][74-77] in GRPs. The damaging effect of water or moisture on polymer composites, on the other hand, is not as harsh as degradation just by UV radiation even at elevated temperatures [71]. However, moisture diffusion into polymer matrix/fiber interfaces can damage the interfaces by microcracking [78][79], especially at elevated temperatures. In addition, hydrolysis of chemical bonds may lead to permanent chemical degradation [5][79][80] and moisture induced swelling [5][78][81] of polymers and their composites.

3.4 Environmental testing and analysis

A Q-LABQUV/SPRAY/RP chamber (Fig. 3.1) was used for individual and combined UV radiation and water condensation aging tests. The UV radiation tests were carried out for 1000 hours with the UV wavelength ranging from 315 to 400 nm at 80°C. An irradiance level of 1.50 W/m² at 340 nm was chosen to more than double the maximum irradiance of natural sunlight at noon (summer, Phoenix). The test temperature was lower than the glass transition temperatures, T_g, of the polymer matrices of the composites, which were higher than 120 °C. The relative humidity (RH) was 3 ± 2% and was recorded by a relative humidity meter placed inside the chamber.

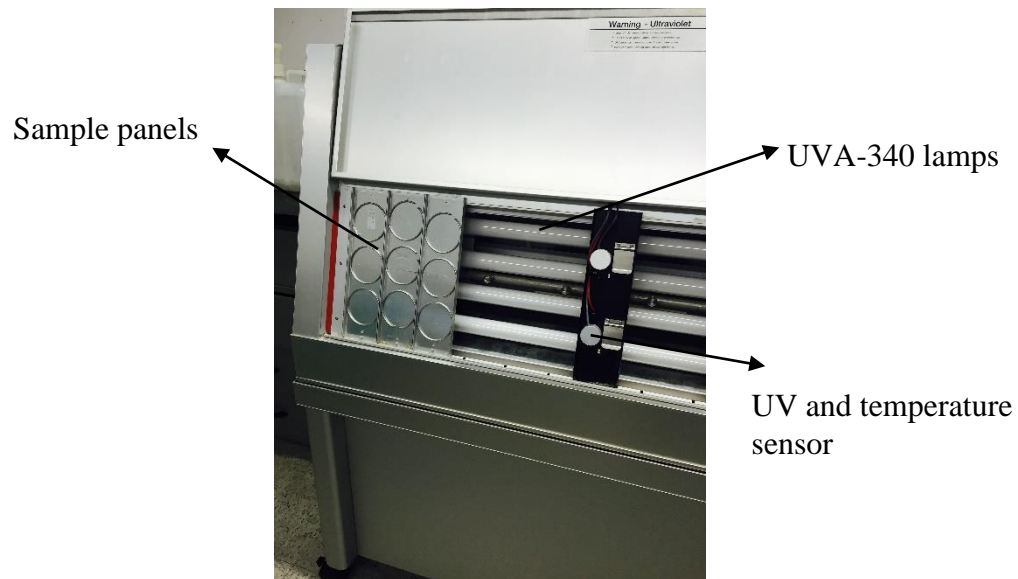


Figure 3.1. Inside of the Q-LABQUV/SPRAY/RP chamber equipped with fluorescent UV lamps.

In the water condensation tests the specimens were continuously exposed to deionized (DI) water vapor condensation at 60 °C for 1000 hours with 92 ± 2% RH. Water condensation was formed by heating deionized water to vapor on a hot panel

inside the chamber. In the cyclic UV radiation and water condensation tests, the composites were exposed to alternating cycles consisting of 16 hours of UV at 80 °C followed by 8 hours of water condensation at 60 °C for 1000 hours. The relative humidities were $33 \pm 2\%$ and $92 \pm 2\%$, respectively. The samples were mounted near vertically so that water condensation on the surfaces would run off.

For weight measurements the specimens were removed every 96 hours from the chamber for about 60 minutes and weighed with an Ohaus Voyager Electronic Balance (precision 0.01 mg). The specimens were then randomly repositioned in the chamber to ensure uniform exposure on all surfaces. The percent weight changes as a function of time were calculated using Eq. 3.1:

$$\% \text{weight change} = \frac{w_f - w_i}{w_i} \times 100 \quad \text{Eq. 3.1}$$

where W_f and W_i are the final and initial dry weights of the samples at room temperature.

Optical and scanning electron microscopes (SEM, JSM 500 LV) were used to evaluate the surface morphology of the specimens after their exposure. All specimens were prepared and mounted using conventional procedures for SEM observations. Most of the work on the surface deterioration in the composite under the above testing conditions has been reported elsewhere [67].

3.5. Tested composites and specimen preparation

The composites tested in this research are listed in Table 3.1. The exact chemical compositions of the composites were not released for the purpose of this study. Also, the matrix of composite F is proprietary information.

Table 3.1. Tested GRPs

Label	Matrix	Glass fiber	Weight fraction fiber (%)
A	Vinyl ester Epoxy	ECR-Glass 1	75
B	Vinyl ester Epoxy	E-Glass	75
C	Vinyl ester Epoxy	ECR-Glass 2	80
D	Polyester	ECR-Glass 2	80
E	Epoxy	ECR-Glass 2	80
F	Proprietary	ECR-Glass 2	80

Two groups of unidirectional GRP composites were investigated. In the first group, three composites (A, B and C) with E-glass, ECR-1 glass and ECR-2 glass fibers in a vinyl ester epoxy blend matrix were tested to evaluate the fiber effect on composites' degradation. ECR-1 glass fibers have higher content of Na_2O and larger fiber size than ECR-2 glass fibers [82]. In the second group, one type of fiber, ECR-2 glass, was considered with four different polymers, namely polyester, vinyl ester, epoxy and a proprietary resin to determine the matrix effect on the degradation processes in composites C, D, E and F. The fibers came from three different glass manufacturers and the composites were supplied by MacLean Power Systems.

1.3 m long, 6 mm thick and 50 mm wide composite plates were made by pultrusion by an outside manufacturer. The weight fractions of fibers in the six systems

were very similar (Table 3.1). Before testing, the composites were dry cut into 80 mm long specimens with special care to ensure minimum damage during cutting. The cut edges of the samples were sealed with a thin layer of a room temperature vulcanization silicone. Subsequently, the specimens were heat-treated for 72 h in an oven at 80 °C. The other as supplied surfaces of the samples were smooth and glossy before the tests.

3.6 Aging results and discussions

3.6.1 Surface erosion

Surface characteristics of all tested composite specimens after their exposures to UV, water condensation and combined UV/condensation were examined optically and by the SEM. Despite significant differences in their original surface properties such as the amounts of exposed glass fibers, fiber distributions, fiber alignment, fiber diameters, etc. [82], all composites, including A, responded in quite similar fashions to all three test environments with the exception of composite D. Therefore, A was picked as an example to illustrate the aging effects on the composites (Figure 3.2A). The polyester composite (D) had apparently UV blockers applied to its resin which resulted in less surface damage by UV (Figure 3.2D). D also had more exposed fibers on the surface (approximately 13%) in comparison with A (2.8%). In some cases the exposed fiber areas were as large as 50% (composite E).

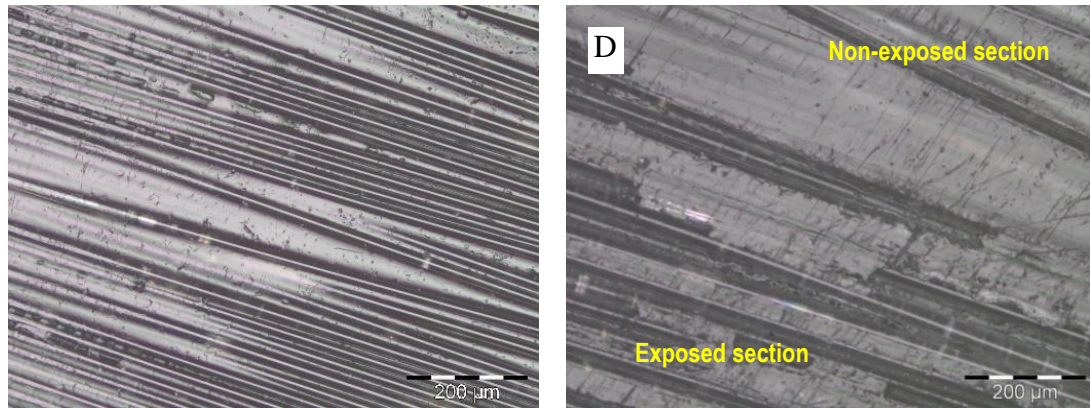


Figure 3.2. Typical surface characteristics of A and D composites after 1000 hours of exposure to dry hot UV.

Surface damage characteristics under individual UV, water condensation and combined UV and water condensation on Vinyl ester Epoxy ECR-Glass 1 – Composite A are shown in Figure 3.3 (UV only), Figure 3.4 (condensation) and Figure 3.5 (UV/condensation combination). Distinct differences in surface erosion can be observed on the surfaces subjected to the three different aging conditions.

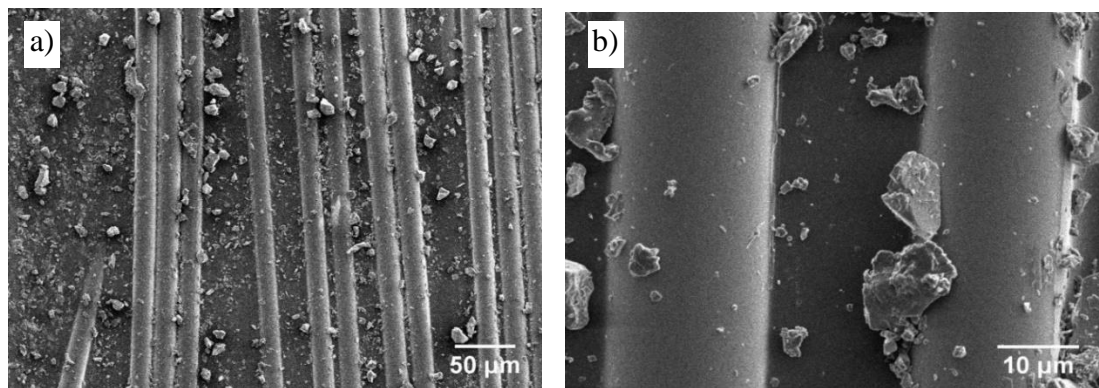


Figure 3.3. SEM images of exposed surfaces after 1000 hours of UV radiation for Vinyl ester Epoxy ECR-Glass 1 – Composite A; a) low magnification at $\times 300$ and b) high magnification at $\times 1500$.

Figure 3.3 shows severe matrix degradation with numerous small particles ranging from a micron or smaller to about 20 μm formed on the surface by chalking.

This phenomenon was caused by the polymer matrix becoming excessively brittle due to increased crosslinking or the formation of microcracking due to chain scission resulting from photo-oxidation reactions induced by UV radiation 0. The removed layer of the matrix was more than 20 μm deep. The fibers and the fiber/matrix interfaces in all composites were unaffected by UV. Previous research reported that degradation on polymers surfaces by UV is a time dependent effect where the photochemical reactions are restricted to the surface of the polymers within a several micron thick layer [83].

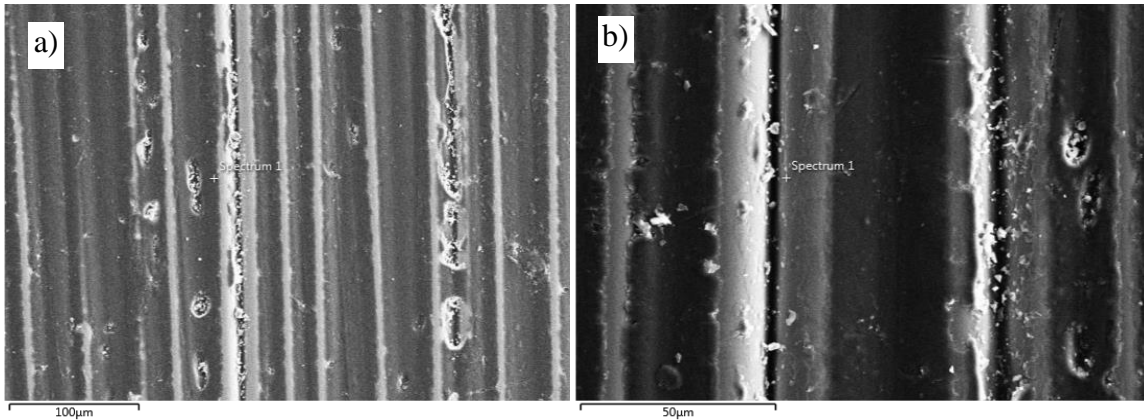


Figure 3.4. SEM images of exposed surfaces after 1000 hours of condensation for Vinyl ester Epoxy ECR-Glass 1 – Composite A. a) low magnification at $\times 300$ and b) high magnification at $\times 1500$.

The micrographs presented in Figure 3.4 indicate that the matrix and the interfaces of the composite were degraded by water condensation and the amount of degradation was not uniform across the surface. Overall the amount of damage by water for all composites was much less severe than the damage illustrated in Figure 3.3 for the UV exposure.

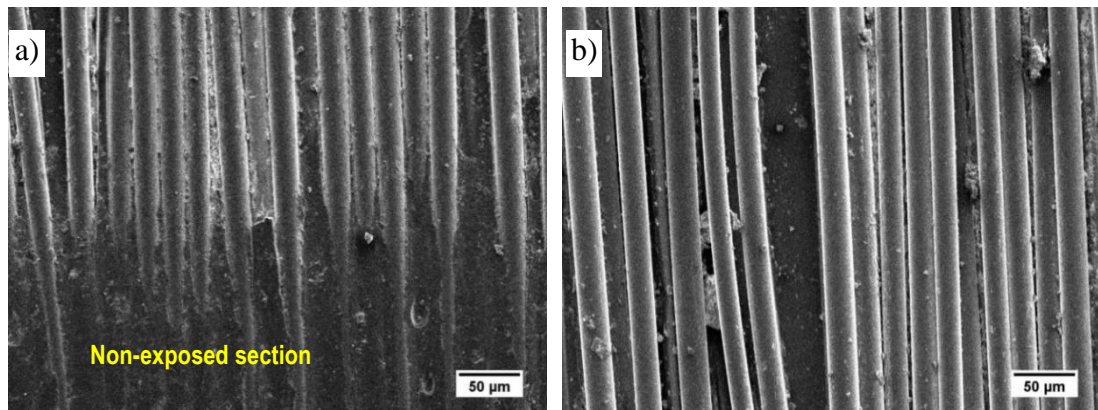


Figure 3.5. SEM images of exposed surfaces after 1000 hours of UV and condensation for Vinyl ester Epoxy ECR- Composite A.

Cyclic exposure to both UV radiation and condensation resulted in severe degradation that was very different from the other two exposures. The damage consisted of extensive matrix erosion and debonding. As shown in Fig. 3.5, the external polymer layer on the specimen surface was completely removed and the underlying glass fibers were exposed. Most importantly, all samples were almost entirely free from any particles larger than a few microns in diameter.

3.6.2 Mass changes

Figure 3.6 shows weight changes as a function of time for the composites exposed only to UV radiation. The data points for each curve represent averaged measurements obtained from two specimens. It can be observed that the specimens exhibited immediate loss in weight from the very first hours of testing. All GRPs after 1000 hours of exposure lost between 0.03 to 0.056 % of their weight. The initial decrease in the weight of the specimens can be attributed to the expulsion of volatiles and residual moisture, which occurred in the first 200 hours of testing. Then, continuous “attack” by UV radiation and

oxidation at elevated temperature was the main reason for severe matrix degradation and weight losses.

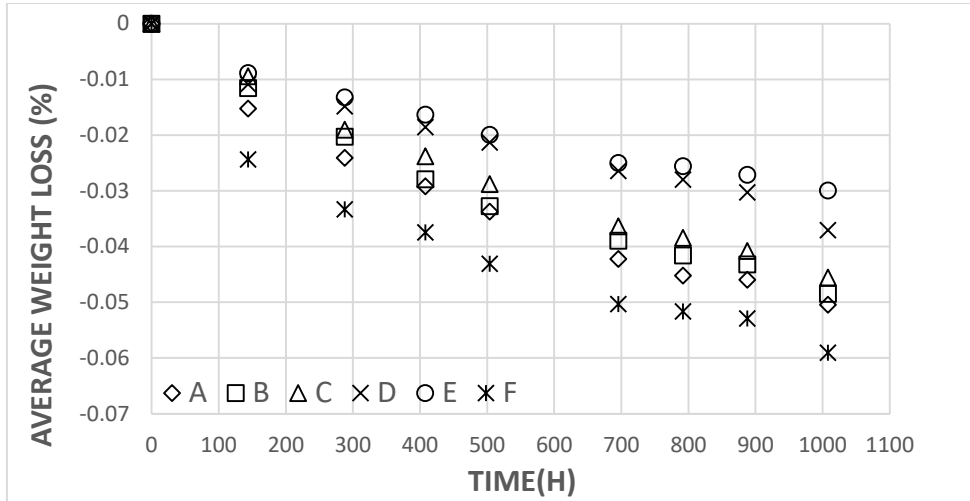


Figure 3.6. Weight changes for six composites under UV radiation as a function of time.

The effect of water condensation on the weight of the specimens was entirely different in comparison with the UV tests. As shown in Figure 3.7, all specimens gained weight with time. Again, the data was obtained from two samples for each composite. The specimens gained about 0.04-0.19% by weight after 1000 hours of exposure depending on their chemical composition without reaching saturation.

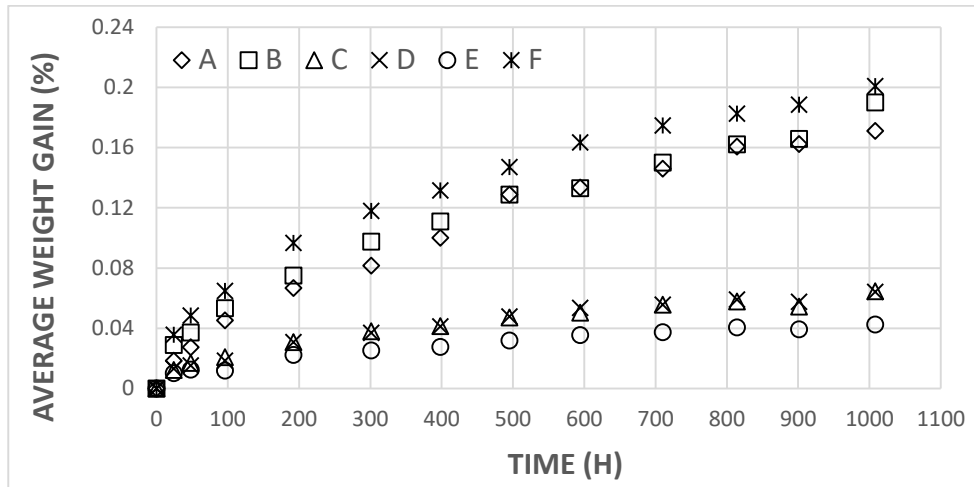


Figure 3.7. Weight changes for six composites under water condensation as a function of time.

The combined effect of UV and condensation created another set of weight gain data noticeably different than the individual UV and water condensation exposure. As shown in Figure 3.8 the specimens started to exhibit a decrease in weight after about 100 hours of exposure after initial small weight gains. The weight losses continued with increasing rates for the remainder of testing. Excluding specimen D, an average of 0.09% decrease in weight was observed after 1000 hours.

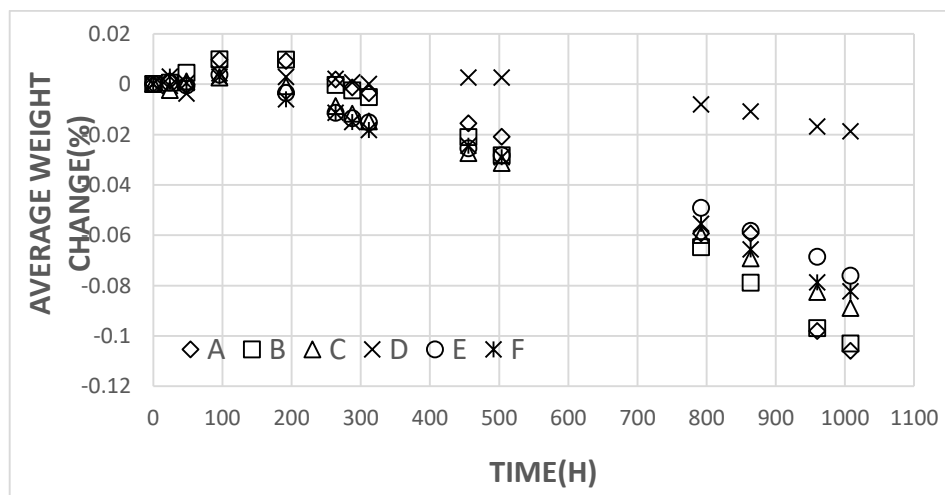


Figure 3.8. Weight changes for six composites under cyclic UV and water condensation as a function of time.

3.7 Synergistic aging effects in GRPs

3.7.1 Comparison between individual and combined exposures

Despite the fact that the six GRPs investigated in this research were based on three different glass fibers and four different polymer resins with very different surface characteristics, their individual responses to UV, water condensation and the combination of UV and condensation were quite similar. As expected, all of them lost weight under UV exposure (Fig. 3.6). Also, as expected, all of them gained weight when exposed to water condensation (Fig. 3.7). Under the combined action of both UV and condensation, all of them lost weight (Fig. 3.8). The changes in weight within the 1000 h of testing were not large but significant enough to detect the effect of the three different environments on the composites. If the sums of the weight changes under the individual exposures are compared with the changes in weight under the combined UV/ condensation condition, a very interesting effect can be observed immediately (Fig. 3.9). The sums of the individual effects on weight changes are positive and much smaller than the changes in weight under the combined environments, which are not only larger but also negative. This clearly demonstrates that the synergistic effects in the aging under UV/condensation/temperature/time of the six composites are quite strong.

The synergistic effects observed in Fig. 3.9 are even better visible in the averaged weight changes obtained from the six composites and presented in Fig. 3.10. Several important observations can be made here. First, the averages of the individual effects on the weight changes for the six composites are positive and about 50% smaller than the

averages in the weight changes from the cyclic exposures which are negative. Most importantly, the sum vs. the cyclic average of all composite relations with temperature is very similar to the relations for the individual composites. Therefore, it is possible that the observed synergistic effect is a typical feature for any unidirectional GRP composite exposed to the aging conditions of this research.

Second, the cyclic UV and water condensation resulted in the largest weight reductions, and most likely the largest amounts of damage to all six composites in comparison with the other exposures. Third, the effect of UV on the averages under UV only seems to increase with a decelerating rate. On the other hand, the cyclic effect of UV and water condensation appears to accelerate. Finally, the standard deviations of the averages from the UV tests are the smallest whereas the condensation tests resulted in the largest scatters in weight changes. Regarding the scatters, the averaged sums and averaged cyclic data for all composites are much closer to the condensation scatters than the UV scatters. Condensation alone or in combination with UV seems to create higher level of uncertainties in the composites response to aging. Most likely this is caused by a much stronger and less predictable effect of interfaces in the condensation erosion than in the UV degradation, which seems to be more predictable and dominated by the steady erosion of the matrix between the fibers.

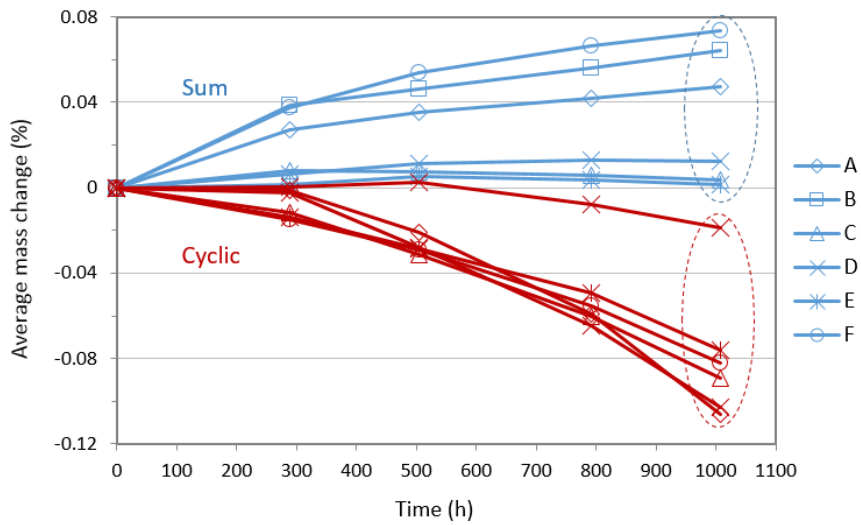


Figure 3.9. Weight changes for six composites tested under cyclic UV/condensation and the sums of weight changes under individual UV and condensation conditions with time.

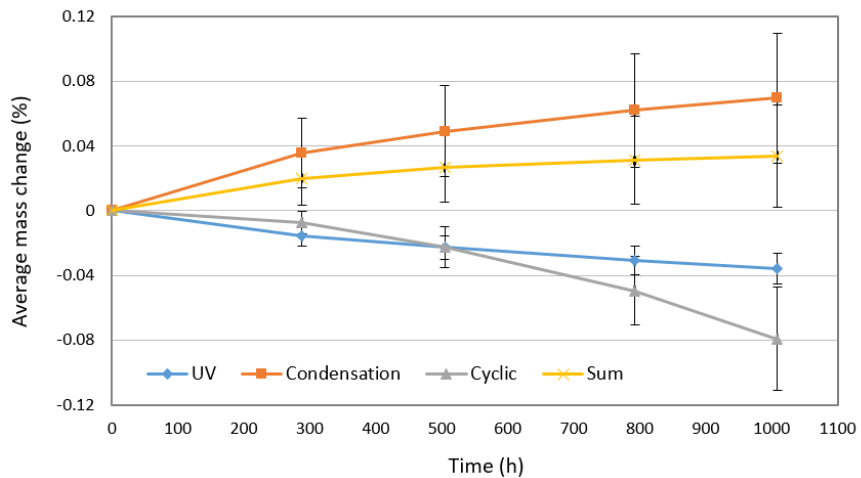
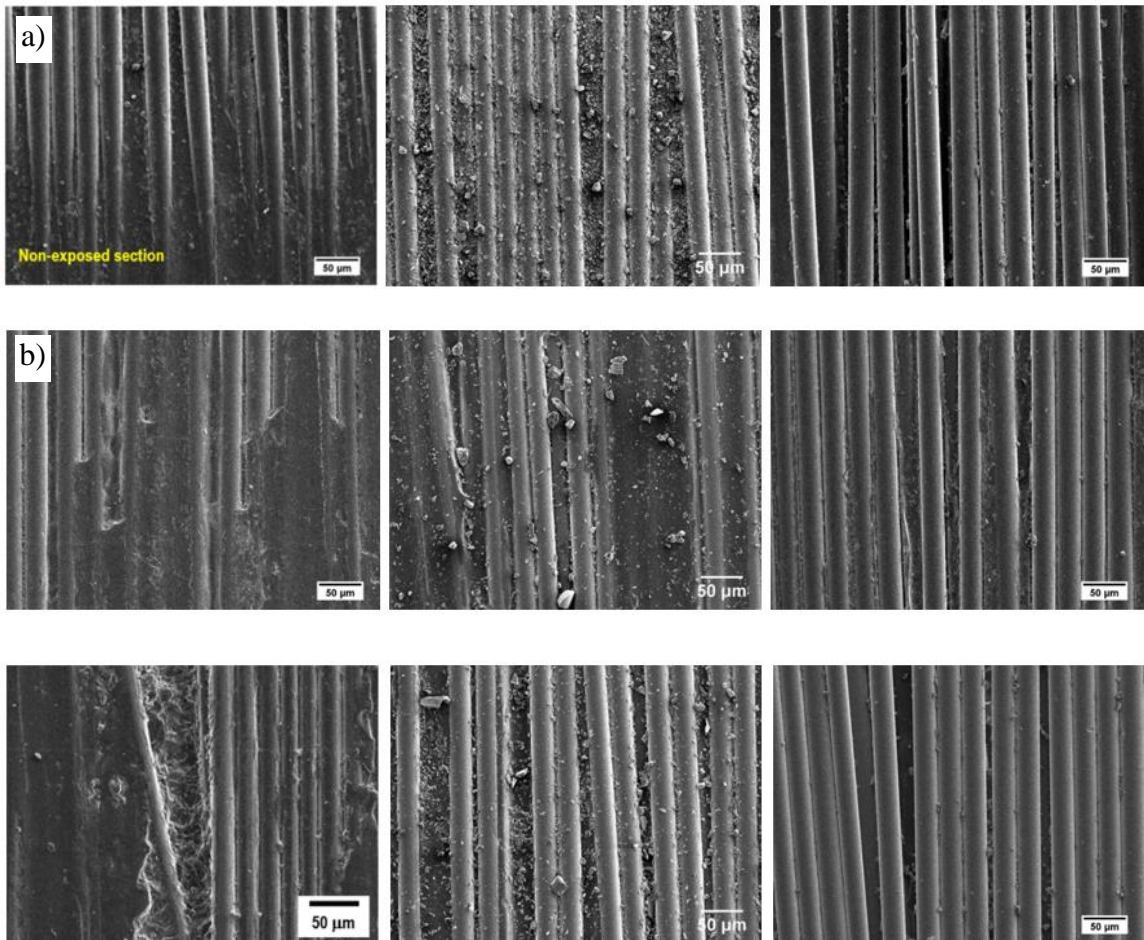


Figure 3.10. Averaged weight changes with standard deviations for six composites tested under individual UV and water condensation, cyclic UV and condensation, and the averaged sums of weight changes from the individual exposures as a function of time.

3.7.2 Summary observations of surface degradation of all tested GRP composites under synergistic aging

It has been shown above that unidirectional GRPs when exposed to individual and cyclic UV radiation, water condensation and temperature develop significantly different

degradation mechanisms with strong synergistic effects. The weight losses of polymer composites under cyclic conditions were larger than those under the individual UV and individual condensation environments. Surface morphology images of four tested GRPs have been shown in Fig. 3.11. It has been shown in Fig. 3.11 (middle and right) that UV alone can damage polymer matrix surfaces by a formation of micro-particles and that the process rapidly accelerates if slow moving water is present on the surface of the composites for debris removal purposes. Without the involvement of water the particles formed by UV tend to stay on the surfaces and prevent further development and progression of UV degradation of the underlying virgin material.



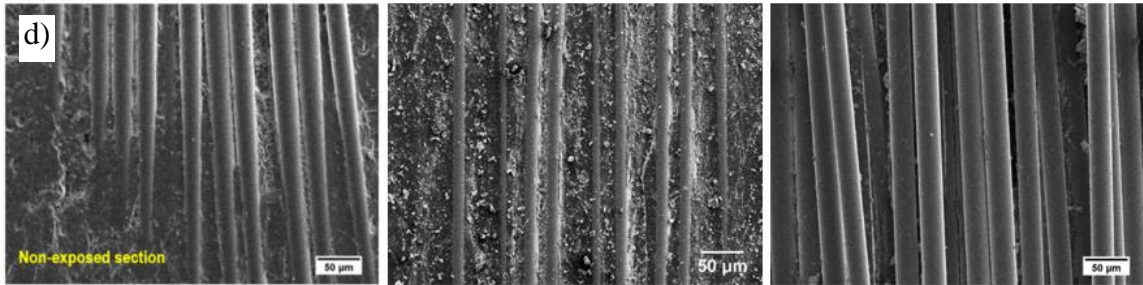


Figure 3.11. SEM images of unidirectional GFRs; before exposure (left), after UV radiation (middle) and after cyclic UV & moisture condensation (right); a) Vinyl ester Epoxy with ECR-Glass 2, b) Polyester ECR-Glass 2, c) Epoxy ECR-Glass 2 and d) PU ECR-Glass 2.

3.7.3 Summary of chemical reactions during synergistic aging of polymers

The aging process that takes place when polymer samples are exposed to UV radiation and water condensation at an elevated temperature in an accelerated environmental device, as shown in the cyclic UV radiation and water condensation tests [13], is schematically shown in Fig. 3.12.

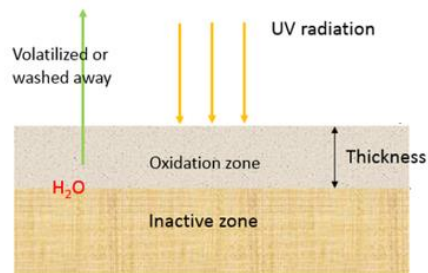


Figure 3.12. Schematic illustration of polymer sample during exposure to UV radiation and humidity.

During UV exposure, photoinitiated chain scission reactions take place, which slowly degrades the top layer of the polymer resin. At the surface, an oxidation front begins to move into the matrix. The rate of movement of this front is dependent on the rates of chemical oxidations, the solubility of oxygen in the polymer, and the rate of diffusion of oxygen into the surface. When a critical fraction of the original network chains has been broken at the surface, the surface layer is ready to be removed. After

several cycles, the rate of movement of the oxidation and ablative fronts can become equal and a stable oxidation zone thickness is established. This stable surface zone has been observed in practice for highly crosslinked polymers [17][29] and estimated by various analytical methods to be less than and close to 2 μm . Inside the sample, a much wider and oxygen-free zone and no degradation take place despite the fact that UV radiation penetrates deeper into the sample. When radicals are formed in this zone, they rapidly recombine and no damage occurs. In the stable oxidation zone, concentration gradients are established, the original matrix structure is partly damaged, and oxidation products are present. As evidenced by Nguyen et al. about 80% of the original benzene rings in the epoxy structure disappeared from the outer layer of the oxidation zone and the presence of carbonyl and amide groups increased rapidly [145].

During the water condensation stage, the polymer system has been dried at a low value of relative humidity during UV exposure cycle, hence moisture is absorbed immediately and starts to penetrate the polymer. Later due to the high value of relative humidity, numerous small water condensation droplets are formed on the surface of the oxidation zone. Furthermore, the accumulation of small water droplets eventually become a slowly moving water flow which removes those oxidation products formed in the previous UV radiation stage and leaves a fresh polymer surface exposed to the next UV radiation cycle. Therefore, even though water may be involved in the chemical reactions with radicals in the polymer, the main role of water in the entire aging process is to physically remove the oxidation products or polymer particles from the surface.

3.7.4 Preliminary synergistic aging model

In support of the above observations, a preliminary synergistic aging model for polymer and GRP composites has been proposed [13]. The UV/water flow aging model consists of two consecutive stages including: Part (A) UV radiation damage formation on polymer surfaces and Part (B) cleaning UV damage on polymer surface by moving water (Fig. 3.13). In comparison with other environmental degradation models in the section 2.2.2, it can be seen that the simulations combine an empirically based approach with a mechanistic method.

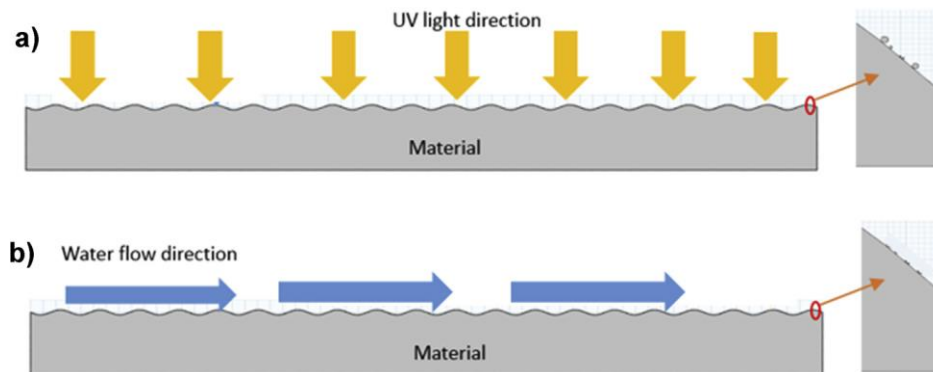


Figure 3.13. Material is exposed to the UV radiation (a), then small particles are formed on the surface, which are then washed away by water flow (b).

Two main mechanisms have been considered to explain why the surfaces of the composites after the cyclic UV/water condensation exposures are severely eroded but almost free from any visible particles (Fig. 3.5). One is based on the chemical degradation of the resins under high energy radiation conditions with oxygen, for example by the formation of hydroperoxides, a significant intermediate [20]0. Those unstable intermediates are quite active and result in chain scission and crosslinking after

complex reactions. Eventually, these chemical reactions will result in the microcracking and chalking on the exposed surface, which was shown in Fig. 3.3. During the condensation cycle, resin hydrolysis and moisture absorption occur but the resin erosion is significantly less severe [71]. In the second step, any soluble and insoluble (particles) products are removed from the ultraviolet irradiated surface by slowly moving condensation water. Then a fresh polymer surface is exposed to the following UV cycle and more damage is subsequently created by UV followed by the subsequent cleaning of the surface damage by water in the next condensation cycle.

3.8 Comparison of degradation by UVB and UVA

In addition to the synergistic degradation of GRPs under UVA and water condensation, aging by a combination of UVB and water condensation has also been investigated. The difference between the UVB and UVA radiation is that UVB comes with a shorter wavelength ranging from 280 to 315 nm and with higher photon energy than that of UVA. Therefore, compared to UVA, UVB radiation will accelerate the degradation rates of polymers and GRP composites. Development of synergistic degradation of vinyl ester epoxy composite under UVB and water condensation environment was presented in Fig. 3.14. From Fig 3.14(a) to 3.14(d), it has been clearly shown that UV induced degradation including a loss of surface gloss, surface discoloration, fiber debonding and a severe loss of resin in GRP composites. Fig. 3.15 showed that UVB can damage VE composite with a higher aging rate than that by UVA. UVB photons with higher unit energy have more options and chances to break VE chemical bonds that UVA may not be able to damage.

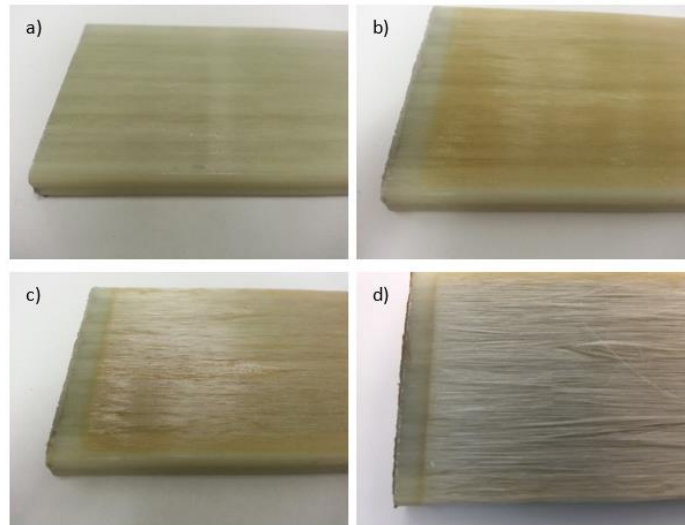


Figure 3. 14. Surface degradation of ECR glass vinyl ester epoxy composite after UVB and water condensation; a) unexposed, b) 500 hours, c) 1000 hours and d) 1500 hours.

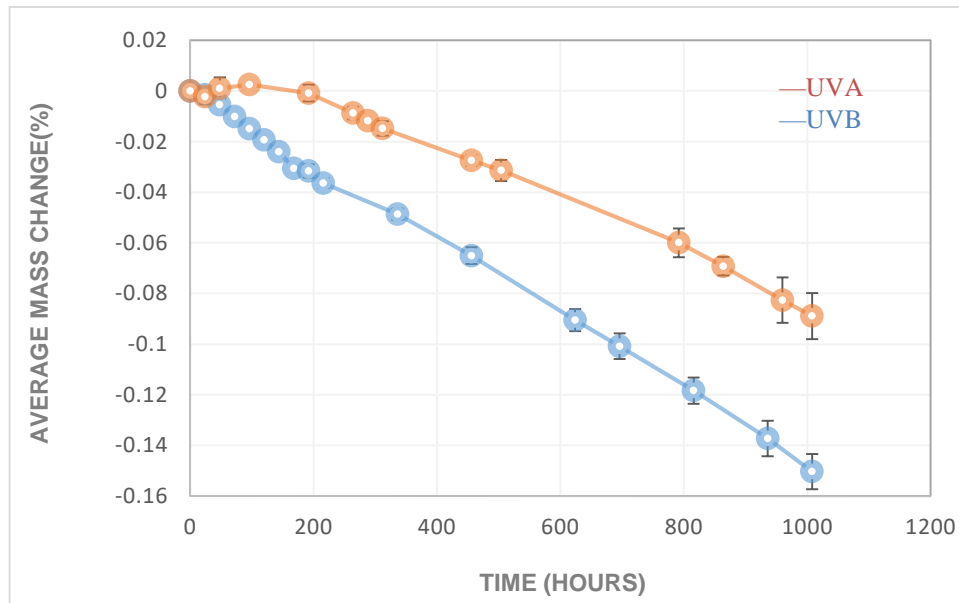


Figure 3.15. Weight changes for ECR-2 glass/vinyl ester epoxy composite under cyclic UVA & water condensation vs. under UVB & water condensation.

3.9 Surface yellowing

The discoloration was immediately observed on the surfaces of six investigated GRPs after 100 hours of UV radiation. The main reason is photooxidation resulting in the

formation of chromophoric chemical species, and which was absorbed in the visible range of light. Minor changes in surface roughness were also visible by the naked eye for all specimens exposed to UV radiation. Fig. 3.16 shows the yellowing phenomena on GRP composite surfaces. Specimen E showed that only the outer layer was affected by UV radiation and the thickness of this layer is around 10 μm [20]. That means, UV radiation alone cannot penetrate through the whole bulk and will be blocked by the outer layer.

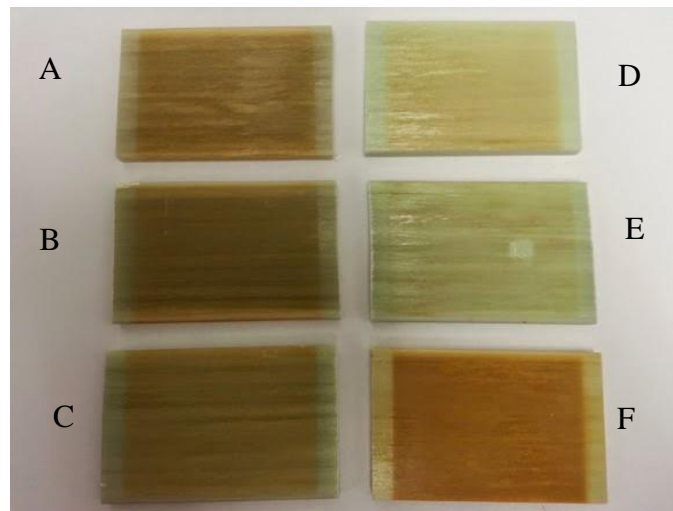


Figure 3.16. Yellowing of specimens after 1000 hours UV radiation.

3.10 Summary

It has been shown that commercially available unidirectional GRP composites when exposed to individual and cyclic UV radiation, water condensation and temperature develop significantly different degradation mechanisms with strong synergistic effects. Most importantly the sums of the individual UV and water condensation aging effects on weight changes are positive with weight gains, whereas the weight changes under the cyclic combined conditions are negative with weight losses for all six tested composites.

The average weight losses under cyclic conditions for all six composites were found to be about 100% larger than the weight gains from the simple superposition of the UV and condensation environments for the same composites. A comparison of weight changes of vinyl ester epoxy composites degraded by UVA and UVB showed that polymers and their composites could suffer higher aging rates and more damage by UVB radiation than under UVA.

To explain the synergistic effect observed in this thesis, a new hypothesis of damage initiation and progression in the GRPs subjected to both UV and water condensation was formulated and supported by a new model of synergistic aging. According to the model, under the combined action of UV and water condensation, small particles are first formed on the surfaces of polymeric surfaces exposed to UV radiation. The particles are subsequently removed by the slowly moving water caused by the condensation, which exposes fresh undamaged polymer surfaces to the cycle of UV. This creates a much more severe surface erosion than UV alone. The model has been subsequently further developed to include comprehensive modeling of UV damage on irregular polymers surfaces and a unique analysis of particle removal by water using advanced nanotechnology approaches.

Chapter 4. Polymer Degradation under UV and Water Condensation

4.1 Polymer photodegradation

It has been shown in Chapter 3 that all GRPs lost weight under individual UV exposure (Fig. 3.6). According to the literature and the previous chapter, complicated photodegradation occurred on the surface of samples which resulted in initial yellowing, discoloration and eventual chalking phenomena. Generally, the explanation for these degradations is always related to absorption of UV photons at specific wavelength and breaking of chemical bonds in polymer chains. The energy of incoming radiation is quantified such that absorption occurs in one and only one step where all the energy of a single photon is either absorbed or rejected. This restriction determines which specific wavelength of radiation is absorbed by a specific bond or group. When a UV photon is absorbed by a molecule, the molecule attains an excited state but only when the energy difference between the states before and after absorption equals $h\nu$ (the energy of the photon). The quantity of energy absorbed determines whether a bond can be broken.

Since the vinyl ester composite exhibited very severe damage under UV (Fig. 3.6), it was chosen as an example to conduct additional chemical structure analyses by using FTIR technology to investigate which sites in the chemical linkages or functional groups in polymer chains can be affected by UVA radiation. Chemical structure of a

vinyl ester (VE) monomer is shown in Fig. 4.1. Fig. 4.2 shows the structure of a VE resin.

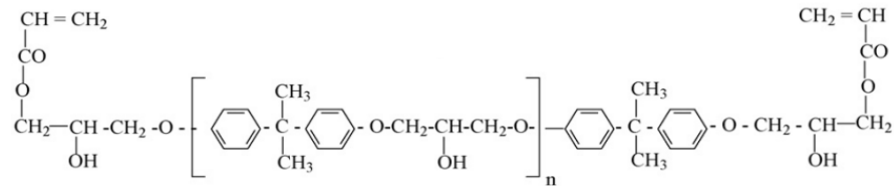


Figure 4.1. Structure of VE monomer.

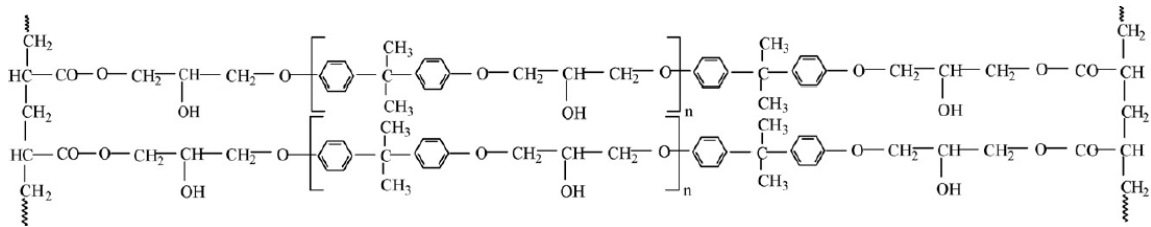


Figure 4.2. Structure of VE resin.

4.1.1 FTIR analysis on selected GRPs

FTIR spectra for the VE/ECR-1 composite before and after UV exposure are shown in Fig. 4.3 and Table 4.1. They show the characteristic infrared absorption bands of the VE polymer. In the region of $2000\text{-}4000\text{ cm}^{-1}$ (not shown in Fig. 4.3), a broadening but weak band of the O-H groups is noticed, with a peak at 3473 cm^{-1} . This band may be attributed to the formation of hydroxyl in the main chain of epoxy. Also, hydrogen bonding may occur between the matrix and the glass fiber. The bands at 2868 cm^{-1} , 2941 cm^{-1} , 2970 cm^{-1} correspond to the stretching vibrations of C-H groups such as CH_2 and CH_3 .

In Fig. 4.3, a very intense band is observed at 1730 cm^{-1} due to stretching vibrations of the C=O group. Comparing the shape of C=O bands after zero day, two days and four days UV exposure, little change has happened. That means the C=O group in VE epoxy system is very steady even after four days of UV exposure. The bands at 1609 , 1582 , 1509 and 1456 cm^{-1} observed in the spectra of cured VE sample can be assigned to aromatic rings. The peak at 1509 cm^{-1} became weaker and may result from the changing of substituents in the aromatic ring after UV exposure.

Another possibility is that the formation of various volatile products such as benzene, styrene, benzoic acid, benzaldehyde and benzophenone by photooxidation may lead to a reduction of aromatic rings [20]. Søren [9] showed that the bridge sites between two aromatic rings were easily affected by UV radiation, which will lead to chain scission.

The bands located at 1382 , 1363 cm^{-1} may correspond to symmetric deformation band of CH_3 and twist of CH_2 double bonds. The peak at 1292 cm^{-1} is due to twisting vibration of CO groups and peak at 1248 is due to twisting vibration of C-O-C. The bands around 1180 cm^{-1} are assigned to stretching of C-CO-O bonding in VE resin. Comparison of these peaks after zero, two and four day UV exposure indicates that there is a decrease in C-O, C-O-C, C-CO-O groups. Ollier et al. [84] reported that the photooxidation mechanisms of phenoxy resins mainly involved the reactivity of the

aromatic ether function. The decreases of the absorbance at 1292, 1248, 1180 cm^{-1} are due to the photolysis of the saturated ester function and ether function [77].

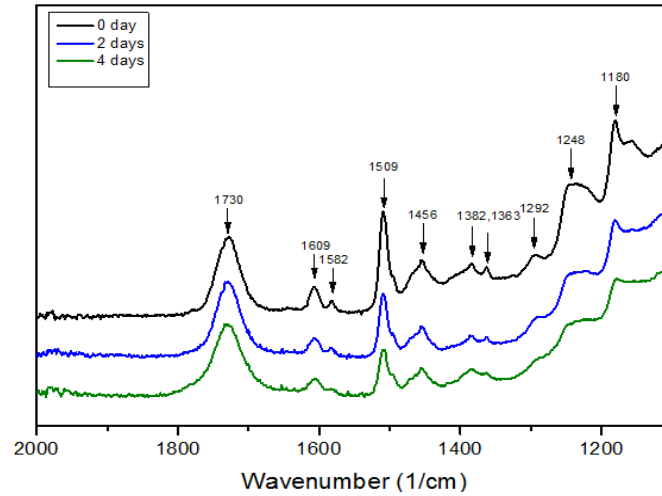


Figure 4.3. FTIR spectra of as received, exposed two days and four days vinyl ester epoxy ECR-Glass 1 fiber composite.

Table 4.1. The characteristic absorption bands of the VE in the spectra.

Absorption bands(cm^{-1})	Assignment
3473	O-H stretch
2970, 2941, 2868	C-H stretch
1730	C=O stretch
1609, 1582, 1509, 1456	Aromatic ring stretch
1382, 1363	CH_3 bend
1292	C-O stretch
1248	C-O-C stretch
1180	C-CO-O stretch

4.1.2 Possible photodegradation mechanisms in VE polymer under UV

The FTIR results presented above indicate the possible presence of the photo-oxidative degradation products such as hydroxyl groups, carbonyl groups, peroxides and hydroperoxides. The unstable hydroperoxides decompose by producing radicals that may attack the VE chains. Dan Rosu et al. [77] suggested a possible mechanism of VE photo-oxidative degradation shown in Fig. 4.4 and Fig. 4.5. This photodegradation mechanism illustrated a possible pathway to decrease ester linkage in VE resin after UV radiation. It is also explained that the weight loss of GRPs after UV radiation (Chapter 3) was caused by the elimination of volatile compounds (CO, CO₂, H₂O, etc).

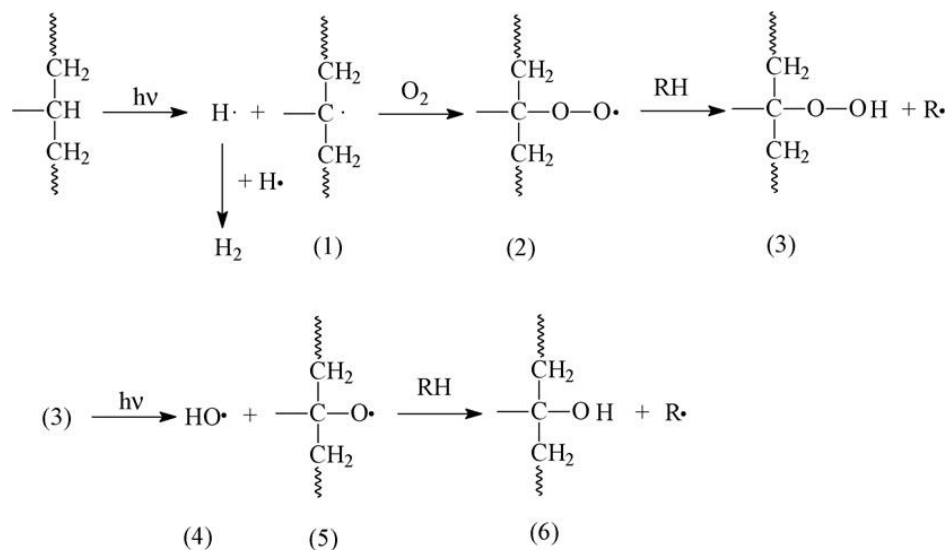


Figure 4.4. Compounds with hydroxyl groups, hydroperoxides and peroxide structures resulted during irradiation of VE resin.

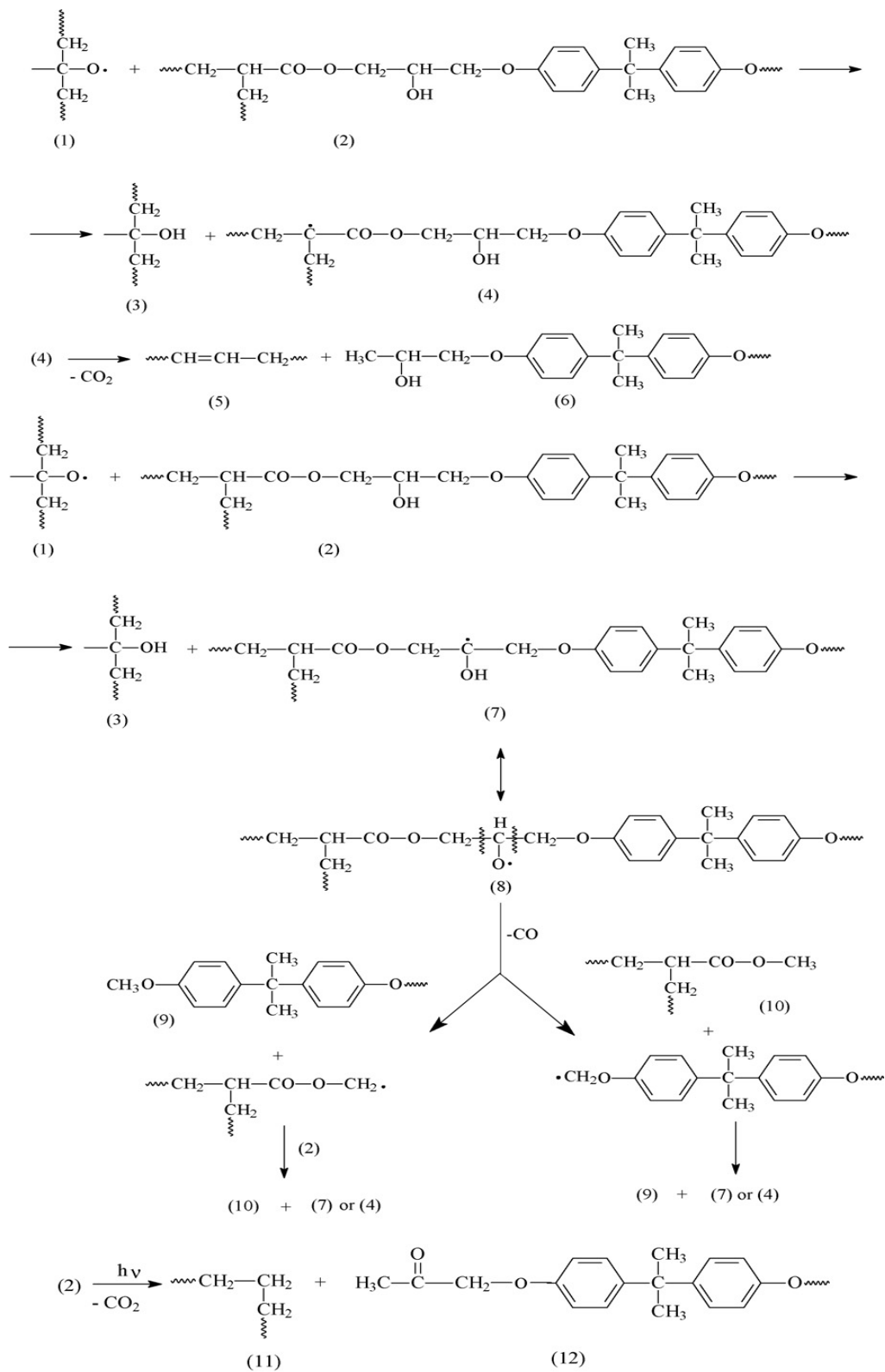


Figure 4.5. The photo-oxidative degradation mechanism of VE resin.

4.2 Synergistic aging of pure polymers

To expand the synergetic aging model to pure polymers, PVC, Nylon (66), HDPE, PC, UHMWPE and PEEK without fibers were chosen. Individual UV, water condensation, and cyclic UV and water condensation experiments were repeated in the QLABQUV/SPRAY/RP chamber and an oven. Here, the testing results from individual UV and combined UV & water condensation exposures are shown in Fig. 4.6 and 4.7. Figure 4.6 shows weight changes as a function of time for the polymers exposed only to UV radiation. It can be observed that most specimens exhibited an immediate loss in weight from the very first hours of testing excluding PC and PEEK. The polymers after 1000 hours of exposure lost between 0.01 to 0.052 % of their weight. Among all six pure thermoplastic polymers, PC exhibited the strongest UV resistance.

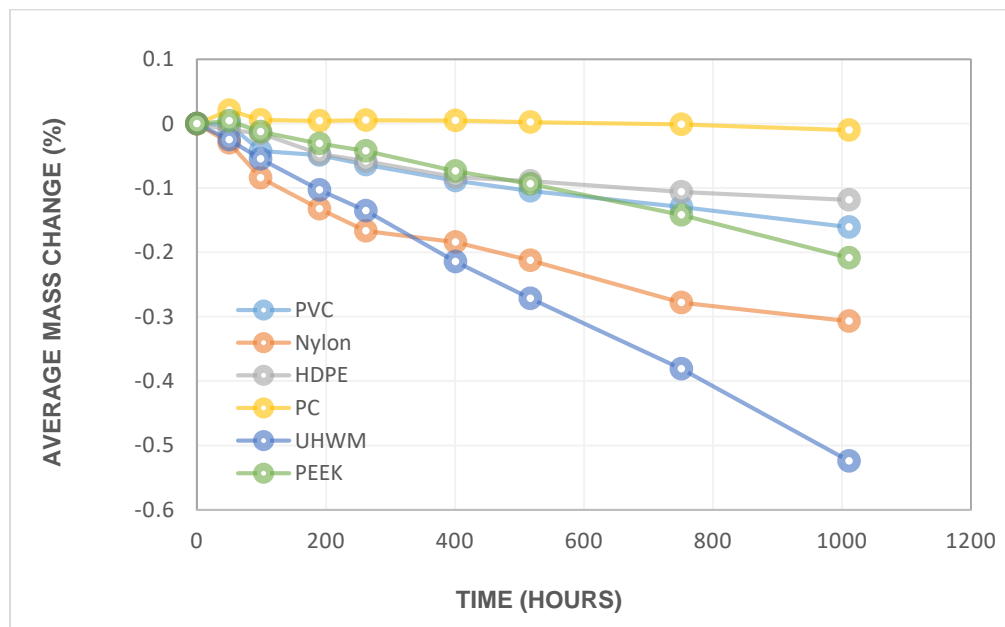


Figure 4.6. Weight changes for six polymers under UV radiation as a function of time.

As seen in Fig 4.7, the weight changes for six polymers exposed to cyclic UV & water condensation were quite similar to those for the GRPs shown in Fig. 3.8 in chapter

3. The specimens started to exhibit a decrease in weight after about 50 hours of exposure after initial small weight gains. Then the weight losses continued with increasing rates for the remainder of testing. Excluding the PVC specimen, an average of about 0.25% decrease in weight was observed after 1000 hours.

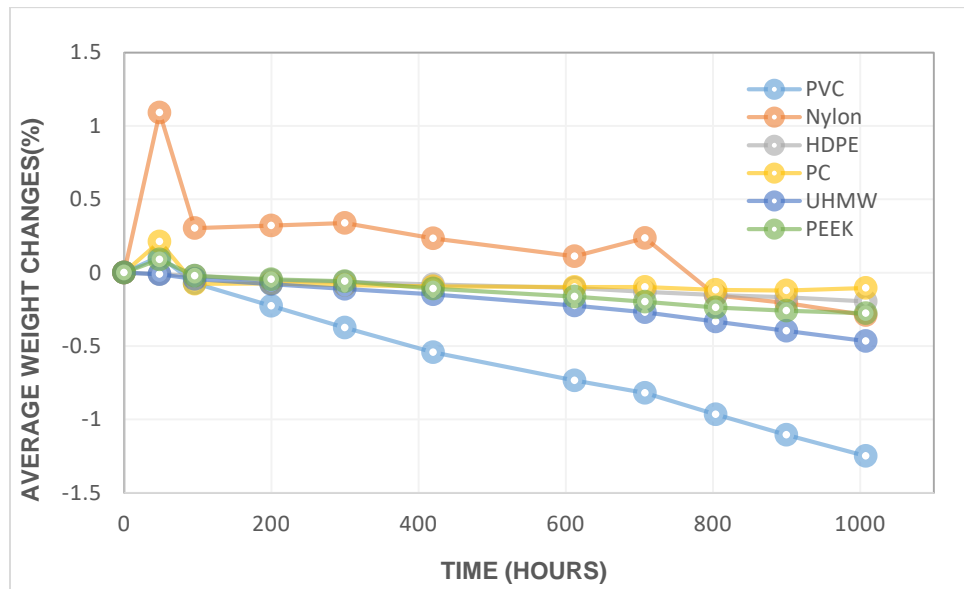


Figure 4.7. Weight changes for six polymers under cyclic UV and water condensation as a function of time.

Synergistic effects presented in pure thermoplastic polymers under a combination of UV and moisture are not as obvious as in the GRP composites. Comparing weight changes for six polymers under individual UV and cyclic UV & water exposure, only PVC exhibited a noticeable difference whereas the other five polymers exhibited tiny differences. One possible explanation is that those thermoplastic polymers have excellent UV resistant property and they respond to UV/moisture differently. Therefore, longer UV exposure time could be suggested. Another possibility is that glass fibers embedded in polymers may accelerate the synergistic aging process just like in the case of the GRP composites tested in this study. Glass/fiber interfaces are always easily affected by water

and by different thermal expansion coefficients of glass fibers and polymer matrices. This may make the formation of microcracks and sequentially micro-particles easier on the surfaces of GRP composites.

As only the PVC system exhibited clear synergetic degradation under UV and water condensation environment, its surface morphology is been shown in Fig. 4.8. It can be seen in Fig. 4.8(b) that the PVC surface was damaged by UV radiation which eventually led to the formation of micro particles on its surface. The particles stayed on the surface and prevented further development and progression of UV degradation. However, with the involvement of slow-moving water, the particles formed by UV were rapidly removed exposing the virgin material, as shown in Fig. 4.8(c). The fresh PVC surface was exposed to the following UV cycle and more damage was subsequently created by UV followed by the subsequent cleaning of the surface damage by water in the next condensation cycle.

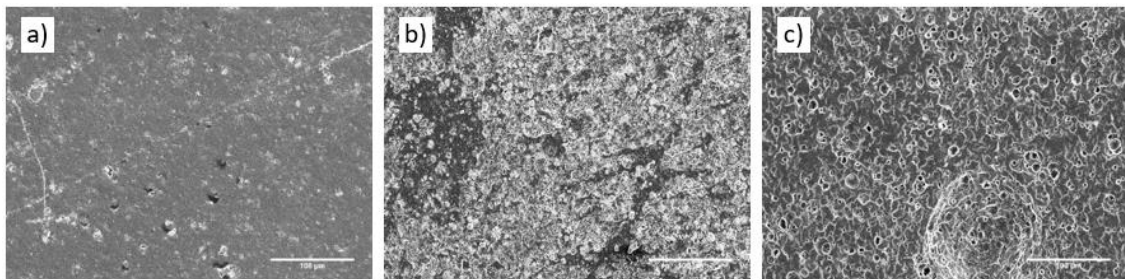


Figure 4.8. SEM images of pure PVC polymer; a) before exposure, b) after UV radiation and c) after cyclic UV & moisture condensation.

4.5 Summary

In this chapter, polymer degradation under UV and water has been discussed. FTIR analysis shows that photodegradation of VE resin led to a decrease of C-O, C-O-C,

C-CO-O groups in VE polymer chains. Based on the decrease of these linkage groups, a potential degradation mechanism was proposed for the VE resin. It has been shown that all tested pure polymers except for PVC, when exposed to individual and cyclic UV radiation, water condensation and temperature do not develop significantly strong synergistic degradation. The average weight losses under cyclic conditions for five tested polymers were found to be similar to the weight loss from the individual UV environment for the same polymers. Aside from the possibility of excellent UV resistance of these thermoplastic polymers, pure polymers have no interfacial problems caused by embedded fibers which could be another explanation for the difference.

Chapter 5. UV Degradation Model for Polymers and Polymer Matrix Composites

In chapter 3, synergistic environmental degradation of glass reinforced polymer composites was examined and a novel synergistic aging model was preliminarily proposed. In this chapter, a new model is proposed just for the UV portion of damage for polymers and PMCs supporting the first stage of synergistic aging hypothesis [13]. Flat and sinusoidal polymer surfaces were numerically simulated for their UV damage as a function of UV intensity, surface topography, and exposure time. Experimentally determined UV degradation rates for a unidirectional glass/epoxy composite were used to predict numerically the local rates of material degradation on sinusoidal epoxy surfaces subjected to UV. This allowed us to show that UV damage on uneven polymer surfaces reduces their surface roughness, making them smoother, and that the degradation rates are the largest at the tips of the local heights of the surfaces. This was subsequently verified experimentally by exposing neat epoxy specimens to UV in air at 80 °C for 1000 hours and by precisely monitoring their surface topography as a function of time. It was found that the surface roughness of the epoxy was reduced by about 12.5% and that UV affected the local peaks on the surfaces of the specimens more than the valleys.

5.1 Introduction

Extensive research has been performed on systematic experimental evaluations of degradations mechanisms in polymer coatings, polymer resins and PMCs after long-term artificial UV exposures [11,14,15,21,35,57,61,69,70,86-96]. However, few studies have concentrated specifically on the development of analytical models of UV aging of polymeric materials [11,61,69,70,90,91]. For a polymer subjected to UV radiation, photolysis and photo-oxidation are the main damage mechanisms. Photo-oxidation includes the photochemical production of electronically excited oxygen [92]. The activation processes initiated by UV photons excite states in macromolecules which lead to surface discoloration, yellowing and a loss of surface gloss [93][94]. Further exposure to UV light results in the formation of a thin layer consisting of loosely adherent particles called chalking [13][57][95][96]. Depending on the type of a polymer, flaking of surface resin, pitting and microcracking may also occur [35][89]. In addition, chemical aging such as chain scission by UV will result in a loss of low molecular weight or highly volatile products, which can vaporize very quickly at elevated temperature [20][92].

Most current environmental aging models for polymers and PMCs are limited to one individual degradation factor such as UV light, elevated temperature, water diffusion and others [5-10]. Few studies have concentrated on synergistic aging under multiple aging conditions involving UV [14-17,19,20,29]. It was shown, for example in [14,15], that the combined cyclic UV-temperature-moisture conditions resulted in severe damage to the polymer matrices of several different GRPs, and that the damage under the cyclic

conditions was more severe than under consecutive but non-cyclic UV and water conditions. It has also been concluded in [13] that UV alone can damage GRP surfaces by a formation of micro-particles, as shown in Fig. 5.1(a), and that the process rapidly accelerates if slow moving water is present on the surface of the composites for debris removal purposes (Fig. 5.1b). Without the involvement of water, however, the particles formed by UV tend to stay on the surfaces and prevent further development and progression of UV degradation of the underlying virgin material [13][14]. At the same time water alone does not cause much degradation in comparison with UV [13][72]. The strong UV/water condensation aging of the composites observed in [13] has been recently supported by a comprehensive particle removal model [14].

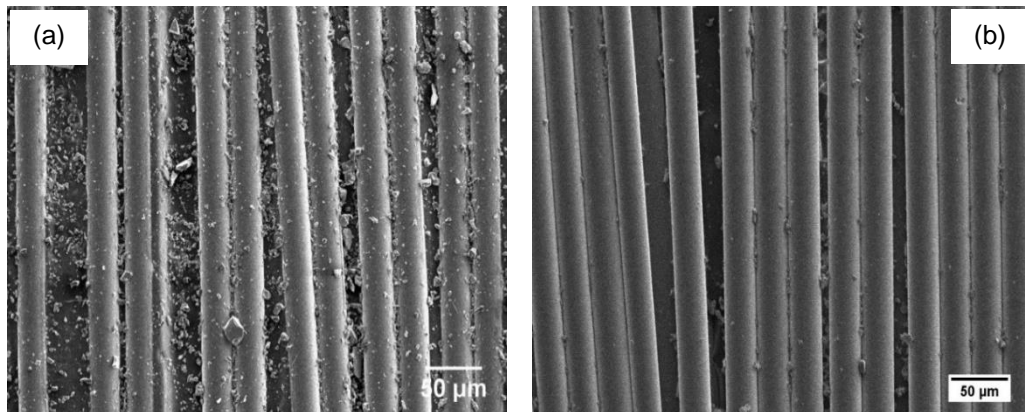


Figure 5.1. SEM images of unidirectional ECR-glass/epoxy composite; a) after UV radiation and b) after cyclic UV & moisture condensation [13].

In this Chapter, I am suggesting another model, which could further contribute to the understanding of the synergistic aging process of polymers involving UV. In particular, I am showing (1) how to properly simulate UV damage on wavy polymer

surfaces typical of unidirectional composites, (2) how to predict UV degradation rates of polymers, in general, and (3) how the surface topographies of polymers change with time under UV exposure.

5.2 Fundamentals of proposed UV degradation model

In this study, the degradation mechanisms on polymeric surfaces exposed to UV were investigated with the assumptions that the air temperature, humidity and UV radiation intensity were all constant. It was also assumed that the modeled polymer surfaces were free from photon stabilizers, antioxidants, or other additives, and that the contributions from individual wavelengths were independent, also neglecting reflection of the parallel-beam of UV light. Only a fraction of absorbed photons led to photolytic activity, and the photo recovery effect was neglected. The UV radiation intensity received by simulated material surfaces corresponded to the UV tests performed in [13]. Also, no thermal degradation was incorporated and the initial surface profiles were either flat or sinusoidal.

Photodegradation of polymeric surfaces by radiation fields can be estimated by using the cumulative damage model, which has been widely accepted in medical and biological studies [19]. Here, an approximate function of the total effective dosage is given by equation 5.1 according to the accumulative dosage model [10][11].

$$D_{total}(t) = \int_0^{\tilde{t}} \int_{\lambda_{min}}^{\lambda_{max}} E_o(\lambda)(1 - e^{-A(\lambda)})\phi(\lambda)d\lambda dt \quad \text{Eq. 5.1}$$

where: λ_{min} and λ_{max} are the minimum and maximum photolytically effective wavelengths (nm). $A(\lambda)$ is the absorbance of the sample at specified UV wavelength, (dimensionless). $E_o(\lambda)$ is the incident spectral UV radiation dose to which a polymeric material is exposed to (W m^{-2}). $\phi(\lambda)$ is the quantum yield, which is the number of times a specific event occurs per photon absorbed by the material. The "event" is typically a kind of chemical reaction, (dimensionless). t is the elapsed time and \tilde{t} is the total radiation time (unit in seconds). $D_{total}(t)$ is the total effective dosage (J m^{-2}) that caused chemical reactions in the absorber.

It is assumed here that there is no UV radiation transmitted through the sample, therefore the sample can be considered infinitely thick. By the Lambert-Beer law (equation 5.2) [19], it is found that $A(\lambda)$ is infinitely large if $I(\lambda)$ is close to zero.

$$\ln \left(\frac{I_o(\lambda)}{I(\lambda)} \right) = A(\lambda) \quad \text{Eq. 5.2}$$

where $I_o(\lambda)$ is the intensity of the incident light at wavelength λ , $I(\lambda)$ is the intensity of the transmitted light at wavelength λ , and $A(\lambda)$ is the absorbance at wavelength λ . Therefore, the probability of absorption of UV photons by a material is 1 ($e^{-A(\lambda)} \approx 0$). The total effective dosage function is simplified to Eq. 5.3.

$$D_{total}(t) = \int_0^{\tilde{t}} \int_{\lambda_{min}}^{\lambda_{max}} E_o(\lambda, t) \phi(\lambda) d\lambda dt \quad \text{Eq. 5.3}$$

According to Martin et al. [11], different incident wavelengths have different quantum efficiencies.

It is assumed in this research that the only photosensitive group in the aromatic epoxy network is phenoxy which only absorbs in the interval 300-340 nm and that the quantum efficiency for this effective absorbed wavelength is 10^{-4} [9]. Equation 5.3 can then be simplified further into equation 5.4.

$$D_{total}(t) = E_o \times \phi \times t \quad \text{Eq. 5.4}$$

In most cases there is an angle between the incident light and the sample surface [97]. The intensity of irradiation is therefore determined by equation 5.5, where I_o is the incident intensity of UV light ($\text{W}/\text{m}^2 \cdot \text{s}$) and θ is the angle between the UV light and the normal to the surface.

$$E_o = I_o(\lambda, \theta, t) \cos(\theta) \quad \text{Eq. 5.5}$$

The relationships between UV damage to polymeric materials and the radiation dosages can be approximated by a linear response (equation 5.6), a power law response (equation 5.7), or by an exponential response (equation 5.8) [19].

$$\Gamma = cD_{total} \quad \text{Eq. 5.6}$$

$$\Gamma = c D_{total}^b \quad \text{Eq. 5.7}$$

$$\Gamma = c e^{bD_{total}} \quad \text{Eq. 5.8}$$

where c and b are empirical constants, and Γ is any quantitative critical material performance characteristic such as specimen thickness, stiffness, toughness, etc. In this study, the linear response (equation 5.6) has been applied in the UV simulation assuming

that the damage characteristic, Γ , is represented by changes to specimen thickness by UV degradation on unit area. Therefore, Γ becomes $H_i - H_f$ and equation 5.6 becomes:

$$H_f = H_i - c D_{total} \quad \text{Eq. 5.9}$$

where H_i and H_f are the initial and final specimen thicknesses before and after UV exposure, respectively.

Polymer surfaces can be highly irregular. Especially in the case of PMCs, surface roughness can be significant and is increased by the presence of surface glass fibers [13]. For simplicity, sinusoidal surface shapes have been assumed in this work. The numerical differentiation method has been adopted to simulate the degradation of a surface as a function of UV exposure. In order to find a relationship between the depth changes and the exposure time (dy/dt), we have expressed the depth change rate of a surface profile as a linear function of its slope and a coefficient, α , (equation 5.10). Also, by substituting equations 5.4, 5.5, 5.6, 5.9 and $dy/dx = \tan \theta$ into Eq. 5.10, we can find the correlation between ' α ' and the coefficient ' c ' as shown in equation 5.11. For any point, x_i , along the surface, θ in equation 5.5 can be calculated from dy/dx . Then the irradiation E_o on this inclined surface can be determined from the same equation. Fig 5.2 shows the incident beam direction on a sinusoidal surface.

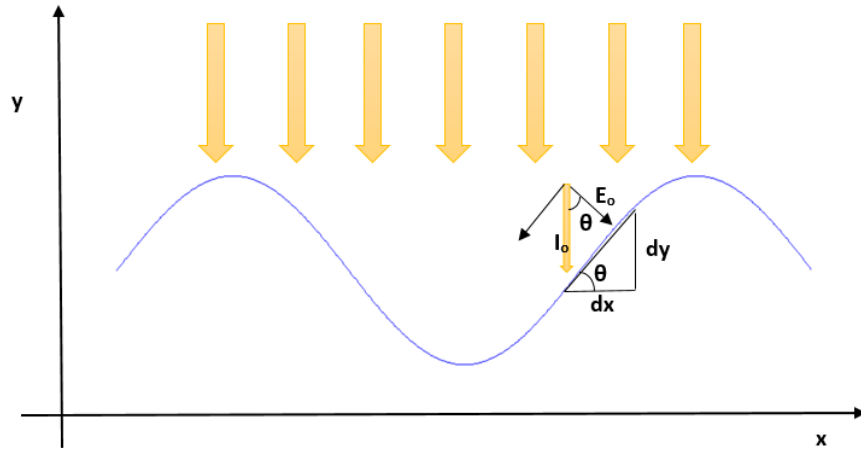


Figure 5.2. Schematics of incident beam direction on a sinusoidal surface.

$$\frac{dy}{dx} = \alpha \frac{dy}{dx} \quad \text{Eq. 5.10}$$

$$\alpha = c \cdot \phi \cdot I_0 \cdot \frac{\cos\theta}{\tan\theta}, \quad 0^\circ < \theta < 90^\circ \quad \text{Eq. 5.11}$$

In order to solve equation 5.11 in MATLAB, firstly, a symmetric, sinusoidal curve was evenly divided into a number of elements with a constant length dx . The forward difference and backward difference methods were used to calculate the slope of the first and the last nodes by equations 5.12 and 5.13, respectively. The derivatives of the remaining nodes were computed by the centered difference scheme (equation 5.14) to improve the numerical accuracy. Then, the lengths of all segments were computed from the slopes obtained from the previous steps. Finally, the irradiation distributions were determined from the irradiation amounts for all segments (computed by equation 5.5) divided by the length of the segments.

$$y'(x_i) = \frac{y(x_{i+1}) - y(x_i)}{\Delta x} \quad \text{Eq. 5.12}$$

$$y'(x_i) = \frac{y(x_i) - y(x_{i-1})}{\Delta x} \quad \text{Eq. 5.13}$$

$$y'(x_i) = \frac{y(x_{i+1}) - y(x_{i-1})}{2\Delta x} \quad \text{Eq. 5.14}$$

Since the relationship between UV damage to a polymer material and a radiation dosage has been defined as a linear function through equation 5.6, the depth function $y(x)$ can be updated by subtracting a correction term during each step (equation 5.15). Furthermore, this iteration can continue over a certain amount of time to eventually reach a final result.

$$y(x_i, t + dt) = y(x_i, t) - aE(x_i, t)dt \quad \text{Eq. 5.15}$$

For the orthogonal angle between UV light and a surface, there is a maximum UV irradiation associated with the maximum degradation rate. This is the reason why at the peaks and the valleys of the sinusoidal surface the degradation rates are at a maximum while those at the locations where the angle of inclination is 45° are at a minimum.

5.3 Experimental estimation of UV damage parameters

The UV degradation model presented in the previous section and in section 4 assumed that the polymer surface material damaged by UV is removed layer by layer, therefore reducing the thickness of the specimen with time. It also assumed that the rate of degradation (or the efficiency of UV damage formation) depended on the “ c ” parameter, which linearly relates the degradation rate to a dose of radiation (D_{total} in equations 5.4 and 5.6) necessary to damage a small critical volume of the material. If this

condition is satisfied, the small critical volume is immediately removed numerically from the surface without a trace. This can be accomplished relatively easily numerically. Physically, however, this is a much more complicated process. If the critical volume absorbs a required dose of radiation, then the volume would have to be physically removed from the surface. Even on perpendicular surfaces, most UV generated polymer particles do not fall off and tend to stay on the surface by adhesion [13][14]. If they are sufficiently large, they can be removed quite efficiently by slowly moving water [14]. In the absence of water, the particles would stay on the surface, protecting the underlying virgin polymer material against UV, and significantly slow down the rate of degradation. It can also be assumed that after receiving a critical dose of UV radiation small volumes of the surface material, are “removed” by evaporation (volatiles) or by shrinkage, especially if a UV test is performed at elevated temperature. Shrinkage and evaporation could occur independently from the volume removal by the micro particles, or in conjunction. In this section, I am showing how to handle the “perfect removal” of the critically damaged surface material by measuring the mass loss of a UV exposed specimen. If the mass loss is significant, the rate of degradation, c , can be estimated and related linearly through equation 5.6 to a change in specimen thickness. However, if the mass loss is small, then the rate of degradation would have to be estimated differently, for example, by directly measuring changes in specimen thickness. This much more accurate approach is demonstrated in chapter 5.5.

In [13] individual and combined UV radiation and water condensation aging tests were conducted in an environmental aging chamber on a unidirectional glass fiber/epoxy composite with an area fraction of exposed fibers of about 50.1%. The UV radiation tests were carried out for 1000 hours with the UV wavelengths ranging from 300 to 400 nm at 80°C. An irradiance level of 1.50 W/m² at 340 nm was chosen. The test temperatures under UV and water were lower than the glass transition temperatures, T_g, of the composite, which was above 120 °C. The relative humidity (RH) was 3 ± 2% under UV. In addition to using the already published data for the composite, UV aging tests were also conducted in this work on neat relatively flat PVC samples under identical conditions to evaluate their mass losses under UV and temperature separately. T_g of the tested PVC was about 80 °C. The composite and PVC specimens had the same dimensions. This allowed us to estimate the level of degradation of the wavy composite samples and the flat PVC samples, and to determine the c values for equation 5.6 from two different polymeric materials, separately.

The average mass changes of the epoxy based polymer composite and the PVC samples under UV radiation and at 80 °C alone for 1000 h are shown in Figs. 5.3(a) and 5.3b. The mass loss slopes seem to become less steep with time in both cases. This can be attributed to the reductions in the amounts of available volatiles with time under heat and UV and heat alone. It can also be attributed to the presence of polymer particles adhered to the surface and exposed glass fibers under UV preventing further degradation of the material underneath (Fig. 5.1a). The same effect was observed for the PVC after UV

radiation, which by the way, lost more mass after 1000 hours. The fact that the PVC samples were affected by UV more could be explained by their, perhaps lower resistance to UV radiation but also by a larger surface area of the polymer exposed to UV in PVC (100%) vs. about 50% for the composite. The percent exposed area of the polymer in the composite was determined from the experimentally measured fiber surface area exposures [67].

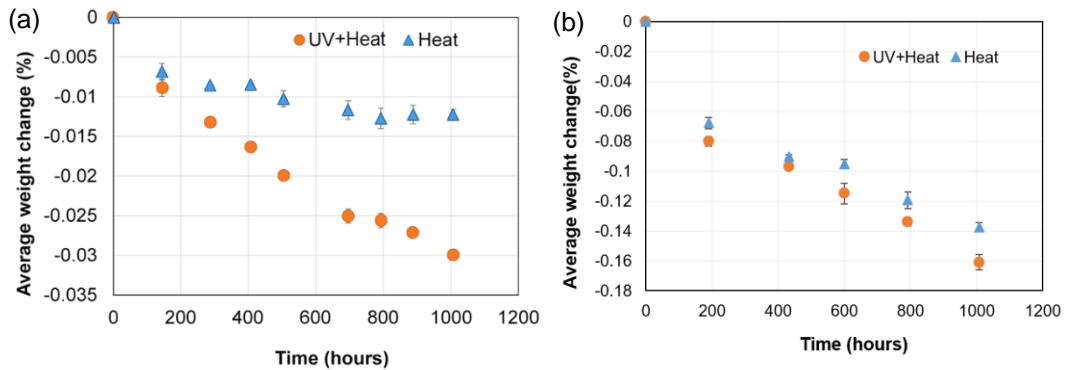


Figure 5.3. Average weight changes of epoxy polymer composite (a) and PVC (b) samples at 80 °C with and without UV.

Under 80 °C alone both materials lost mass because of the evaporation of volatile organic compounds. It appears that more volatiles were lost under temperature alone from the PVC samples than from the composite. As seen in Fig. 5.3, the average weight loss of the composite samples caused by the thermal condition was almost half of the total weight loss under UV radiation at the same temperature. The weight loss due to temperature of the PVC samples was larger in comparison with the UV caused loses.

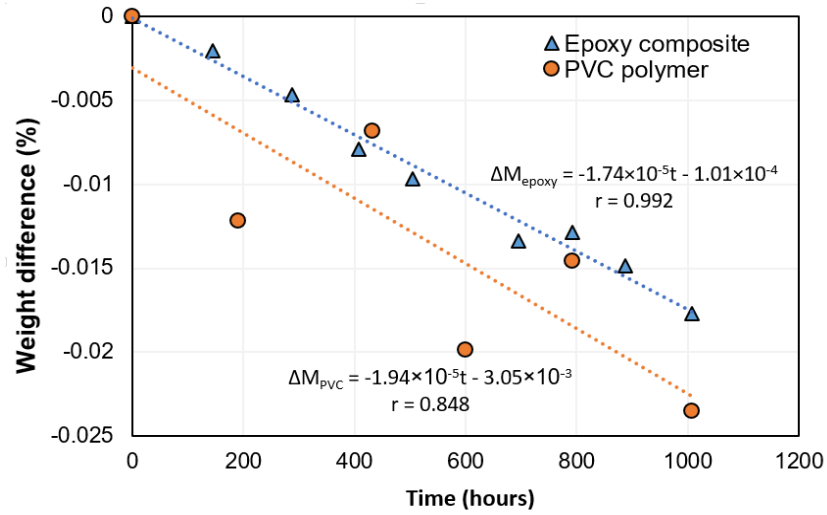


Figure 5.4. Estimated weight changes of epoxy composite and PVC polymer samples by UV radiation condition for 1000 hours after subtracting the 80 °C heat effect in Fig. 5.3.

It is stipulated here that the mass loss caused by the removal of a “solid” UV generated substance from the composite and the polymer is the result of the mass change under UV minus the mass change under the thermal condition. Therefore, linear curve fitting was used to obtain the estimated value of “c” in equation 5.6 for the two materials from the difference in the mass losses due to UV and to temperature. The c values are the slopes of the curves in Fig. 5.4. The slopes were found to be close but different. For the modeling analysis, the c value was considered to be 2×10^{-5} . It is also assumed that the changes in specimen thickness are directly proportional to the amount of degradation and are linearly dependent on time. Therefore, the changes in specimen thickness can now be related to time for the assumed E_0 and Φ values according to equations 5.4 and 5.16.

$$H_f = H_i - 2 \times 10^{-5} D_{total} \quad \text{Eq. 5.16}$$

5.4 Simulations of UV radiation on polymeric surfaces

The UV degradation model developed in this thesis and already published in [98] required certain physical constants as the input parameters in the subsequent numerical simulations of UV damage. Quantum yield, Φ , was taken from literature [9] whereas the others were obtained from the experiments described above. All used physical constants are listed in Table 5.1.

Table 5.1. Physical parameters required for the UV radiation simulations.

Parameter	Value
Sensitive wavelength, λ	300-340 nm
Radiation intensity, E_0	1.5 W/m ²
Quantum yield Φ	10 ⁻⁴ [9]
Exposure time, t	1000 hours (3.6×10 ⁶ s)
Exposure area	3.25×10 ⁻³ m ²

5.4.1 Radiation angle effect on flat surfaces

If we assume that a flat polymer sample with an initial thickness of 1 mm is subjected to UV in two directions (perpendicular and at 45°) for 1000 h, the thickness reduction of the sample will change for the two exposure directions according to the simulated data shown in Fig. 5.5. As expected the thickness reduction of the samples exposed perpendicularly is larger than that for a 45° exposure by an expected factor of $1/\cos(45^\circ)$.

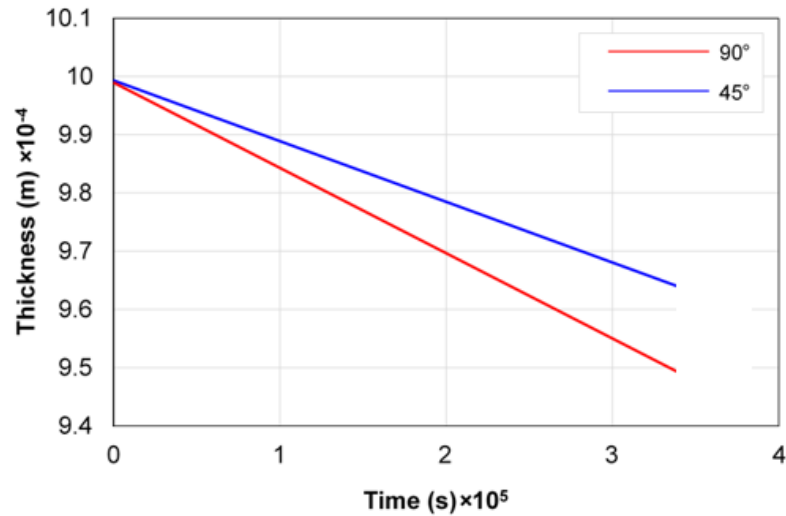


Figure 5.5. Thickness reduction rates with respect to time under different radiation angles (in degree).

5.4.2 UV radiation damage of sinusoidal surfaces

The stages of polymer degradation from an initially sinusoidal surface, based on equation 5.15 are shown in Fig. 5.6. A much larger value of parameter ‘ a ’ in Equation 5.15 was used (0.01) to accelerate the rates of numerical photodegradation for an arbitrarily chosen polymer material. In Fig. 5.6 the reduction in specimen thickness of the polymer is shown along the Y direction in arbitrary units. When the angle between the UV light and the surface is 90 °, there is a maximum UV irradiation associated with the maximum degradation rate. That is the reason why the degradation rates at the peaks and the valleys of the surface are much greater than those at the locations where the angle of inclination is around 45 °. In a more general case, the surface profile could be $B \sin(x)$ where B is an arbitrary coefficient related to the surface roughness, the maximum angle of inclination could be less than or greater than 45 degrees. It can be noticed in Fig. 5.7 that initially the tops and bottoms of the surface exhibit higher degradation rates than

those at the other locations. However, when a sharp bottom is formed at the valley, the degradation rate in this location starts to decline, whereas the degradation rate on the peaks remains the same. As a result, the sinusoidal profile will gradually diminish, and a flat shape will eventually become dominant on the entire surface (Fig. 5.7).

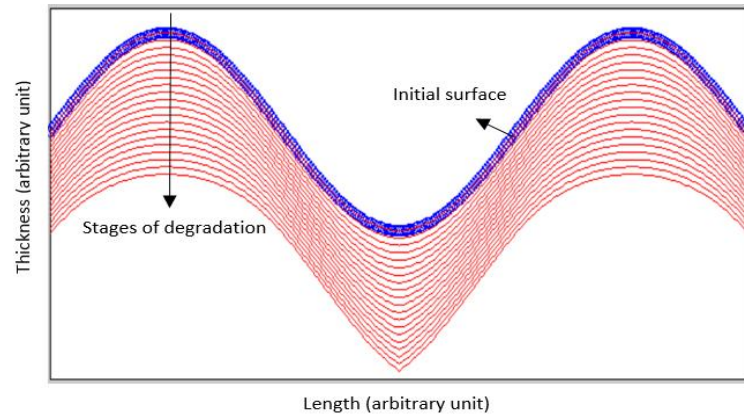


Figure 5.6. Initial stages of UV degradation of a sinusoidal polymeric surface subjected to UV at 90° .

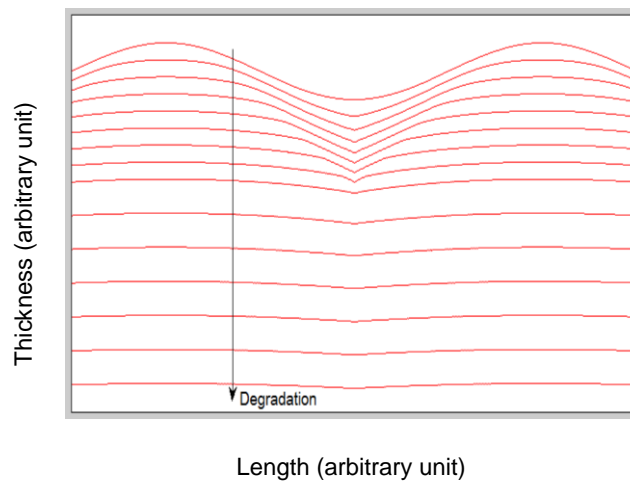


Figure 5.7. Complete UV degradation of a sinusoidal polymeric surface subjected to UV at 90° .

The degradation rates at different locations of the sinusoidal surface are functions of time, as shown in Fig. 5.8. The peak locations are subjected to constant degradation rates because the radiation is directed perpendicularly to the surface at this location and there is no angle change during exposure. At a location where the angle between the surface and UV is 45° , the degradation slowly accelerates as the slope of the surface becomes smaller. At the bottom of the valley the degradation rate is reduced at the beginning, and then increases. There is a maximum, initial degradation rate that is the same as that at the peaks because of the 0° incident angle. However, when the surface profile is approaching a straight line, the degradation rate will slow down and become equal to the rate at 45° . After that, due to the slowed degradation rate at the valleys, the sinusoidal surface will become flat and the degradation rate of the valleys will increasingly approach the rate at the peaks again.

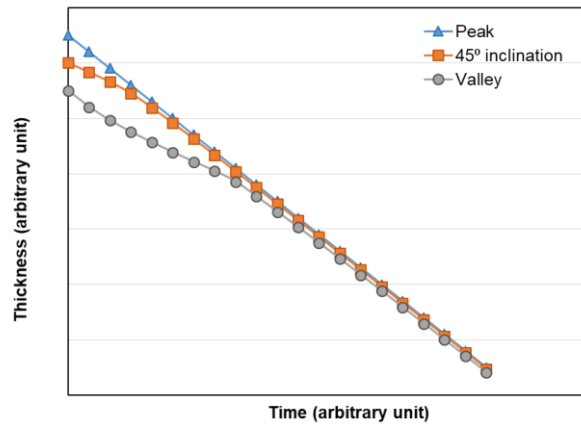


Figure 5.8. Thickness degradation at three different locations of the sinusoidal surface.

One problem which has been encountered in the numerical simulation of UV degradation using MATLAB is that the result could not converge in some situations, as

shown in Fig. 5.9. It was observed that there were very small errors in the initial iteration ($\sim 10^{-16}$). After several iterations, however, the errors accumulated and became more and more significant, eventually leading to a divergent solution. It has been found that it is important to keep the ratio of the number of time steps to the number of nodes above a certain threshold to avoid numerical oscillations in the solution. In this research the critical number was 50.

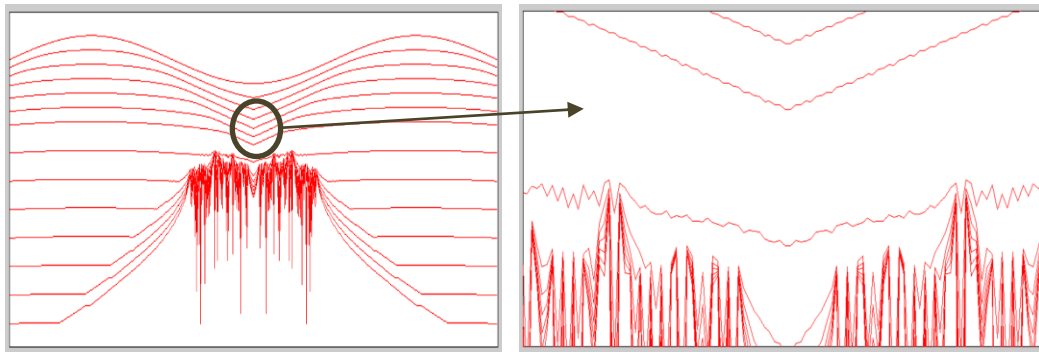


Figure 5.9. Examples of severe oscillations in the solution caused by the numerical instability.

It should be pointed out that the explicit finite difference method has been used to solve equations 5.11-5.14. This method differs from the implicit method where the solution is unconditionally stable. The numerical issues encountered in this work are analogous to those in the transient heat conduction simulation, in which there exists a critical Fourier number (0.5 in the one-dimensional problem, for example) leading to a divergent solution [98]. This implies that there could also exist a critical value in the current problem that determines the numerical stability. It has also been found in this work that it is a good strategy to employ a symmetric surface profile to avoid possible

numerical problems in the UV damage simulation since the numerical errors tend to cancel out in the presence of symmetrical domains.

5.4.3 Surface amplitude and frequency shape effects

The UV degradation simulations of sinusoidal surfaces presented above show that peaks exhibit higher UV aging rates than other locations, which leads eventually to a flat surface. It is reasonable to ask how the initial surface topography of polymers with different surface amplitudes and frequencies will affect UV degradation rates and final surface morphologies. In this section, the numerical UV degradation model was expanded to include various surface amplitudes and frequencies. Amplitudes and frequencies are the most important parameters to characterize surface topography (2D profile). The amplitude parameters are used to measure the vertical characteristics of the surface deviations. The frequency parameters are those which measure the horizontal characteristics of the surface deviations. Therefore, these two parameters were expanded in the simulation to investigate the influence of the distribution of surface heights and the spacing between peaks and valleys on the surface degradation rates.

The studied surface was described by a sinusoidal profile defined by $y = A \cdot \sin(Bx)$, where B and A are the characteristic factors of the profile. These factors were varied to generate six different profiles. A represents the roughness (amplitude) and B is the wavelength (frequency) parameters of the profile. The physical parameters used in the

simulation are listed in Table 5.1. Fig. 5.10 schematically shows six different surfaces with different amplitudes and frequencies analyzed in this study.

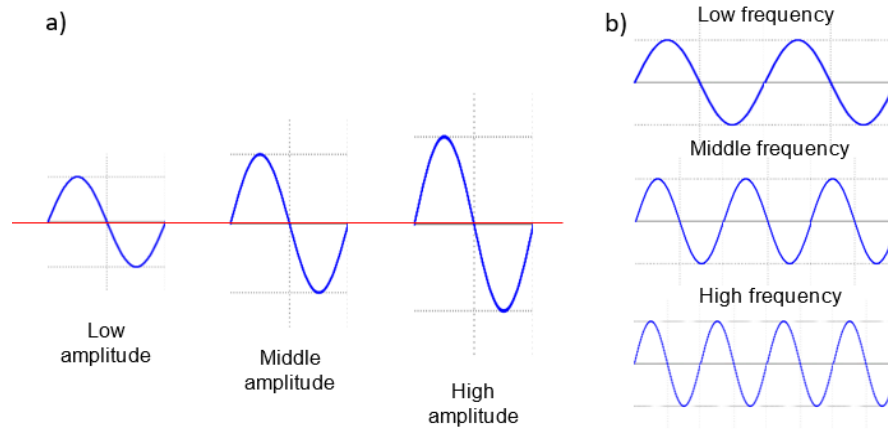


Figure 5.10. Schematics of six surfaces; a) three surfaces with the same frequency but different amplitudes and b) three surfaces with the same amplitude but different frequencies.

Fig. 5.11 and 5.12 present the RMS roughness values of the simulated surfaces as a function of the UV exposure time. It can be seen that the roughness values for these six surfaces decreased to the lowest value of around 0.05 for the maximum simulation time. Again, this simulation result indicated that the UV planarization mechanism is associated with a significant reduction of surface amplitudes. In addition, in the early stages of degradation, the RMS values decrease with similar rates. A reduction of 0.25 units from their initial value (Fig. 5.11) was predicted. After longer UV exposure times, different rates of degradation are evident for the three surfaces, and the surfaces with high amplitudes exhibited faster degradations than the surfaces with the low amplitudes.

It can be seen in Fig. 5.12, initially the high and mid-frequency surface roughness profiles decreased at about the same rate, considerably faster than the low frequency

roughness profile. After longer UV exposure times, different rates of degradation are evident. The RMS values start to decrease and gradually approaches a constant value of about 0.05. The surfaces with the middle and high frequencies exhibit faster transition with larger planarization rates than the surface with the low frequency indicating that the peaks are more affected by UV than the valleys.

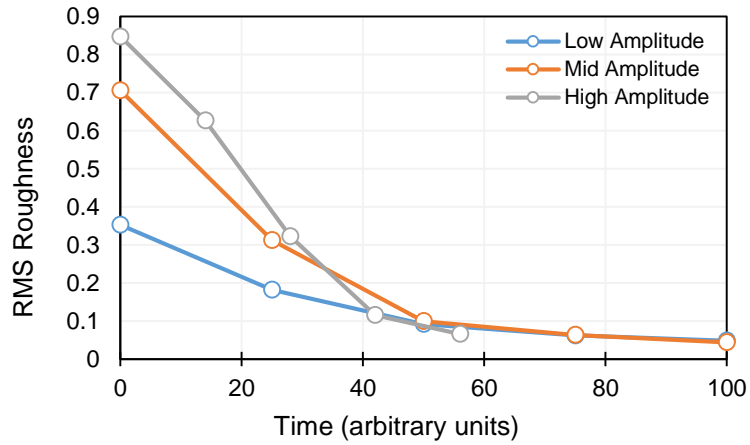


Figure 5.11. Simulated RMS roughness values of three surfaces with different amplitudes as a function of UV radiation time.

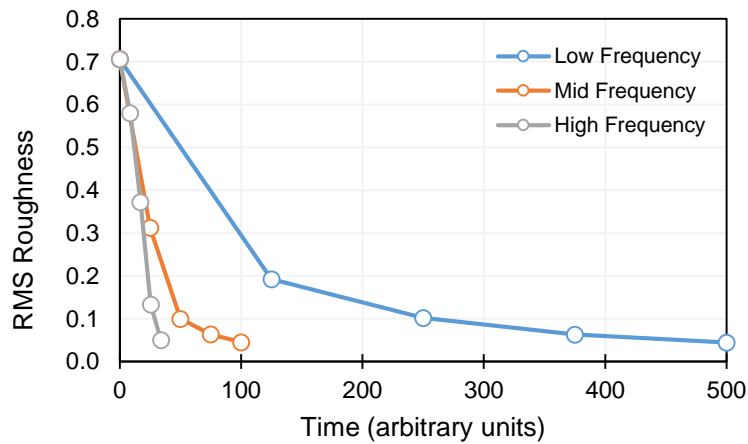


Figure 5.12. Simulated RMS roughness values of three surfaces with different frequencies as a function of UV radiation time.

5.5 Verification of the proposed UV degradation model

In this part of the study, the UV degradation model was experimentally verified by monitoring the local changes in the surface topographies of neat epoxy specimens subjected to UV with the help from Dr. Euripides Solis-Ramos. An unpigmented epoxy resin and a hardener, both supplied by Buehler Inc. (commercial known as EpoxiCure 2 Resin and Epoxicure 2 hardener, the matrix was a mixture consisting of resin with hardener at a ratio of 25% parts by weight), were used to fabricate epoxy specimens according to manufacturer's specifications for UV exposure. A Q-LAB accelerated weathering tester model QUV/spray with an irradiance level of 1.5 W/m^2 at 340 nm wavelength was used in the UV testing. The tests were carried out for 1000 hours at $80 \text{ }^\circ\text{C}$ and the relative humidity was $3 \pm 2\%$ dry. Subsequently, the samples were evaluated for their surface roughness as a function of time both on their unexposed and exposed surfaces. The roughness was determined by the root mean square roughness (R_q), also known as RMS. using equation 5.17. A total of 15 surface profiles were collected using a Keyence white light interference microscope (wide-area 3D measurement system-VR-3100 Series). The results from the tests are listed in Table 5.2. In addition, two examples of the virgin and exposed to UV surfaces are shown in Fig. 5.12. It can be noticed in Table 5.2 that the roughness of the specimens was reduced by 12.5% after 1000 h of UV exposure. Using the t-test approach, it was also determined that the roughness data obtained before and after the UV exposures were statistically different. This thus supports the UV planarization effect observed numerically.

$$R_q = RMS = \sqrt{\frac{1}{n} \sum_{i=1}^n y_i^2} \quad \text{Eq. 5.17}$$

where y_i is surface height.

Table 5.2. Comparison of surface roughness of unexposed and exposed to UV epoxy surfaces after 1000h.

Surface Conditions	R_q (μm)		% change
	Unexposed	UV exposed	
As supplied	1.6 ± 0.2	1.4 ± 0.1	12.5

The UV planarization effect on irregular polymeric surfaces can also be observed in Fig. 5.13, which contains two surface profiles obtained before and after UV exposure for 1000h. It has been observed in this study that the UV planarization mechanism is mainly associated with a significant reduction of surface amplitudes and that the peaks are more affected than the valleys (see Fig. 5.13). This resulted in a reduction in the specimen thickness, $\Delta H = H_i - H_f$, with time, t . The effectiveness of UV degradation parameter, c , can be determined by $-\Delta H/D_{total}$. For the epoxy specimens, the thickness was reduced by $9.4 \pm 1.7 \mu\text{m}$ in 1000 hours and the effectiveness parameter was estimated to be -1.12×10^{-5} .

It should be noted here that the “ c ” parameter obtained by the direct thickness reduction estimations in the epoxy specimens was much smaller than those obtained by the mass change evaluation, and then from the indirect thickness estimation, for the unidirectional glass fiber epoxy composite and the PVC samples described in section 3.

For the neat epoxy specimens, the c value was found to be approximately 10 times smaller than for the other two materials. This can be attributed to a much better resistance of the epoxy to UV degradation, since, contrary to the epoxy composites and PVC samples, the neat epoxy specimens developed multiple but much smaller particles after 1000 h (Fig. 5.13, upper right corner) and its UV surface damage appeared to be in its initial stages. Therefore, the UV degradation of the neat epoxy specimens must have been predominantly associated with the thickness reduction by the evaporation of volatiles and shrinkage and by the initial formation of very small particles. It must also be added at this point that the c estimations from the mass loss of badly damaged samples might not be accurate leading to severe underestimations of degradation rates due to the presence of the particles still left on the surface. The particles left on the surface will also create problems in the direct measurements of surface profiles and specimen thickness estimations using the technique presented in this section. This approach, however, is very accurate for the monitoring of the very initial stages of UV degradation in polymers and polymer matrix composites.

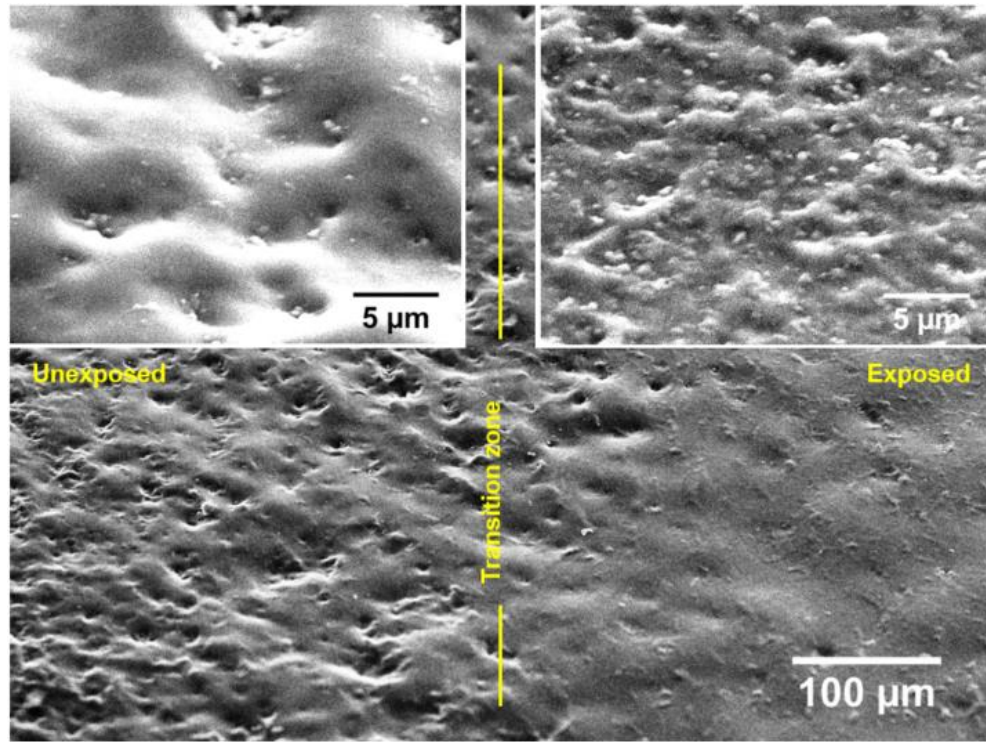


Figure 5.13. Surface topographies of unexposed (left) and UV exposed (right) for 1000h surfaces of the epoxy specimens. Inserts show magnified SEM images of their surface topographies.

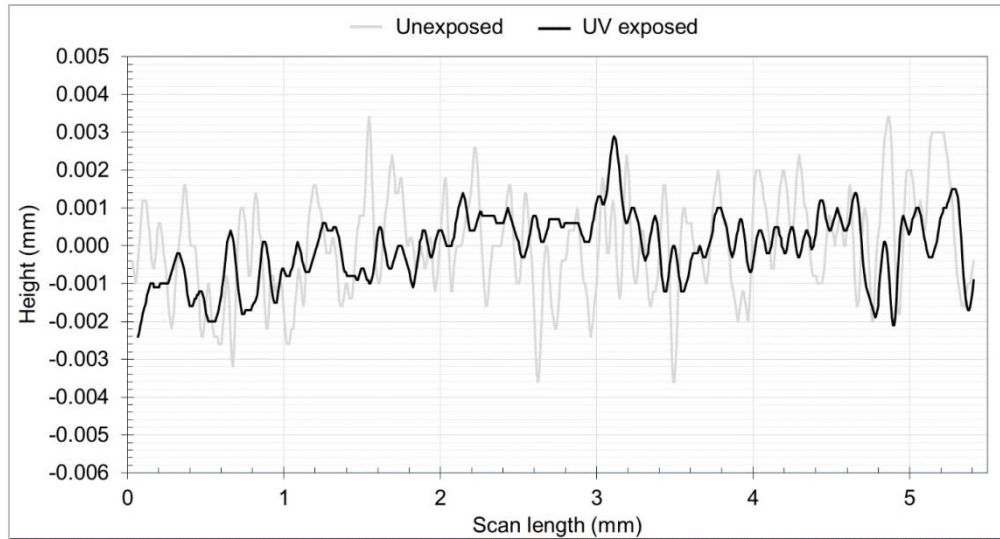


Figure 5.14. Representation of planarization effect after UV exposure.

5.6 Summary

It has been shown in this chapter that UV degradation of polymeric surfaces is strongly dependent on UV wavelength, intensity and exposure time. It is also shown that UV intensity and surface inclinations determine the local degradation rates of the material which can be numerically simulated and compared with the global degradation rates for a material determined experimentally. The finite difference method was successfully applied in the UV radiation simulation to study the evolution of the sinusoidal surface due to the material degradation under UV exposure. The simulation parameters were appropriately defined to avoid numerical instabilities in the solution. Through the numerical simulations, it was concluded that the initial irregular, sinusoidal surface of the material will be eventually degraded to a flat surface over a long period of exposure to UV radiation regardless of the local irradiation angle. Surface shape effects show that polymer surfaces with larger amplitudes and high frequencies suffer faster degradations than the surface with low amplitudes and low frequencies. Furthermore, surface frequency is more influential than surface amplitude in determining degradation rates. Although the simulations were performed in the setting of sinusoidal surfaces, the methodology is equally applicable to any irregular surfaces. The UV planarization effect on irregular polymeric surfaces observed numerically was finally experimentally verified in this work by the UV testing of neat epoxy specimens at elevated temperature. The surface roughness of the specimens was reduced by about 12.5% after 1000 hours of UV exposure.

Chapter 6. Particle Removal Mechanisms in Synergistic Aging of Polymers and GRP Composites under Combined UV and Water Movement

In Chapter 3, a preliminary novel synergistic aging model was proposed to explain complex degradation processes which occur with time on GRP surfaces exposed to combined UV and water condensation. The UV portion of the model was then expanded and presented in Chapter 5. During the aging process micro-particles of a polymer are formed by UV (Chapter 5) and subsequently removed by slowly moving water [14]. The UV radiation model addresses the first stage in this overall degradation process. In this chapter, the hydrodynamic effects of the second stage of the degradation process have been analyzed to explain removals of micro-particles from polymeric materials affected by the synergistic aging by UV and water. Viscous shear stresses generated by slowly moving water were determined on polymer surfaces as a function of surface morphology, flow rates, and volumetric forces. Subsequently, a new micro-particle removal mechanism was suggested by comparing the adhesion forces calculated using the Johnson-Kendall-Roberts (JKR) model and the Hamaker approach with the drag forces created by slow water flows. In the experimental part, the particle removal mechanism has been verified on an inclined unidirectional glass/epoxy surface with randomly distributed epoxy particles subjected to a gravitational flow of water. It has been shown that the movement of polymer particles on polymer/composite surfaces

depends very strongly on particle sizes, water velocity and surface morphology. The research presented in this chapter clearly explains why polymer and GRP degradation by UV in the presence of occasional slow water flows is much faster than just by the individual exposure to UV radiation reported in [13].

6.1 Introduction

Very few studies have concentrated on synergistic aging under multiple degradation conditions [9][15][16][82]. One of them has been recently completed on the environmental degradation of a group of unidirectional glass fiber/polymer composites subjected to combined UV, moisture condensation and elevated temperatures as a function of time [13]. Strong synergistic aging effects were observed for when GRP composites were subjected to UV radiation/water condensation conditions, Table 6.1 [13].

Table 6.1. Total weight changes with standard deviations for six different GRP composites (A-F) tested in [13] individually under UV for 1000h at 80 °C followed by water condensation at 60 °C also for 1000h (Individual Exposures) and under combined 16 hours of UV exposure at 80 °C followed by 8 hours of water condensation at 60 °C for 1000 hours (Cyclic Exposures).

Composites	Sum of Individual Exposures (%)	STD	Cyclic Exposures (%)	STD
A	0.0471	0.0029	-0.1060	0.0314
B	0.0641	0.0131	-0.1030	0.0050
C	0.0038	0.0016	-0.0889	0.0091
D	0.0126	0.0060	-0.0187	0.0040
E	0.0017	0.0028	-0.0760	0.0086
F	0.0734	0.0049	-0.0823	0.0056

According to the damage hypothesis made in [13] and presented in Chapter 3 , the UV/water flow aging model consists of two consecutive stages including: Part (A) UV radiation damage formation on polymer surfaces and Part (B) cleaning UV damage on polymer surface by moving water (Fig. 3.13). In this research, hydrodynamics effects are added to the degradation study in [13] to explain in detail the accelerated aging under the cyclic UV/water condensation situation. In particular, the briefly described particle removal model in [13] is greatly expanded, experimentally verified, and then used to determine the manner micro-polymer particles are moved by slowly moving water on UV damaged polymer and GRP surfaces.

The UV/water synergistic aging model is based on the following main assumptions:

- No water absorption or diffusion occur during condensation exposure.
- Water does not react with the polymer.
- Water flow velocity is low; water is accelerated by the gravity alone.
- The particles are spherical in shape and perfectly smooth.
- The substrate is also perfectly smooth.
- Micro-particles are distributed on the surface as a monolayer and subjected to laminar flows.
- Only adhesion forces between particles and the surface are considered; interactions between particles are neglected.
- Additional less important assumptions will be added to this research.

6.2 Interaction of particles with substrates

It is known that particle adhesion and detachment depend on many factors such as particle and surface material properties, particle shape and morphology, contact area, and surface roughness [100][100][102]. To simplify this potentially complicated problem, all of the particles in [13] and in this work are assumed to be perfectly smooth and spherical. In addition, the effects of gravity and buoyancy are relatively small for micro-scale particles and are neglected [103]. Also, for many microscopic particle systems the electrostatic double layer forces are insignificant compared to the van der Waals forces when the particles and surface are the same material and in contact [104]. Moreover, since the particles are assumed to be constantly immersed in water, capillary forces were also neglected. Therefore, the adhesion forces acting on the particles considered in this research are mainly determined by the Van der Waals forces.

H.C. Hamaker [105] employed the concept of the London-Van der Waals interaction between molecules for the attraction between two spherical macroscopic bodies. If the diameter of one sphere is allowed to approach infinity, the Hamaker equation (Eq. 6.1) [103][106][107] can be used for the case of a sphere adhering to a flat surface.

$$F = \frac{A_H d}{12z_0^2} \quad \text{Eq.6.1}$$

where F is the adhesion force, A_H is the Hamaker constant, d is the particle diameter, and z_0 is the particle-surface separation distance at contact, which is generally assumed to be the equilibrium spacing in the Lennard - Jones potential equal to 0.4 nm [104][108]. It

can be seen, however, that Hamaker's method does not consider the contact area between particles and flat surfaces. To determine the total force including the Van der Waals force and the force acting on the contact area, Eq. 6.2 has been adapted [109][110][111]

$$F = \frac{A_H d}{12z_0^2} \left(1 + \frac{2a^2}{z_0 d} \right) \quad \text{Eq.6.2}$$

where a is the radius of the contact area between the particle and the flat surface. The contact radius depends on the physical properties of the materials involved. These properties determine whether the particle or the surface will deform, which could be calculated using Eqs. 6.3-6.6.

Johnson-Kendall-Roberts (JKR) developed a model that included the effect of adhesion forces on the deformation of an elastic sphere in contact with an elastic half space [112]. Accordingly, the contact radius in the model is given in Eq. 6.3 [111][113][114]:

$$a^3 = \frac{d}{2K} \left[P + \frac{3}{2} W_A \pi d + \sqrt{3\pi W_A d P + \left(\frac{3\pi W_A d}{2} \right)^2} \right] \quad \text{Eq. 6.3}$$

$$W_A = \frac{A_H}{12\pi \cdot z_0^2} \quad \text{Eq. 6.4}$$

$$K = \frac{4}{3} \left[\frac{1-\nu_1^2}{E_1} + \frac{1-\nu_2^2}{E_2} \right]^{-1} \quad \text{Eq. 6.5}$$

where K is the composite Young's modulus, P is the external force, and W_A is the thermodynamic work [111]. K is given by Eq. 6.5 in which ν_1 and ν_2 , E_1 and E_2 are Poisson's ratios and Young's moduli for the particle and the sample surface, respectively

[100][112][113]. In this research, the particles and supporting substrates were assumed to be of the same material; therefore, $\nu_1=\nu_2$ and $E_1=E_2$. The contact radius for a zero external force P in Eq. 6.2 can be easily derived from Eq. 6.3, and the simplified result is given by Eq. 6.6.

$$a = \left(\frac{3\pi W_A d^2}{2K} \right)^{1/3} \quad \text{Eq. 6.6}$$

The Derjaguin-Muller-Toporov (DMT) model [115] is an alternative model for adhesive contact problems which assumes that the contact profile remains the same as in the Hertzian contact but has additional attractive interactions outside the area of contact. According to the DMT model, the contact radius for a zero external force is given in Eq. 6.7 [116].

$$a = \left(\frac{\pi W_A d^2}{2K} \right)^{1/3} \quad \text{Eq. 6.7}$$

The JKR model is appropriate for soft, highly deformable particles such as soft polymers adhesively bonded to soft surfaces. In case of hard, less deformable particles and substrates, the DMT model should be applied [107][116]. David Tabor [117] showed that the JKR and DMT approaches were the extreme cases of a single theory parameterized by the Tabor coefficient (μ) defined in Eqs. 6.8 and 6.9

$$\mu \sim \left[\frac{R(\Delta\gamma)^2}{K^2 \times z_0^3} \right]^{1/3} \quad \text{Eq. 6.8}$$

$$\Delta\gamma = 2\gamma \quad \text{Eq. 6.9 [118]}$$

where R is the radius of the particle, γ is the surface energy of the material, and $\Delta\gamma$ is the work of adhesion. According to Tabor, when the coefficient $\mu \gg 1$, the JKR model

should be adapted. However, when the coefficient $\mu \ll 1$, the DMT model should be used [119].

6.3 Particle removal by hydrodynamics

The characteristic features of photolytic damage is the formation of small micro-size particles on the surface of a glass fiber/polymer composite (Fig. 5.1a). Under combined UV/water flow conditions, these micro-size particles are subsequently removed by the flowing water (Fig. 5.1b) [13]. Here, the drag force (i.e. viscous shear stress) caused by water flow is assumed to play a primary role in the particle removal process. When the viscous shear stress is sufficiently large, UV generated micro-particles will be removed from the surface and expose a fresh undamaged layer to the next UV cycle. According to [110][111], when a stream of fluid passes over a surface with distributed particles, drag forces, lift forces, and external moments of surface stresses are generated. These forces are dependent on the flow conditions, particle conditions and the conditions of the substrate. In this work, surface roughness is neglected to simplify the model.

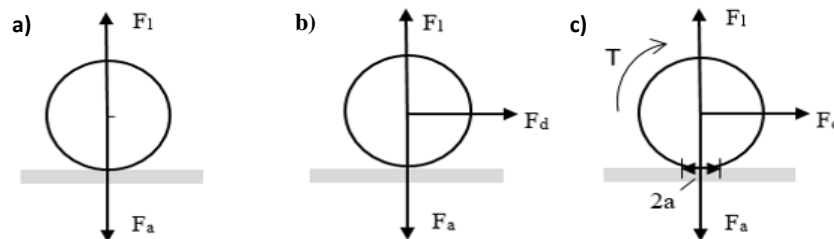


Figure 6.1. Particle removal mechanisms in laminar flow: (a) lifting; (b) sliding; and (c) rolling.

Based on [110], there are three potential particle removal mechanisms by water flow: lifting, sliding, and rolling; as shown in Fig. 6.1. The criteria for particle removal

by the mechanisms are derived from the equilibrium equations; see Eqs. 6.10-6.12. The lifting criterion is derived from the force balance in the vertical direction through Eq. 6.10. The sliding criterion is derived from the force balance in the horizontal direction according to Eq. 6.11. The rolling criterion is derived from the moment balance described by Eq. 6.12.

$$F_l \geq F_a \quad \text{Eq. 6.10}$$

$$F_d \geq u_s(F_a - F_l) \quad \text{Eq. 6.11}$$

$$T + F_l \times a + F_d \times \frac{d}{2} \geq F_a \times a \quad \text{Eq. 6.12}$$

where u_s is the coefficient of wet friction, which was assumed to be 0.01. T is the hydrodynamic moment, F_l is the lifting force, F_d is the drag force, F_a is the adhesion force, a is the contact radius of a particle, and d is the diameter of a particle.

The viscous shear stresses resulting from a pressure difference across the particles are evaluated in this study numerically using COMSOL [120]. The lift forces resulting from a gradient in the shear flow are given in Eq. 6.13 [121].

$$F_l = 81.2(d/2)^3 \frac{1}{\sqrt{\mu v}} \tau^{3/2} \quad \text{Eq. 6.13}$$

where v is the kinematic viscosity, τ is the shear stress and μ is the dynamic viscosity. Dynamic viscosity, also known as absolute viscosity, is a measure of the fluid internal resistance to flow, while the kinematic viscosity is a ratio of the dynamic viscosity to density, $v = \mu / \rho$.

The drag forces can be estimated using the viscous shear stress in Eq. 6.14. [121].

The moment of the surface stresses is given by Eq. 6.15. [110]

$$F_d = 8.014d^2\tau \quad \text{Eq. 6.14}$$

$$T = 0.943993 \cdot 2\pi\mu d^2 V_p \quad \text{Eq. 6.15}$$

where the constant 0.943993 accounts for the effect of the surface on the moment [122][123] and V_p is the fluid velocity at the center of the particle (0.01 m/s).

6.4 Simulation of hydrodynamic effects on flat and wavy surfaces

In our previous UV/water condensation research [13] the samples were positioned perpendicular to the ground and the water flow was driven solely by gravity. Hence, the velocity of the water flow was slow (0.01 m/s) and the thickness of the water layer on a composite surface was assumed to be 0.5 mm. The dynamic viscosity of water at 25 °C, μ , was taken as 8.9×10^{-4} Pa·s and its density, ρ_w , was assumed to equal 1000 kg/m^3 . The volumetric force (gravity), g , was assumed to be 9.8 m/s^2 . The open boundary condition was assumed on the water surface in the numerical simulations using COMSOL.

According to [124] the distribution and the magnitude of viscous shear stress are affected by the surface morphology, flow velocity, and the slope of a surface. Under the same water flow rates and volume forces, the distribution and magnitude of viscous stress will be different when different amplitudes and frequencies of wavy surfaces are assumed. This effect could be important on GRP surfaces with large amounts of surface fibers. For the same frequency in the sine function but different amplitudes, water flow

velocities and viscous shear stresses were obtained in Fig. 6.2 and Fig. 6.3 for 0 mm, 0.02 mm, and 0.2 mm surface amplitudes.

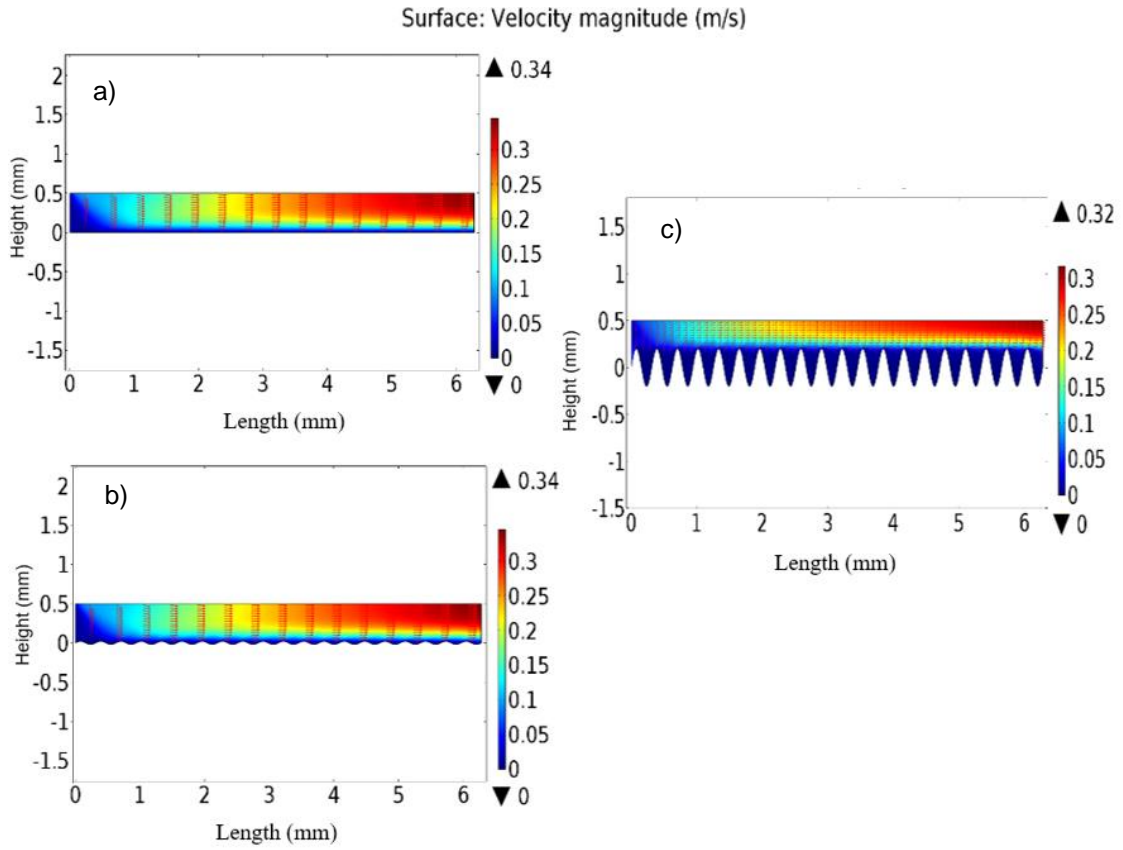


Figure 6.2. The effect of surface morphology on water flow velocities for 0 mm, 0.02mm, and 0.2 mm surface amplitudes all with a frequency of 20 1/s.

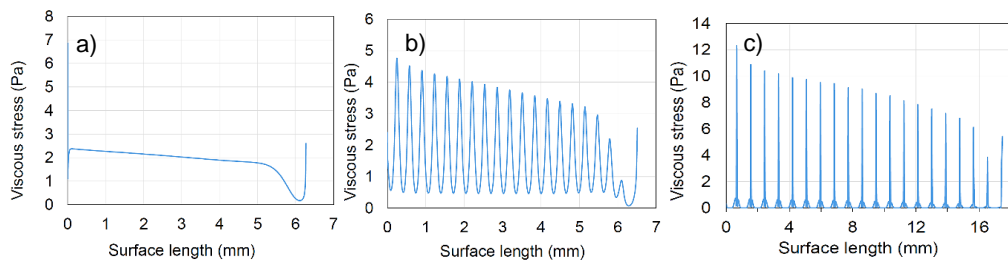


Figure 6.3. Viscous stresses along three surfaces with three different surface profiles: flat (a), sinusoid low amplitude (b) and sinusoidal large amplitude (c).

It can be noticed in Fig. 6.2 that the flow velocity is slightly affected by the amplitudes of sinusoidal surfaces. The maximum flow velocity on the flat surface in Fig. 6.2(a) was found to be 0.34 m/s, which then decreased to 0.32 m/s on the rough surface in Fig. 6.2(c). In addition, the average viscous shear stresses of these three different surfaces (Fig. 6.3) were found to be 1.87 Pa, 1.59 Pa and 0.55 Pa, respectively. It can also be observed in Fig.6.2 that when the amplitude of the wavy surface profile increased from 0 mm to 0.2 mm, the maximum viscous shear stress increased almost three times, the average viscous shear stress decreased three times, and the minimum viscous shear stress decreased from 0.5 Pa to around zero. Therefore, when the surface roughness increases, the average viscous shear stress decreases affecting negatively the efficiency of particle removal.

A steadily decreasing viscous stress on a flat surface and significant oscillations of the viscous stresses on a sinusoidal sample surface can be noticed in Fig. 6.3. The decrease in the shear stress in Fig. 6.3(a) was caused by a decrease in the gradient of the velocity of water flow as it gained distance in water flow direction (du/dy is decreasing in Eq. 6.16). It can be seen in Fig. 6.3(b) that there are periodic oscillations in the viscous stresses on the polymer surface caused by the initial surface configuration affecting streamlines. Streamlines are the curves that are instantaneously tangent to the velocity vector of the flow. In Fig. 6.4(a) the streamlines follow the solid wavy interface in the valley locations. However, in Fig. 6.4(b), the streamline configuration rapidly changed to closed circles inside the valleys, which was caused by an increase in the roughness of the surface. Clearly, under certain circumstances, surface profiles of a sample can rapidly

influence the streamline configuration drastically changing water flow and affecting particle removal.

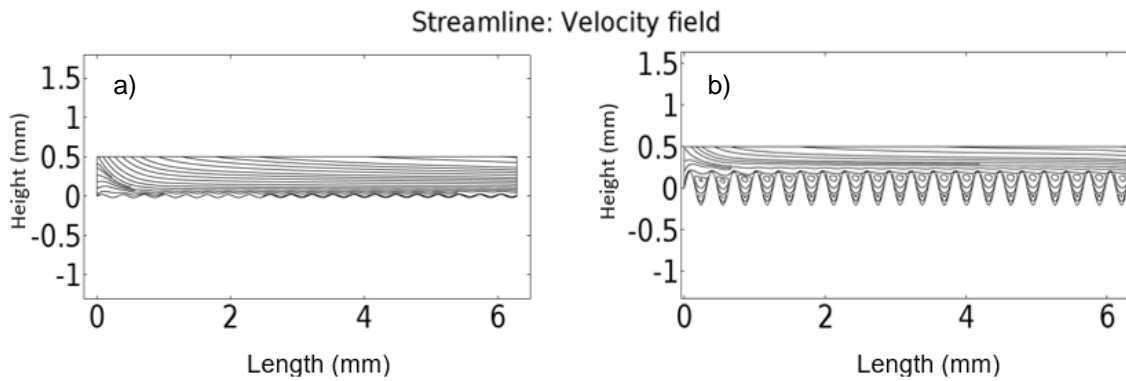


Figure 6.4. Streamlines of water flow for 0.02 and 0.2 mm amplitudes.

According to the viscous stress distribution along the interface in Fig. 6.5, locations can be found with the maximum and minimum viscous stresses, respectively. The bottom of the valley exhibits the maximum viscous shear stresses because of a rapid increase in the shear water velocity (du/dy) (Eq. 6.16) caused by a decrease of the path area due to the elevated surface profile at that location (0.24mm). Similarly, slightly over the peak (0.41mm), the water shear velocity decreases rapidly because an increase in the flow path area leads to a low-pressure condition which eventually forms a minimum shear stress.

$$\tau = \mu \frac{du}{dy} \quad \text{Eq. 6.16}$$

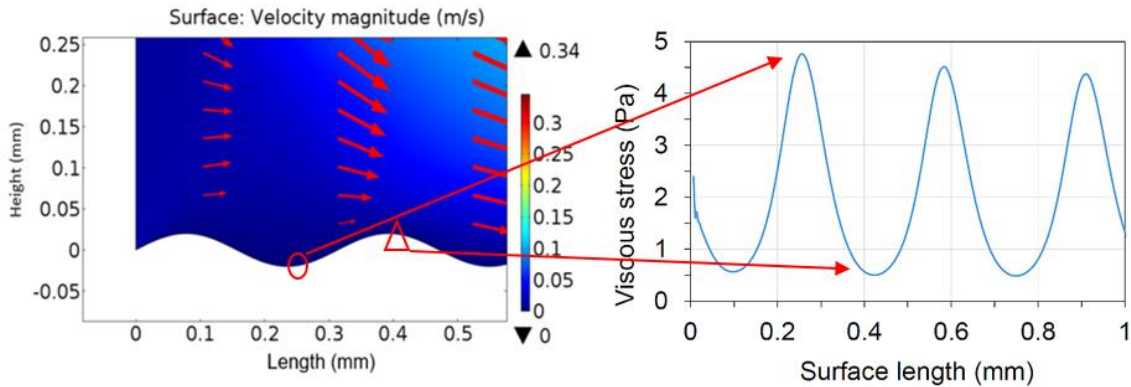


Figure 6.5. Maximum and minimum viscous stress locations for 0.02 mm surface amplitudes.

The effect of the volumetric forces is shown in Fig. 6.6. The volume force equals the gravity when a sample is positioned perpendicular to the ground (90°). However, when the surface is inclined at 45° , the volume force is $0.707g$. Comparing the data in Fig. 6.6 for the 90° and 45° inclined surfaces, the average shear stresses were reduced from 1.59 Pa to 1.29 Pa, almost a 20% decrease, when the volume forces changed from 1.0 g to 0.707 g.

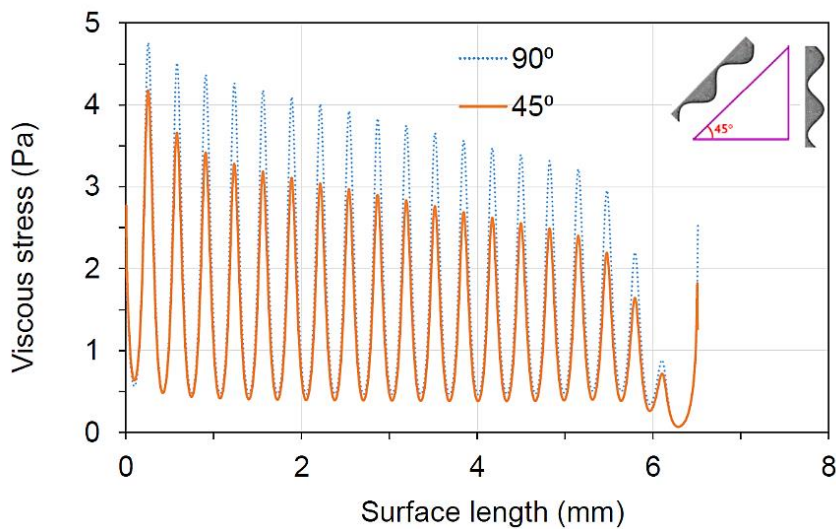


Figure 6.6. The effect of volumetric forces on 45° and 90° inclined surfaces.

Correlations between the surface roughness, body forces and viscous stresses are summarized in Fig. 6.7. Again, when the surface roughness increases, the average viscous shear stress decreases affecting negatively the efficiency of particle removal. Also, when the inclination of the sample surface increases, the average viscous shear stress increases affecting positively the efficiency of particle removal. However, surface roughness (amplitude here) has a more significant effect on particle removal in comparison with surface inclination.

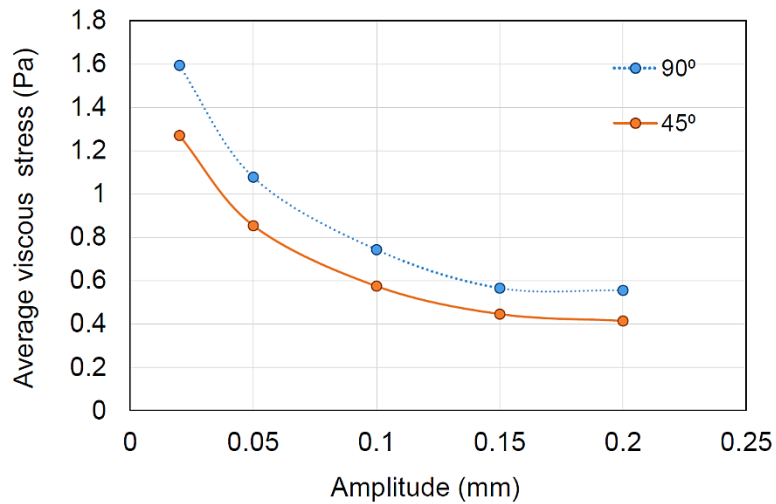


Figure 6.7. The effect of surface profile amplitude and surface inclination on the average viscous shear stresses.

6.5 Particle removal simulations and preliminary verifications

6.5.1 Adhesive forces for small epoxy particles on wet epoxy surfaces

According to Section 3, the adhesion forces between smooth spherical micro-particles and a smooth surface are mainly determined by the van der Waals forces. They can be determined using Eqs. 6.2-6.7 following the DMT and JKR models, and the Hamaker approach. The forces were calculated in this study for epoxy particles assuming

that the density of the epoxy, ρ_e , is $1,400 \text{ kg/m}^3$, the density of water, ρ_w , is $1,000 \text{ kg/m}^3$, the Hamaker constant, A_H , is $1 \times 10^{-20} \text{ J}$ [125]; the gap distance, z_0 , is 0.4 nm , the Young's modulus of the epoxy, E , is 3.0 GPa , and the Poisson's ratio of the epoxy particles, ν , is 0.38 . The surface energy, γ , of the perfectly wet contact area between the particle and the substrate was assumed to be equal to 0.072 J/m^2 [126]. The estimated van der Waals forces for the assumed physical properties are listed in Table 6.2 with the estimated weights and buoyancies of the particles.

It can be seen in Table 6.2 that the gravitational forces and buoyancies of the particles were much smaller than the van der Waals forces for the particles smaller than $200 \text{ }\mu\text{m}$. Therefore, for small micro size particles their weights and buoyancies could be neglected in the calculation of their adhesion forces. For those particles, the van der Waals force is the main factor which prevents the particle detachment in the presence of water. It can also be observed in Table 6.2 that the adhesion forces estimated from Eq. 6.3 by using the contact radii determined from the JKR model are higher than those from the DMT model.

Table 6.2. Adhesion and gravitational forces, and buoyancies for epoxy particles of different sizes determined from the DMT and JKR models.

Particle diameter (μm)	Adhesion force (N) DMT	Adhesion force (N)JKR	Gravitational force (N)	Buoyancy (N)
0.2	5.0859×10^{-9}	9.4540×10^{-9}	4.5976×10^{-16}	3.2840×10^{-16}
2	9.7547×10^{-8}	1.9166×10^{-7}	4.5976×10^{-13}	3.2840×10^{-13}
20	1.9813×10^{-6}	4.0088×10^{-6}	4.5976×10^{-10}	3.2840×10^{-10}
200	4.1484×10^{-5}	8.5165×10^{-5}	4.5976×10^{-7}	3.2840×10^{-7}

For the assumed physical properties of the particles and the contact area, the Tabor coefficients were subsequently calculated using Eq. 6.8. The coefficients were found to be ranging from 1.8 to 17 for the particle sizes ranging from 0.2 to 200 μm . According to [119], the JKR model is applicable when the Tabor coefficient is larger than 5. When the Tabor coefficient is around 1, the Maugis-Dugdale model should be adopted [127]. In this study, the JKR method was adopted to calculate the contact radii, which were then substituted into Eq. 6.2 to calculate the van der Waals adhesion forces [128].

6.5.2 Explanation of particle removal in Fig. 3.13 from [13].

For a shear stress of 1.59 Pa obtained from the hydrodynamic FEM model and determined for a surface amplitude of 0.02 mm and by using equations 6.2-6.15, the movements of the epoxy particles seen in Fig. 5.1(a) were predicted for gravitational water flows. It has been shown that the particles larger than 1.3 μm can roll, and that the combined sliding/rolling type of motion is possible for particles larger than 34.1 μm . It has also been found that particles larger than 84.5 μm will move by a combination of sliding, rolling and lifting. These preliminary predictions can be verified by the SEM observations in Fig. 5.1. Slow water flows, created by moisture condensation on vertically positioned composite samples with the fibers oriented with the water flow as shown in Fig. 5.1(a), removed almost all the 2-50 μm diameter particles in Fig. 5.1(b) that were generated by UV radiation in Fig 5.1(a). However, smaller particles ($<1 \mu\text{m}$) still adhered to the surface. This has already been briefly reported in [13], however,

without any specifics regarding the combined movements of the particles depending on their sizes.

6.5.3 Predictions of particle movements on smooth inclined surface caused by moving water

The above simulations were subsequently extended to other shear stresses created by slowly moving water due to gravitational forces on smooth inclined polymer surfaces for the inclination angles of 30 °, 45 °, 60 °, 75 ° and 90 ° (Fig. 6.8). From the particle removal simulations, it is noticed that small particles can be washed away by lifting, sliding or rolling if removal conditions are satisfied. Thus, it is possible for each viscous shear stress in Fig. 6.8 to remove three different size particles by different combinations of rolling, sliding or lifting mechanisms depending on their diameters. Large size micro-particles will tend to move by the three different movements. On the other hand, smaller particles will tend to mostly roll. Fig. 6.8 shows these relationships between viscous shear stresses caused by gravitational water flows, particle sizes and their movements on inclined smooth surfaces. It should be stated here that in reality, particle collisions can also have a significant effect on their movements. These effects were ignored in this study assuming that each particle is removed independently.

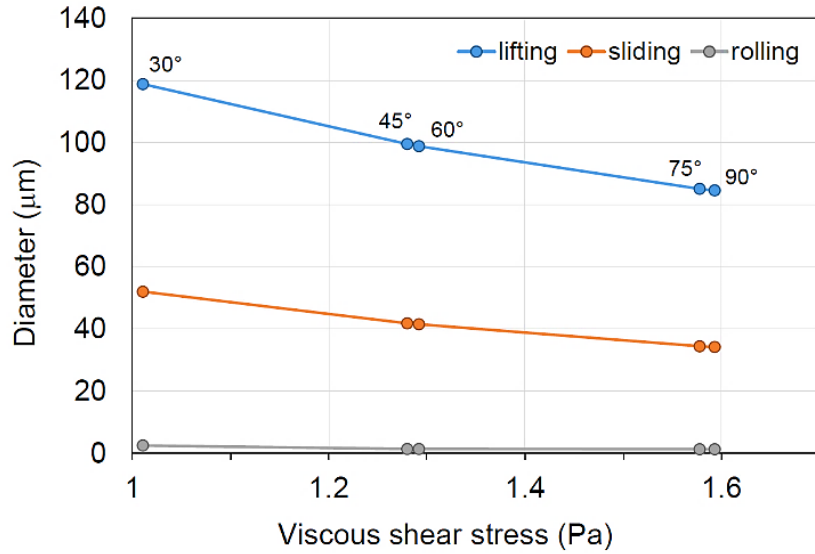


Figure 6.8. Critical size of particle which could be removed by different average shear stresses caused by volumetric forces.

6.6 Experiment verification of particle removal by hydrodynamic effects

To further validate the particle removal model, an alternative particle removal experiment was designed. A polymeric powder made from crushed epoxy was deposited on a flat glass fiber/epoxy substrate and subjected initially to a constant flow of water of 5 ml/min for 10 min at room temperature. The particle removal efficiency in different areas of the substrate was examined. The initial randomly distributed particles had irregular shapes and were 0.1 to 100 μm in size (Fig. 6.9). They were distributed inside a region 20 mm by 50 mm, as shown in Fig. 6.10(a), on an inclined specimen at 30°. After the particle cleaning process was completed, several SEM images were collected from different locations of the substrate to assess the particle interaction with the water flow (Fig. 6.10(b)).

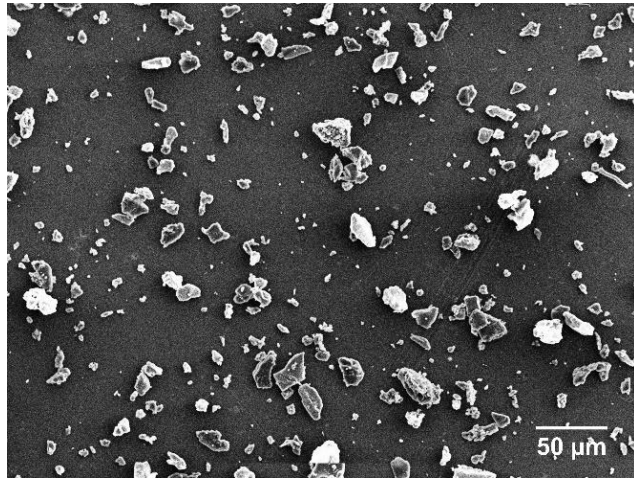


Figure 6.9. Initial particle distribution before water cleaning test.

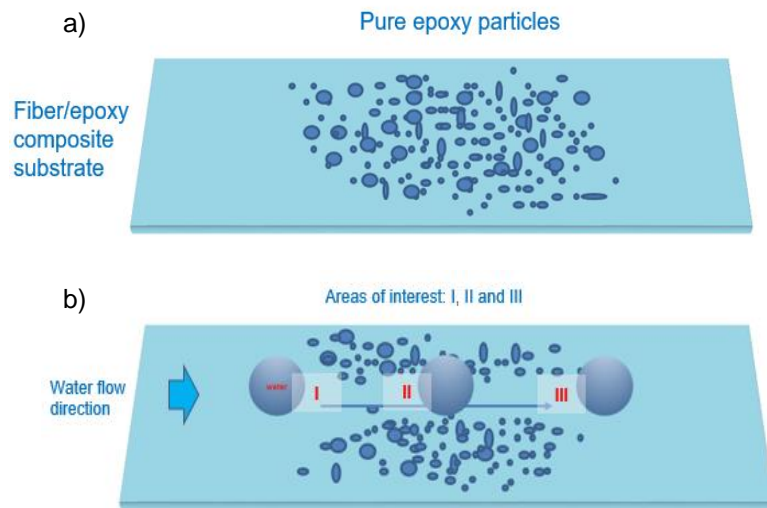
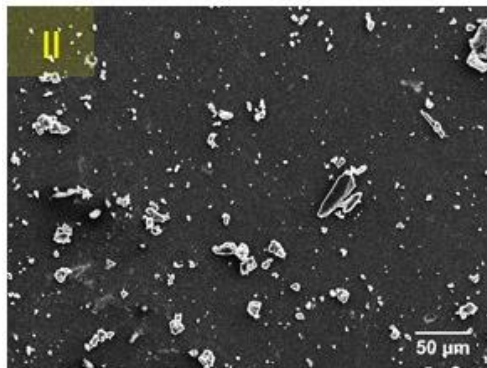
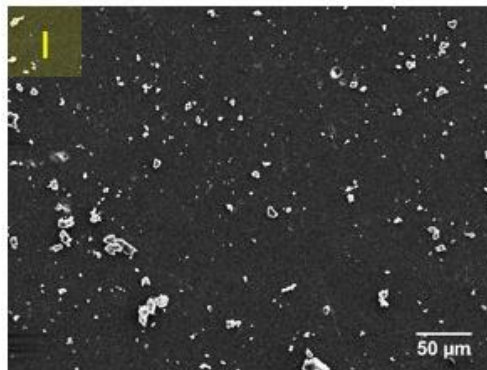


Figure 6.10. Schematics of particle distributions (a) before and (b) after water cleaning experiments.

According to Fig. 6.3(a), viscous shear stresses decrease along flat surfaces in the direction of water flow. This decrease is caused by a gradient of the water flow velocity. Therefore, any variation in the shear stress would be reflected in the particles' interaction with the flowing water. Based on the water experiment, the extent of particle removal can be estimated to verify the hydrodynamic model simulation. First, from the areas of

interest, represented in Fig. 6.10(b), it can be concluded that the viscous shear stress in location I is larger than that in location II, and the viscous stress in location II is greater than that in location III, as water gains distance, i.e. $\tau_I > \tau_{II} > \tau_{III}$. Secondly, the SEM images in Fig. 6.11 show that the particle size distribution was different in the selected locations after the water flow. The measurements conducted in those locations are summarized in Table 6.3.



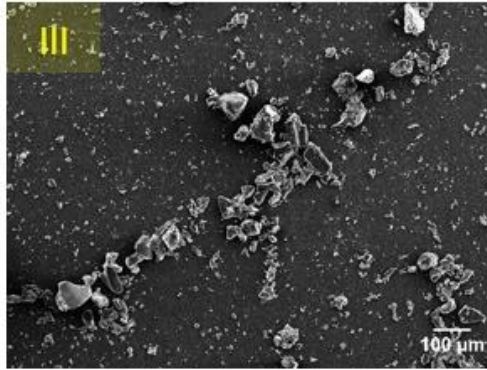


Figure 6.11. SEM images of remaining particles after water flow; (I) mostly small particles, (II) combination of small and large particles, and (III) agglomerates of mostly large particles.

Table 6.3. Particle size distribution analyses; maximum Ferret's diameters.

	Initial (before water)	I	II	III
Particle size (μm)	0.1-45	0.1-20	0.1-47	0.1-119
Average size (μm)	8.9	3.5	4.8	9.4

The small average size of the particles left in region I indicates that most of the large particles were washed away by water, as evident in Fig. 6.11(I). The largest particles were concentrated in region III (Fig. 6.11 (III)). Therefore, it can be concluded that the viscous shear stress in this location was not large enough to cause significant movements of large particles. Once the large particles began to agglomerate, it is possible that this created an obstacle for the subsequent particles to pass through, which eventually led to the agglomerations of the particles seen in region III. Finally, it can also be observed in Table 6.3 that the average particle size significantly increases with increasing water flow direction clearly supporting the hydrodynamic model.

6.7 Summary

In this chapter, hydrodynamics modeling is performed to estimate the viscous shear stresses generated by slowly moving water on polymer and GRP surfaces affected by synergistic aging by UV and water flows. It has been shown that when the surface roughness of the specimens increases, the average viscous shear stress decreases negatively affecting the efficiency of particle removal. On the other hand, when the inclination of the surface increases, the average viscous shear stress increases positively affecting the efficiency of particle removal. A micro-particle removal model is proposed by comparing the adhesion forces calculated by JRK model with the drag forces created by water flows. It has been shown that the movement of polymer particles on polymer surfaces depends strongly on particle sizes, water flow rate, surface morphology, and the viscous shear stresses caused by the moving water. It was also shown in this research that depending on particle sizes and magnitudes of viscous shear stresses, small particles can be moved by rolling only, and large particles could be cleared by a combination of rolling, sliding and lifting. The particle removal model by water was verified experimentally showing the average size of epoxy particles moved by water on a GRP surface increases in the direction of the water flow.

Chapter 7. General Discussion; Effect of Surface Roughness of both Particles and Substrates on Particle Removal; Critical Evaluation of Proposed Particle Removal Mechanism and its Actual Effect on Synergistic Aging of Polymers

In the previous chapter, adhesion forces between smooth spherical micro-particles and smooth polymer surfaces were determined using the JKR model and the Hamaker approach. However, the main limitation of the previous simulations was the fact that the actual polymeric and composite surfaces are not flat and can be highly irregular with complex micro and nano roughness features. In this part of the thesis, the interactions between spherical particles and micro/nano rough surfaces were investigated by applying the Rumpf and Rabinovich models. It has been shown that the adhesion forces predicted by both models are smaller than for flat surfaces and smooth spherical particles determined either by the JKR or Hamaker methods. The Rabinovich model showed that the roughness effect of secondary asperities on adhesion forces is much larger than the effect of primary asperities. A comparison between adhesion forces calculated using the Hamaker method, the Rumpf theory, and the Rabinovich model was also presented. Finally, the limitations of the Rumpf and Rabinovich models are discussed and potential improvements of the models are also suggested in this chapter.

7.1 Introduction

Adhesion is a term relating to the force required to separate two bodies in contact with each other [128][130][130][132]. This phenomenon is well understood following the JKR [112] and DMT [115] models. The JKR and DMT models estimate the adhesion forces between two contacting bodies using a surface energy approximation; however, both models neglect the surface roughness, which causes a non-uniform pressure distribution across the contact area. Regardless of surface preparation, all engineering surfaces exhibit certain finite roughness characteristics. Several earlier studies have shown that the existence of nanoscale and microscale roughness features dramatically reduce adhesion between two contacting bodies due to a decrease in the actual contact area and an increase in the distance between the interacting surfaces [133][134][135] [137].

The classical Rumpf model [135] is the most commonly used model to predict the adhesion forces for nanoscale rough surfaces. This model predicts the adhesion force between particles and surfaces with nanoscale asperities, however, unfortunately little has been said about how well those asperity geometries correlate with surface roughness. Later, by studying the effects of nanoscale surface roughness on adhesion, Rabinovich et al. proposed a relation between the average radius of hemispherical asperities, with the center lying on the rough surface, and the measured rms roughness [137]. According to the Rabinovich model, the adhesion force decreases sharply with increasing surface roughness in the nanometer scale (<2 nm); followed by a gradual and slow decrease with

a further increase in the micro-roughness. Fig. 7.1 schematically illustrates primary and secondary asperities related to this topic.

In this section of the thesis, interactions between adhering particles of various sizes and nano/micro rough surfaces are studied. Aside from adhesive force results, interpretations and comparative studies between the JKR and Hamaker models, the Rumpf model, and the modified Rabinovich model are also presented.

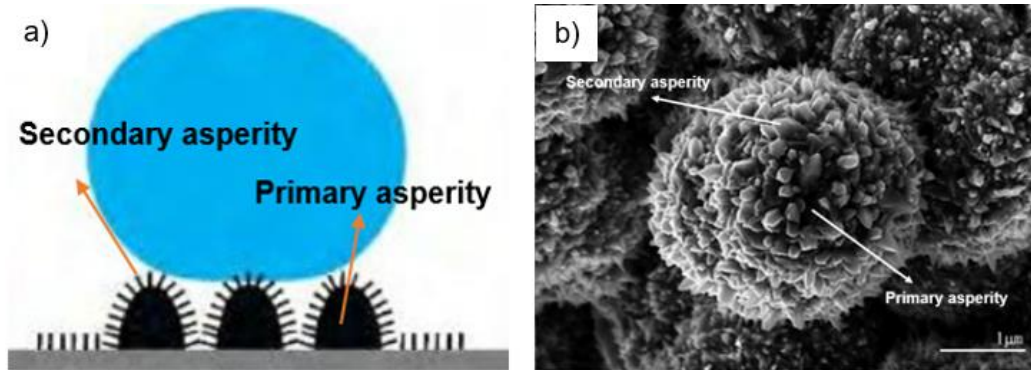


Figure 7.1. a) Schematic illustration of a water droplet on primary asperities and secondary asperities in a micro/nano structure surface and b) a SEM image of a micropapillae with nanobranches [138].

7.2 Adhesion and Van der Waals force

In general, the adhesion force, F_{ad} , is a combination of the electrostatic force, F_{el} , the van der Waals force, F_{vdW} , the capillary force, F_{cap} , and forces due to chemical bonds or acid-base interactions, F_{chem} (Eq.7.1).

$$F_{ad} = F_{el} + F_{vdW} + F_{cap} + F_{chem} \quad \text{Eq.7.1}$$

Under gaseous conditions, contributions from electrostatic forces are significant on insulators and at very low humidity. Under aqueous conditions, electrostatic forces are still important, but their magnitude also depends on electrolyte concentration. The Van

der Waals force always contributes to adhesion, and it is attractive in most cases. Here, we focus on the Van der Waals forces which exist in the most nano level cases.

Van der Waals forces between the materials can be calculated if the geometries are known and the surfaces are smooth. To estimate the influence of roughness on adhesion, several models have been proposed. Rumpf has developed a model in which a small hemisphere is added onto the flat interacting surface [135]. Due to this hemisphere, the distance between the particles increases and the attractive forces decrease. The Rabinovich model simulates the roughness by spherical caps at the substrate [136][137]. These caps can be correlated to the RMS-roughness of the substrate which can be measured, for example, with an atomic force microscope (AFM). The models are able to predict the order of magnitude of the adhesive forces if the roughness is at a nanometer scale. This issue will be discussed in detail in the following section. Fig. 7.2 schematically shows the hemispheres and spherical caps in the Rumpf and Rabinovich models.

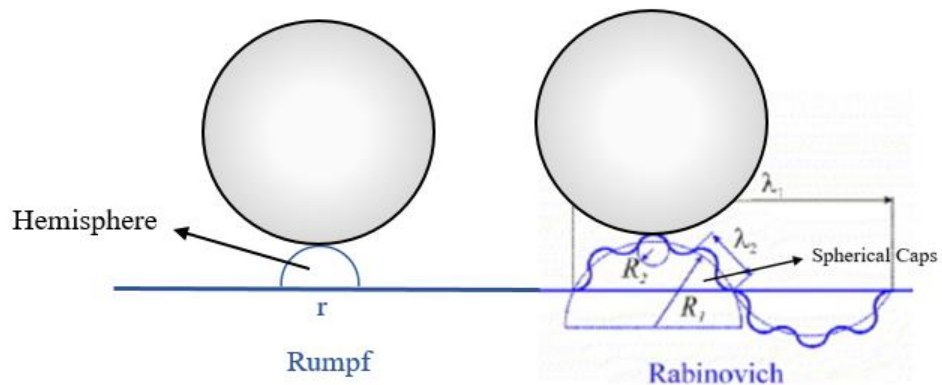


Figure 7.2. Schematics of hemispheres and spherical caps.

To remove adhering dust particles by water, wind or other media, adhesion forces between the dust and substrate surfaces must be first calculated. The Van der Waals forces between solids vary greatly over short separation distances. For smooth surfaces without a micro/nano asperities, the actual contact area between the particles and the surface is relatively large. The debris resist not only for being blown away, but also for adhering to cleaning water droplets. For rough surfaces, surface asperities act as spacers that separate surfaces and serve to reduce the contact area, because the asperity itself is smaller in size than the native surface (i.e., asperity-asperity contact for rough surfaces vs. surface-surface contact for smooth surfaces). Consequently, surface roughness reduces the force needed to separate surfaces in contact by orders of magnitude compared to smooth surfaces. Fig. 7.3 shows the waxy surface of lotus leaves, which combined with the presence of microscopic structures result in an extremely hydrophobic surface that can get rid of adhering particles easily.

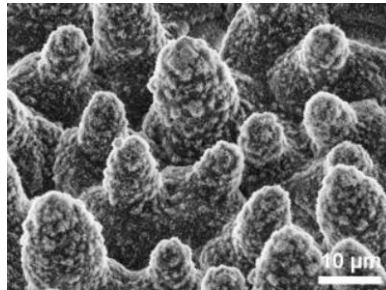


Figure 7.3. Nano/micro roughness structure on the surface of a lotus leaf [139].

From the previous chapter, for smooth surfaces, two types of theories can be used to predict the adhesion force between smooth round particles and smooth flat surfaces: the Hamaker (1937) theory, in which the van der Waals force is a function of the surface

separation distance, and the JKR/DMT (Johnson et al., 1971; Derjaguin et al., 1975) theory in which the surface energy of the compressing surfaces is used to determine the adhesion force. The choice of JKR (Johnson et al., 1971) or DMT (Derjaguin et al., 1975) is determined, in part, by the material properties of the system under investigation, namely, JKR for soft materials and DMT for hard. Not surprisingly, when applied to even mildly rough surfaces, these (smooth-surface) theories are reported to over-predict the measured adhesion force by orders of magnitude. The magnitude of the adhesion forces for the cases illustrated in Fig. 7.4 ranks in the order of (a) < (c) < (b) < (d).

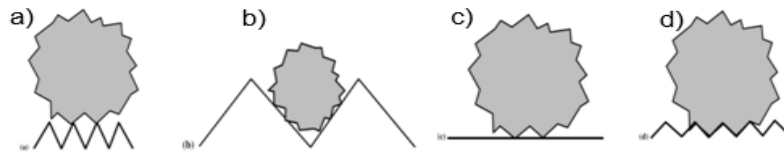


Figure 7.4. Schematics of particle-surface interfacial contacts illustrating the effect of surface roughness on the adhesion of particles to various surfaces, (a) particle size greater than distance between two peaks, (b) particle size smaller than distance between two peaks, (c) particle on flat surface, and (d) particle interlock with rough substrate surface.

7.3 Simulation of adhesion forces between spherical particles and irregular surfaces

7.3.1 Application the Rumpf model

Rumpf's model (Eq. 7.2) is based on a single hemispherical asperity centered on the surface and interacting with a much larger spherical particle along a line normal to the surface connecting their centers, as shown schematically in Fig. 7.5. The model consists of two terms that describe the total van der Waals interaction. The first represents the interaction of the adhering particle in contact with the asperity, while the second

describes the “noncontact” force between the adhering particle and flat surface separated by the height (radius) of the asperity.

$$F_{ad} = \frac{A_H}{6H_0^2} \left[\frac{rR}{r+R} + \frac{R}{\left(1 + \frac{r}{H_0}\right)^2} \right] \quad \text{Eq. 7.2}$$

where A is the Hamaker constant, R and r are the radii of the adhering particle and asperity, respectively, and H_0 is the distance of the closest approach between the surfaces (approximately 0.4 nm).

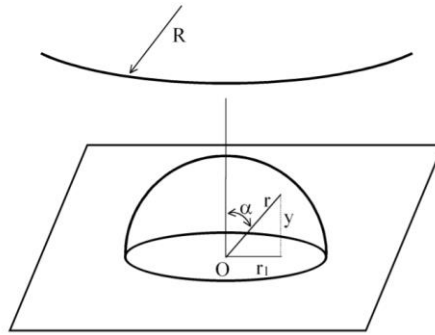


Figure 7.5. Schematic illustration of the geometry proposed by Rumpf for the interaction of an adhering particle with a rough surface. Diagram depicts a hemispherical asperity of radius r and origin at the surface interacting along the y axis with a spherical adhering particle.

In this section, a straightforward simulation of adhesion forces was performed using the Rumpf model. A spherical particle with 20 μm in diameter was considered adhered to a rough surface with different nanoscale asperities. Asperity radii were assumed to be 1nm, 10nm, and 100nm, respectively. The Hamaker constant, A_H was 10^{-20} J, and H_0 was 0.4 nm. The simulation results listed in Table 7.1 show that the adhesion forces determined from the Rumpf model with nano-level asperities on the substrate surface were much smaller than that for a flat epoxy surface from the JKR model.

Table 7.1. Adhesion forces from the Rumpf model for different asperity sizes compared with the predictions using the JKR and Hamaker methods.

r (nm)	1	10	100
F_{ad} (N) Rumpf	9.880×10^{-9}	3.421×10^{-10}	1.840×10^{-9}
F_{ad} (N) JKR	4.009×10^{-6}	4.009×10^{-6}	4.009×10^{-6}
F_{ad} (N) Hamaker	1.852×10^{-7}	1.852×10^{-7}	1.852×10^{-7}

7.3.2 Application the Rabinovich model

The Rumpf theory has been found to under predict the measured force by an order of magnitude [137][139][140][141]. Accordingly, to overcome the large errors generated by the Rumpf model, Rabinovich et al. [136] extended the Rumpf theory by treating asperities as submerged spheres, which removes the hemispherical restriction and allows for a wider range of asperity geometries. He additionally developed the modified Rumpf model to account for the second order asperities of very rough surfaces (Eq. 7.3) [137]. The geometry of this model is shown schematically in Fig. 7.6. In this model, the surface is proposed to consist of an array of spherical asperities and troughs, with the origin of the asperities positioned below the surface. The geometry for these surfaces consists of two scales of roughness (rms_1 and rms_2) and two scales of peak-to-peak distances (λ_1 and λ_2).

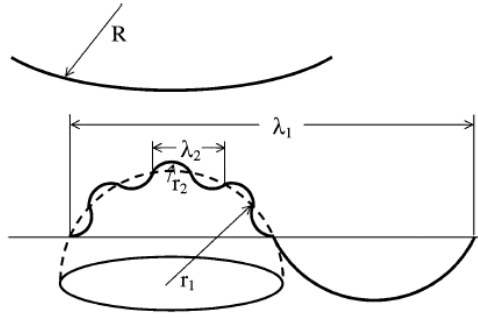


Figure 7.6. Schematic illustration of the geometric model used to calculate adhesion forces using the Rabinovich model.

The adhesion forces based on the Rabinovich theory can now be calculated using the following equation 7.3 [137]:

$$F_{ad} = \frac{A_H R}{6H_0^2} \left[\frac{1}{1 + \frac{58R(rms_2)}{\lambda_2^2}} + \frac{1}{\left(1 + \frac{58R(rms_1)}{\lambda_1^2}\right) \left(1 + \frac{1.82rms_2}{H_0}\right)^2} + \frac{H_0^2}{(1 + 1.82(rms_1 + rms_2))^2} \right] \quad \text{Eq. 7.3}$$

where F_{ad} is the adhesion (pull-off) force and A_H is the Hamaker constant, H_0 is the distance of the closest approach between surfaces, rms_1 and rms_2 are the roughness values of surfaces and peak-to-peak distances, and λ_1 or λ_2 , are associated with both types of superimposed roughnesses. The first, second, and third terms between the brackets correspond to the interaction of the adhered particle with the secondary(nano) asperity, adhesion force between the adhered particle and primary(micro) asperities, and the adhesion forces between adhered particle and the substrate surface, respectively (Fig. 7.7). One limitation of this model is that an adhering particle will interact with only one secondary asperity when the particle comes in contact exactly on the top of the hilly portion of the primary asperity.

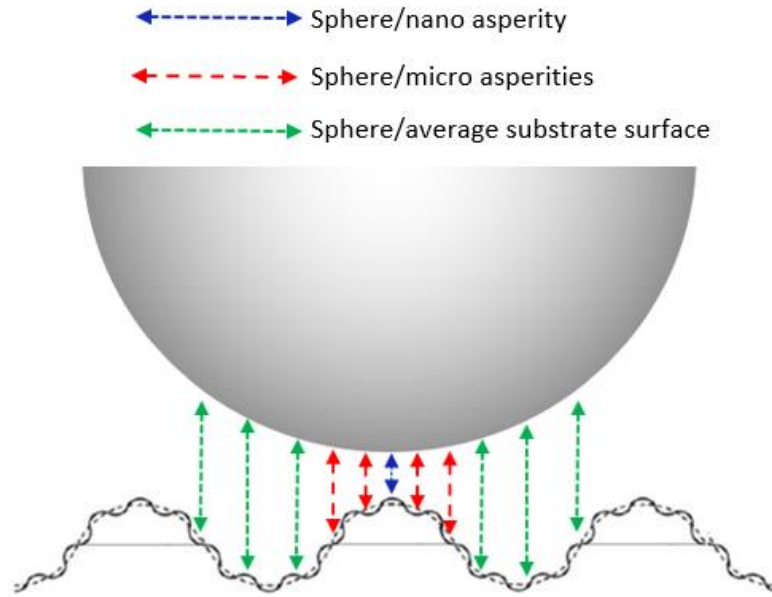


Figure 7.7. Schematics of all interactions between a sphere and a hierarchical structured surface.

When the peak-to-peak distance, λ_1 , is comparable to the particle radius, R , the third term of Eq. 7.3 can be neglected. Therefore, Eq. 7.3 becomes Eq. 7.4.

$$F_{ad} = \frac{A_H R}{6H_0^2} \left[\frac{1}{1 + \frac{58R(rms_2)}{\lambda_2^2}} + \frac{1}{\left(1 + \frac{58R(rms_1)}{\lambda_1^2}\right) \left(1 + \frac{1.82rms_2}{H_0}\right)^2} \right] \quad \text{Eq. 7.4}$$

Again, a simple simulation has been performed by applying the Rabinovich model assuming a spherical epoxy particle with 20 μm in diameter adhering to a rough surface. The parameters used in the simulations are listed in Table 7.2.

Table 7.2. Parameters used in the simulations using the Rabinovich model.

Parameter	Value
Hamaker constant, A_H	10^{-20} J
The smallest distance, H_0	0.4 nm
Particle radius, R	10 μm
Roughness of substrate, rms_1	1.5 μm
Roughness of substrate, rms_2	1-15 nm
Peak-to peak distance, λ_1	20 μm
Peak-to peak distance, λ_2	0.5 μm

Fig. 7.8 presents simulation results of the three terms between the brackets in Eq. 7.3, which represent the interactions between (1) spherical particles and the contact secondary asperity, (2) spherical particles and the non-contact primary asperities, and (3) spherical particles and the non-contact substrate surface, respectively. It can be seen that the particle/nano asperity interaction dominates the total adhesion force. The spherical particle/micro asperities interaction is at least two orders of magnitude smaller than the interaction between the particle and the nano asperities. The spherical particle/flat surface interaction is so small compared to the other two interactions that it can be neglected.

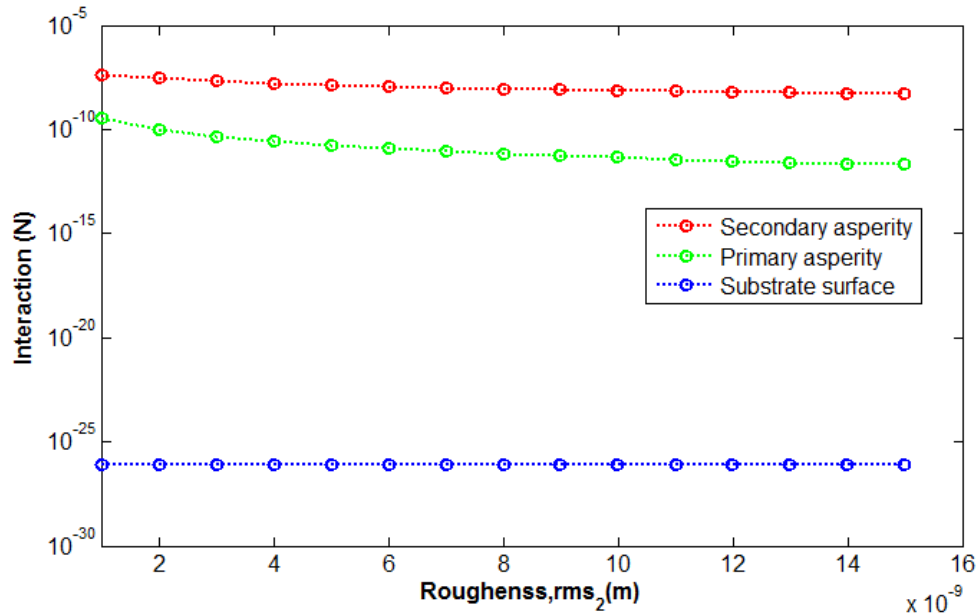


Figure 7.8. Predictions of sphere/secondary asperity, sphere/primary, and sphere/ substrate interactions.

Fig. 7.9 illustrates adhesion forces with different particles sizes using the Rabinovich method. The difference in adhesion forces caused by spherical particle sizes becomes small when the roughness rms₂ of secondary asperities increases from 1 to 15nm. It can be seen from the simulations that when the sizes of adhering particles and the roughness of primary asperities are kept constant, the roughness of secondary asperities will dramatically affect the adhesion force. When the roughness of secondary asperities is around 1 nm, all three particle sizes have maximum adhesion forces. Then the adhesion force decreases sharply with increasing surface roughness in the nanometer range (< 2 nm); followed by a gradual and slow decrease with further increases in roughness. Eventually, the adhesion forces decrease to a minimum value. Figure 7.10 shows a schematic diagram of the Rabinovich simulation for particle-rough surface interaction.

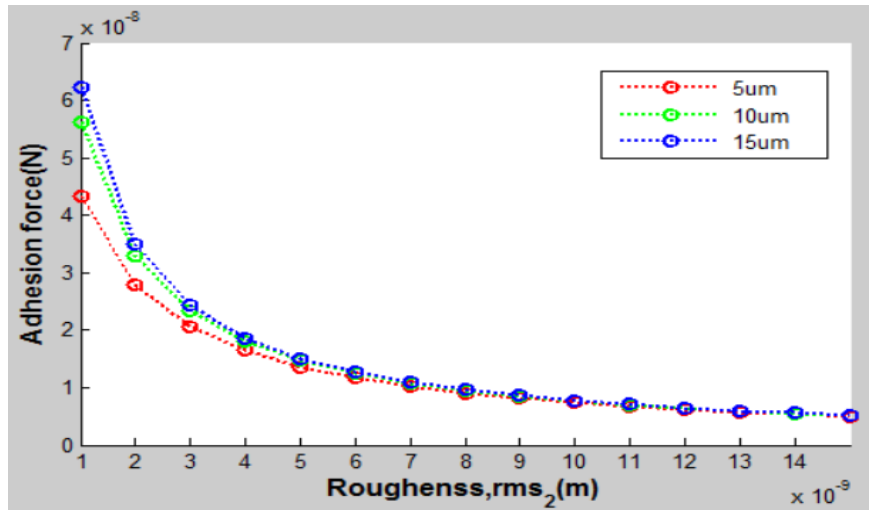


Figure 7.9. Adhesion forces for different particle sizes calculated using the Rabinovich model.

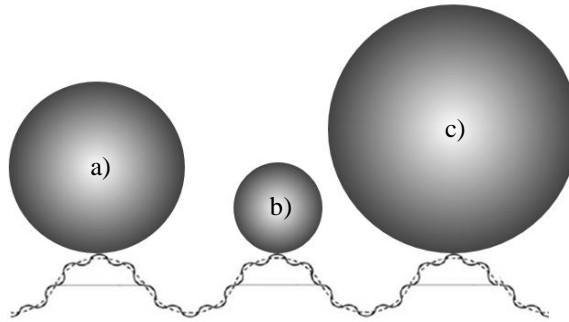


Figure 7.10. Schematic diagram of particle-rough surface interaction with particle radii (a) 10 μm , (b) 5 μm and (c) 15 μm .

The roughness effect of primary asperities was also investigated and the results are presented in Fig.7.11 comparing the effect of both micro and nano asperities on particle adhesion for rms_1 ranging from 0.1 to 100 μm and rms_2 ranging from 1 to 20nm. When the primary roughness rms_1 increases from 0.1 to 100 μm and the secondary roughness is 1 nm, adhesion forces decrease from 3.915×10^{-9} to 3.907×10^{-9} N. However, when the secondary roughness changes from 1 to 20nm and the primary roughness is 0.1 μm , adhesion forces decrease from 5.579×10^{-8} to 3.907×10^{-9} N. Therefore, it can be

clearly concluded from Fig. 7.11 that the roughness effect of primary asperities on adhesion force is much smaller than the roughness effect of secondary asperities.

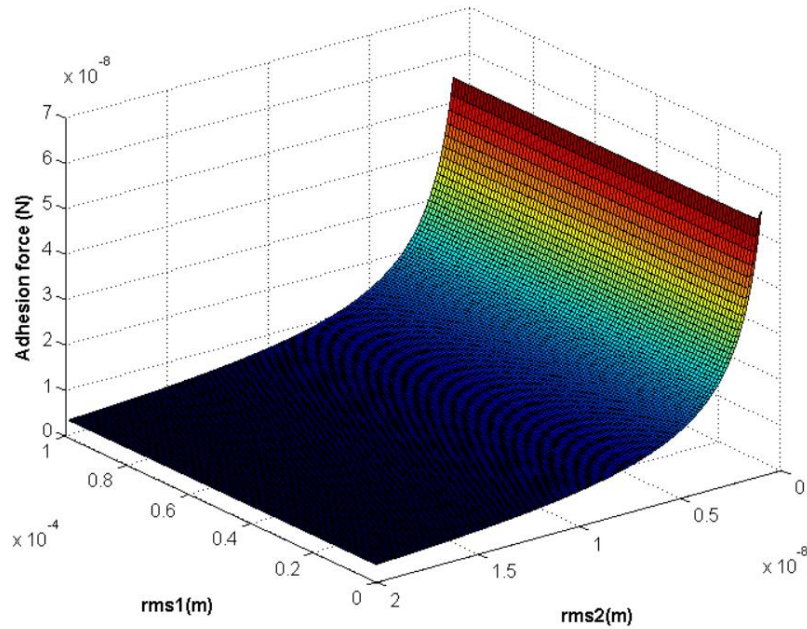


Figure 7.11. Predictions of adhesion forces for an epoxy sphere with irregular surfaces as a function of rms1 and rms2. R is 10 μm .

It has been shown in Fig. 7.11 that the nanoscale roughness rms₂ is more important than the primary roughness rms₁ in creating adhesion forces when spherical particles are kept of the same size. Fig. 7.12 shows the relationship of the adhesion force, particle radius, and roughness of nanoscale asperities. Again, it can be seen in Fig. 7.12(a) that increasing the surface roughness caused by secondary asperities dramatically decreases the adhesion forces. In addition, when particle radii increase from 0.1 to 200 μm and asperities roughness is 1 nm, adhesion forces increase from 1.527×10^{-8} to

7.874×10^{-8} N. It is noticed in Fig. 7.12(b) that adhesion forces increase slowly after spherical particles become larger than 5 μm in radius.

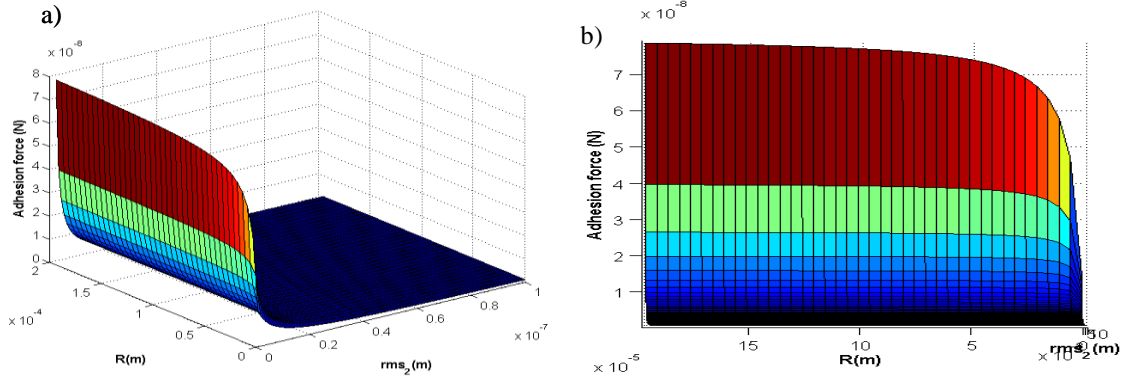


Figure 7.12. (a) Predictions of adhesion forces for an epoxy sphere with the irregular surfaces as a function of R and rms_2 and (b) cross-section view of (a) at $rms_2 = 1 \text{ nm}$.

7.4 Comparison of the Rumpf, Rabinovich, and Hamaker models

As presented in Chapter 5, a simple flat surface was used as the substrate to calculate the adhesion between epoxy particles and an epoxy surface. However, in actual situations irregularities exist on the surfaces of the particles and their substrates. To predict the correct Van der Waals forces considering the presence of surface irregularities for the substrates, the modified Rumpf and Rabinovich approaches were adopted in this research. The modified Rumpf model assumes that roughness rms treats peaks and valleys equivalently, as seen in Eq. 7.5. RMS values can be measured with an AFM. In the following simulations, it is assumed that rms is equal to rms_2

$$F_{ad} = \frac{A_H R}{6H_0^2} \left[\frac{1}{1+(R/1.48rms)} + \frac{1}{(1+1.48rms/H_0)^2} \right] \quad \text{Eq. 7.5}$$

The parameters used in the calculations of the Rumpf, Rabinovich and Hamaker method are listed in the Table 7.3.

Table 7.3. Values used in calculations.

Parameter	Rumpf	Rabinovich	Hamaker
Hamaker constant, A_H	10^{-20} J	10^{-20} J	10^{-20} J
The smallest distance, H_0	0.4nm	0.4nm	0.4nm
Particle radius, R	10 μm	10 μm	10 μm
Roughness of substrate, rms_1	0	1.5 μm	0
Roughness of substrate, rms_2	1 - 80 nm	1 - 80 nm	0
Peak-to peak distance, λ_1		20 μm	
Peak-to peak distance, λ_2		0.5 μm	

Fig. 7.13 compares the adhesion forces following the above three theories as a function of the secondary asperities (small-scale) roughness rms_2 . For the Rabinovich theory, the other roughness parameters (rms_1 , λ_1 , and λ_2) are held constant. The predicted forces in Fig. 7.13 are constant according to the Hamaker theory with increasing rms , non-monotonic according to the Rumpf theory, and monotonically decreasing according to the Rabinovich theory. The Hamaker theory predicts a constant force because it does not account for the surface roughness. The Rumpf theory predicts a minimum ($\text{rms} \sim 8$ nm), to the left of which the particle/surface interaction dominates and to the right of which the particle/asperity interaction dominates. The Rabinovich model predicts monotonically decreasing forces as both the contacting and non-contacting contributions (first term and second term in Eq. 7.4) reduce with increasing rms . When the roughness of secondary asperities becomes zero, for the Rumpf model, the substrate surface becomes flat leading to the adhesion force being equal to that calculated by the Hamaker

method. Under this condition, both models do not consider the non-contact forces. However, for the Rabinovich model, non-contact forces are still considered even when rms_2 decreases to zero. That is the reason why the adhesion force according to the Rabinovich approach is slightly larger in comparison with the other two methods when rms_2 is zero, as shown in Fig. 7.13.

The predictions from the Rumpf and Rabinovich models (applied to smoother surfaces) collapse at small rms. However, for moderate rms ($\sim 0.5\text{--}40\text{ nm}$) the adhesion force for the Rumpf model is at least an order of magnitude below that of the Rabinovich model. Conversely, at large rms the Rumpf theory predicts a larger asperity radius, resulting in a larger adhesion force. In addition to illustrating how the force prediction is affected by changes in roughness parameters, Fig. 7.13 also demonstrates the order-of-magnitude difference in force predictions between the models for a given set of roughness parameters.

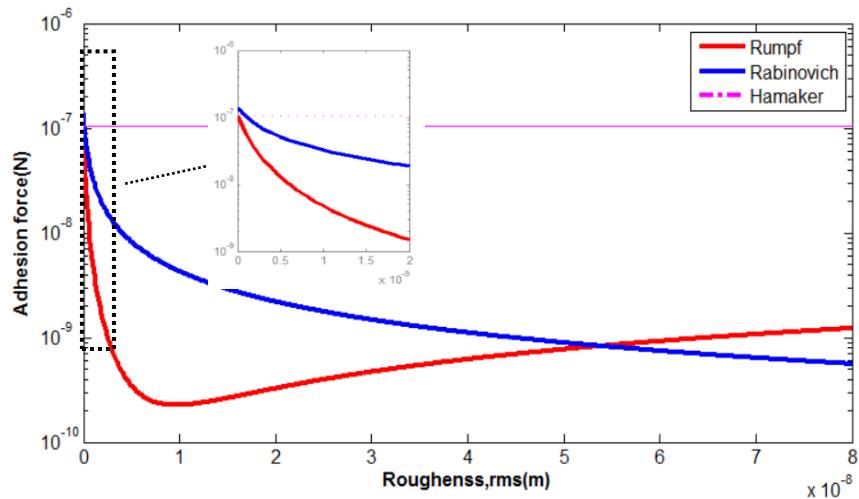


Figure 7.13. Comparison between the Rumpf, Rabinovich and Hamaker models for adhesion forces between an epoxy substrate and a $10\ \mu\text{m}$ epoxy sphere separated by $H_0=0.4\text{ nm}$.

7.5 Limitations of the Rumpf, Rabinovich, and Hamaker models and their potential improvements

It is usually recognized that the geometries of hierarchical asperities of surfaces do not resemble as the Rumpf model described. The asperity geometry is found to be similar to the Rabinovich model. However, the Rabinovich model is based on an approach by calculating interactions between an adhering particle and hemispherical caps. This approach underestimates the role of the valley of asperities and completely neglects the contact interaction between the adhering particle and the valley portion of the asperities, as shown in Fig. 7.14(b). Another problem is that both the Rumpf and Rabinovich models do not consider elastic deformation of surface asperities caused by surface/particle interactions, which is considered in the JKR and DMT models.

One method of solving multi-asperity problems is by applying a Gaussian distribution to assume the height of the surface asperities. Polina et al. [142] presented a new approach to calculate multi-asperities contact interaction between two surfaces. Each asperity is individually considered with its different height and radius of curvature, then the contribution of each asperity to the overall surface was summed. The set of asperities was generated using the Monte Carlo Method and both asperity heights and radii were based on their statistical distributions experimentally obtained. Finally, contact forces were determined for each asperity at a given distance between the two surfaces, and the deformation of each asperity was calculated according to the JKR or DMT model (depending on the material).

Aditya Kumar et al. [144] proposed a model with multi-asperities in contact by modifying the Rabinovich model. When an adhering particle interacts with only one secondary asperity, then the Rabinovich model is valid (Fig. 7.14(a)). However, if the adhering particle comes in contact with the valley portion of primary asperities, then the adhering particle interacts with multiple secondary asperities, as shown in Fig. 7.14(c). The Rabinovich model will underestimate the adhesion force.

It was already stated that the first and second terms in Eq. 7.3 correspond to the adhesion of a particle with secondary and primary asperities, respectively. According to the Kumar model [144], when the number of secondary asperities in contact with adhering particle is n , then adhesion force will be the first term multiplied by n . Eq. 7.6 will replace with Eq. 7.3. In the denominator of the second term, the negative sign comes from the interaction of the adhering particle with the valley portion of primary asperities. It is extremely difficult to calculate the number of contact points. However, the number of secondary asperities in contact lies in between 1 and $\pi R / \lambda_1$ with $\lambda_1 > \sqrt{58Rr_{ms_1}}$. It can be observed from the proposed relationship and our simulation results shown in Fig. 7.15, that the adhesion force is completely dependent on the number of secondary asperities in contact.

$$F_{ad} = \frac{A_H R}{6H_0^2} \left[n \cdot \frac{1}{1 + \frac{58R(r_{ms_2})}{\lambda_2^2}} + \frac{1}{\left(1 - \frac{58R(r_{ms_1})}{\lambda_1^2}\right) \left(1 + \frac{1.82r_{ms_2}}{H_0}\right)^2} + \frac{H_0^2}{(1 + 1.82(r_{ms_1} + r_{ms_2}))^2} \right] \quad \text{Eq. 7.6}$$

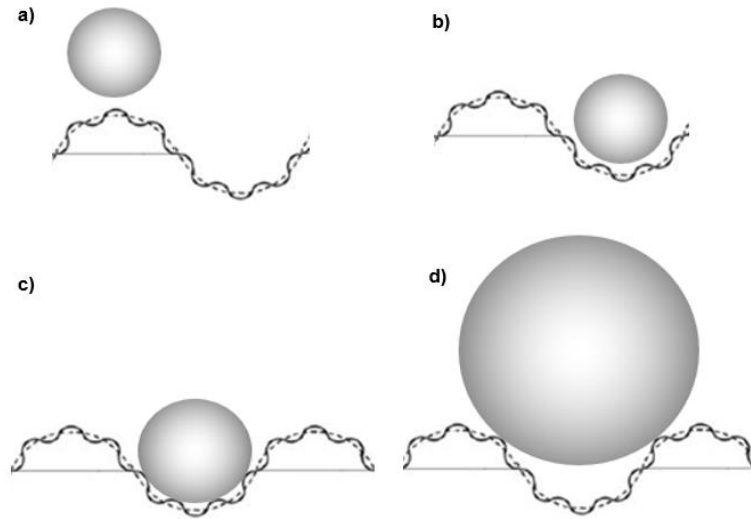


Figure 7.14. (a) Schematic diagram of particle-rough surface interaction ($r_{ms1} > R$). Particle interaction between hilly portion; (b) Schematic diagram of particle-rough surface interaction ($r_{ms1} > R$). Particle interaction between valley portion; (c) Schematic diagram of particle and valley portion of primary asperity showing multiple interactions of adhering particle and secondary asperities. Here r is comparable to R ; (d) Schematic diagram of particle-rough surface interaction ($r_{ms1} < R$). [144]

Table 7.4 shows the parameters used in the following simulation following the Kumar model. It was assumed that a $50 \mu\text{m}$ particle has three asperities in contact, a particle with $5 \mu\text{m}$ in radius has two asperities in contact, and two particles with 50 nm in radius have one and four asperities in contacts, respectively, corresponding to contact at the top of a hilly portion and a valley portion of a primary asperity.

Table 7.4. Parameters used in simulations using the modified Rabinovich model.

Parameter	Value
Hamaker constant, A_H	10^{-20} J
The smallest distance, H_0	0.4 nm
Particle radius, R	50 nm, 5 μm , 50 μm
Roughness of substrate, rms_1	5 μm
Roughness of substrate, rms_2	1 - 15 nm
Peak-to peak distance, λ_1	10 μm
Peak-to peak distance, λ_2	0.1 μm

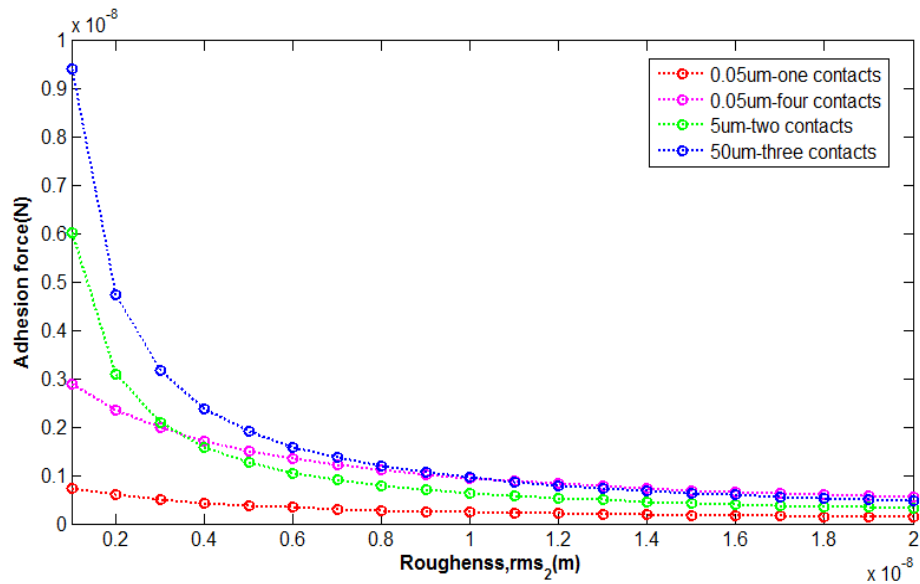


Figure 7.15. Adhesion forces for different particles sizes calculated with the modified Rabinovich model with different numbers of contacts.

As an example, particles with 0.05 μm in radius may be adhered to the surface peaks with only one contact point or to the surface valleys with four contact points

(Fig.7.14a and 7.14c). Particles with 50 μm and 5 μm in radius may adhere to the location between surface peaks with three contacts (in three dimensions) and two contacts(Fig. 7.14d). respectively. From Fig. 7.15, it can be seen that particles of the same size with the higher number of asperity contacts have larger adhesion forces. Comparing the particle with 0.05 μm radius and four interfacial contacts with the particle with 50 μm radius and three interfacial contacts, it was found that the number of contacts is dominant in determining the adhesion force with a large surface rms. When the surface becomes smooth, particle size is also important when determining the adhesion force.

7.6 Adhesion forces between irregular particles and irregular surfaces

When adhered particles are not smooth spheres but irregular in shape, then this problem becomes very complicated. However, it has been shown in Fig. 7.8 that the contact interactions are much larger than the other non-contact interactions. Therefore, the total adhesion force can be calculated by considering the number of adherent contacts between irregular particles and rough surface. A brief description of interactions between irregular particles and irregular surfaces was schematically shown in Fig 7.4. Aside from the interlocking case shown in Fig. 7.4(d), which has a large contact area between particles and surface, the other cases have multi-contacts. According to the previous investigation of multi-contacts between spherical particles and rough surfaces, it has been shown that adhesion forces with multi-contacts are larger than those with only one contact.

Fig. 7.16 schematically shows most common examples of particle and surface interfacial contacts when the particle size is larger than the distance between two microscale peaks, smaller than the distance between two microscale peaks, and similar to the space between microscale peaks. Regardless of the particle sizes, a sphere adhered to a flat surface has the minimum contact point which is equal to one. Most irregular particles that can be stably deposited on a flat or uneven rough surface usually have three contacts for equilibrium. Some small particles that are deposited in the valley portion between two peaks may exhibit more asperities in contact (Fig. 7.16b). However, most of the large particles that are deposited on the top of a hierarchical surface can have only three contacts (Fig. 7.16a). When the particle size is similar to the distance between two peaks, two adherent contacts are possible (Fig. 7.16c).



Figure 7.16. Schematics of a particle-surface interfacial contact, (a) particle size greater than the distance between two peaks, (b) particle size smaller than the distance between two peaks, (c) particle size similar to the distance between two peaks.

Casey Q. LaMarche et al. [145] proposed a model to predict the adhesion forces between rough particles and rough surfaces. They modified the Rabinovich model by introducing micro and nano asperities to a smooth particle, as shown in Fig 7.17.

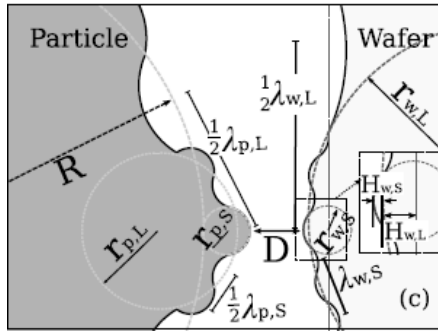


Figure 7.17. Schematics of a rough particle (submerged-sphere roughness) and a rough substrate (submerged-sphere roughness) [145].

The Rabinovich model was modified to give Eq. 7.7 using the Derjaguin approximation to account for the more relevant interaction between a rough particle and a rough substrate.

$$\begin{aligned}
 F_{vdW} = \frac{A}{6} & \left[\frac{R}{(D + H_{p,L} + H_{p,S} + H_{w,S} + H_{w,L})^2} \right. \\
 & + \frac{Rr_{w,L}}{(R + r_{w,L})(D + H_{p,L} + H_{p,S} + H_{w,S})^2} \\
 & + \frac{Rr_{w,S}}{(R + r_{w,S})(D + H_{p,L} + H_{p,S})^2} + \frac{r_{p,L}}{(D + H_{p,S} + H_{w,S} + H_{w,L})^2} \\
 & + \frac{r_{p,L}r_{w,L}}{(r_{p,L} + r_{w,L})(D + H_{p,S} + H_{w,S})^2} \\
 & + \frac{r_{p,L}r_{w,S}}{(r_{p,L} + r_{w,S})(D + H_{p,S})^2} + \frac{r_{p,S}}{(D + H_{w,S} + H_{w,L})^2} \\
 & \left. + \frac{r_{p,S}r_{w,L}}{(r_{p,S} + r_{w,L})(D + H_{w,S})^2} + \frac{r_{p,S}r_{w,S}}{(r_{p,S} + r_{w,S})D^2} \right]
 \end{aligned}
 \tag{Eq. 7.7}$$

where the substrate roughness is defined with nano- and micro-scale asperity radii $r_{w,S}$ and $r_{w,L}$, and heights $H_{w,S}$ and $H_{w,L}$, respectively. Particle roughness is defined with nano- and micro-scale asperity radii $r_{p,S}$ and $r_{p,L}$, and heights $H_{p,S}$ and $H_{p,L}$, respectively. D is the minimum separation distance (0.4 nm).

Similar to the Rabinovich model, the individual terms in Eq. 7.7 relate to the interactions of combinations of substrate, particle and asperity. However, Eq. 7.7 also accounts for interactions between asperities on the two surfaces. In particular, the first three terms in Eq. 7.7 represent, respectively, the interaction of the particle surface with the substrate surface, the micro-scale substrate asperity, and the nano-scale substrate asperity. Additionally, the fourth, fifth and sixth terms describe the contribution from the particle micro-scale asperity interacting with the substrate surface, substrate micro-scale asperity and the substrate nano-scale asperity, respectively. Finally, the particle nano-scale asperity interactions with the substrate surface, substrate micro-scale asperity and substrate nano-scale asperity are represented by the last three terms, respectively. The nano-scale asperity interaction term – i.e., the last term in Eq. 7.7 – represents the contact term, while all other terms are noncontact terms.

The asperity radius and height are given by Rabinovich et al. [136][137] as Eqs. 7.8 and 7.9

$$r_{i,j} = \frac{\lambda_{i,j}^2}{58rms_{i,j}} \quad \text{Eq. 7.8}$$

$$H_{i,j} = 1.817rms_{i,j} \quad \text{Eq. 7.9}$$

It was assumed in this study that an irregular particle has the same value of $\lambda_3, \lambda_4, rms_3$ as an irregular substrate ($\lambda_1, \lambda_2, rms_1$). The nano roughness of the particle (rms_4) was 60 nm. Then the asperity radii and heights of the particle and substrate were calculated

using Eq 7.8 and 7.9. Table 7.5 shows the parameters used in the comparative studies between all models considered so far.

Table 7.5. Parameters used in the comparative study.

Parameter	Rumpf	Rabinovich	Hamaker	Modified Rabinovich
Hamaker constant, A_H	10^{-20} J	10^{-20} J	10^{-20} J	10^{-20} J
The smallest distance, H_0	0.4 nm	0.4 nm	0.4 nm	0.4 nm
Particle radius, R	10 μ m	10 μ m	10 μ m	10 μ m
Roughness of substrate, rms_1	0	1.5 μ m	0	1.5 μ m
Roughness of substrate, rms_2	0 - 80 nm	0 - 80 nm	0	0 - 80 nm
Roughness of particle, rms_3	0	0	0	1.5 μ m
Roughness of particle, rms_4	0	0	0	60nm
Peak-to peak distance of substrate, λ_1	/	1.5 μ m	/	1.5 μ m
Peak-to peak distance of substrate, λ_2	/	0.5 μ m	/	0.5 μ m
Peak-to peak distance of particle, λ_3	/	1.5 μ m	/	1.5 μ m
Peak-to peak distance of particle, λ_4	/	0.5 μ m	/	0.5 μ m

Comparison between the Rumpf, Rabinovich, Hamaker, and the modified Rabinovich (a new model proposed by Casey Q. LaMarche et al) methods is illustrated in Fig. 7.18 with only one adhering contact between the particle and the surface. The black dash curve represents adhesion forces between a rough particle and a rough surface predicted by the modified Rabinovich model. Initially, a rapid reduction in the adhesion forces between the rough particle and the rough surface can be seen (the dashed line). When $rms_2 > 5$ nm, the adhesion forces stabilize. That means when the nanoscale roughness of a substrate surface is larger than a critical rms_2 , here is around 5 nm, rms_2 cannot affect the adhesion forces anymore. Comparing adhesion forces between an irregular particle and a flat substrate surface ($rms_2 = 0$ nm) predicted by these four models, the modified Rabinovich model predicted the smallest interaction due to the rough surface of the irregular particle.

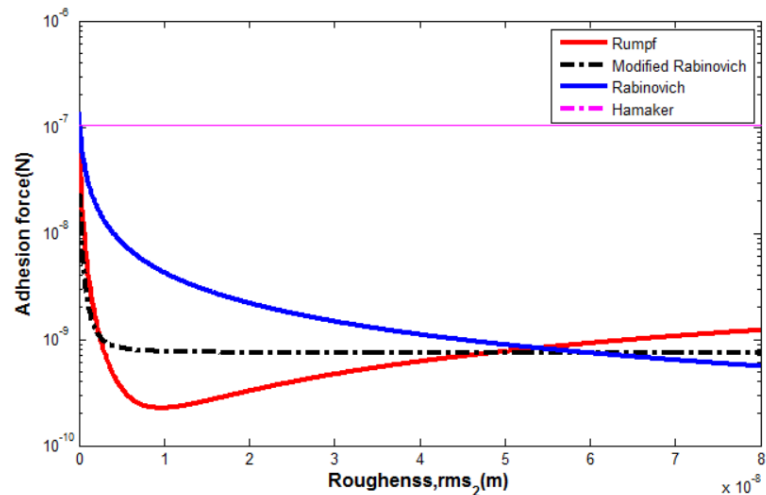


Figure 7.18. Comparison between adhesion forces obtained from the Rumpf, Rabinovich, Hamaker, and modified Rabinovich models for an epoxy substrate and a $10 \mu\text{m}$ epoxy particle separated by H_0 equals to 0.4 nm. Rms_4 is 60 nm

Fig. 7.19 shows the adhesion forces as a function of the roughness of nano asperities (rms_4) on irregular particles. For the Rumpf, Rabinovich, and Hamaker models, the particles are smooth spheres. Therefore, they produce constant adhesion forces when rms_4 is increasing. For the modified Rabinovich model, increasing of rms_4 leads to the reduction of adhesion forces between irregular particles and irregular surfaces.

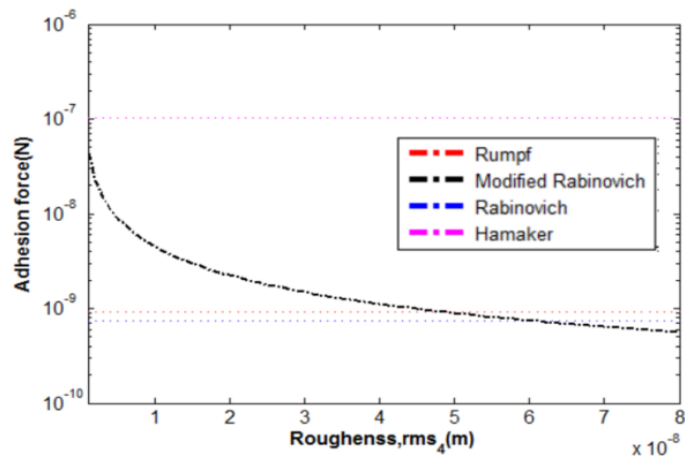


Figure 7.19. Comparison between adhesion forces obtained from the Rumpf, Rabinovich, Hamaker, and the modified Rabinovich models for an epoxy substrate and a 10 μm epoxy particle separated by H_0 equals to 0.4 nm. Rms_2 is 60 nm.

Fig. 7.20 shows the predictions for adhesion forces between irregular particles and irregular surfaces as a function of nanoscale roughness of particle and substrate surfaces. It can be seen that adhesion forces decreased when the nanoscale roughness of irregular particles increased from 0 to 80 nm and the nanoscale roughness of irregular substrates increased from 0 to 80 nm. If we compare the nano asperity effects of particles and substrates on adhesion forces, nanoscale asperities of particles are much more influential on adhesion forces than nanoscale asperities of substrates.

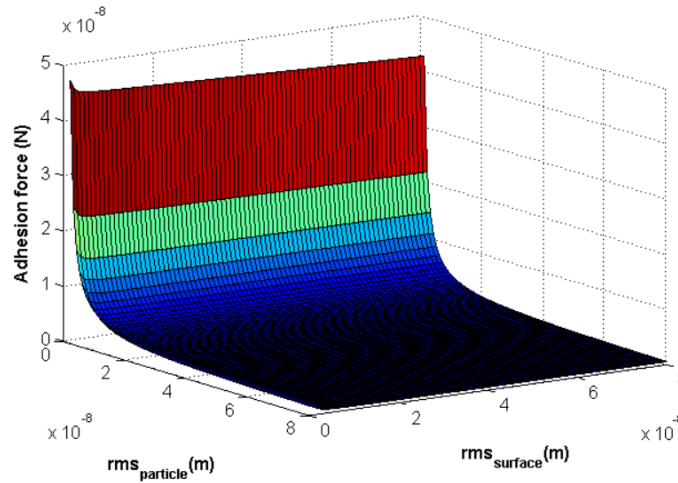


Figure 7.20. Predictions of adhesive forces using the modified Rabinovich model between irregular particles and irregular surfaces as a function of nanoscale rms particle and rms surface.

7.7 Predictions of irregular particle movements on uneven surface caused by moving water

Considering the facts presented in the sections above, the removal of irregular particles from uneven surfaces by slowly moving water (see Chapter 6) can be reconsidered. As the previous section stated, adhesion forces between spherical particles and nano/micro rough surfaces estimated using the Rumpf and Rabinovich methods are dramatically smaller than those calculated following the Hamaker method. The reason is that the contact area between particles and substrate surface are decreased by nano/microscale rough structures distributed on uneven surfaces eventually leading to a reduction in interaction forces. Therefore, the critical size of particles which could be removed by viscous shear stresses from rough surfaces should be smaller than from flat surfaces. In Fig. 7.21 the critical sizes of particles are presented which could be removed by water flow over rough surfaces following the modified Rabinovich model for an average viscous shear stress of 1.59 N/m^2 . Clearly, the critical sizes of particles that can

be removed decreased in all three movements when surface roughness increases. When the surface roughness is 5 nm, all of particles smaller than 10.2 μm could be removed by individual or combinations of lifting, sliding and rolling movements. Comparing to the particles adhered to the flat surface (Fig.6.8), particles adhered to a nanoscale rough surface can be clearly removed more easily under the same value of viscous shear stress.

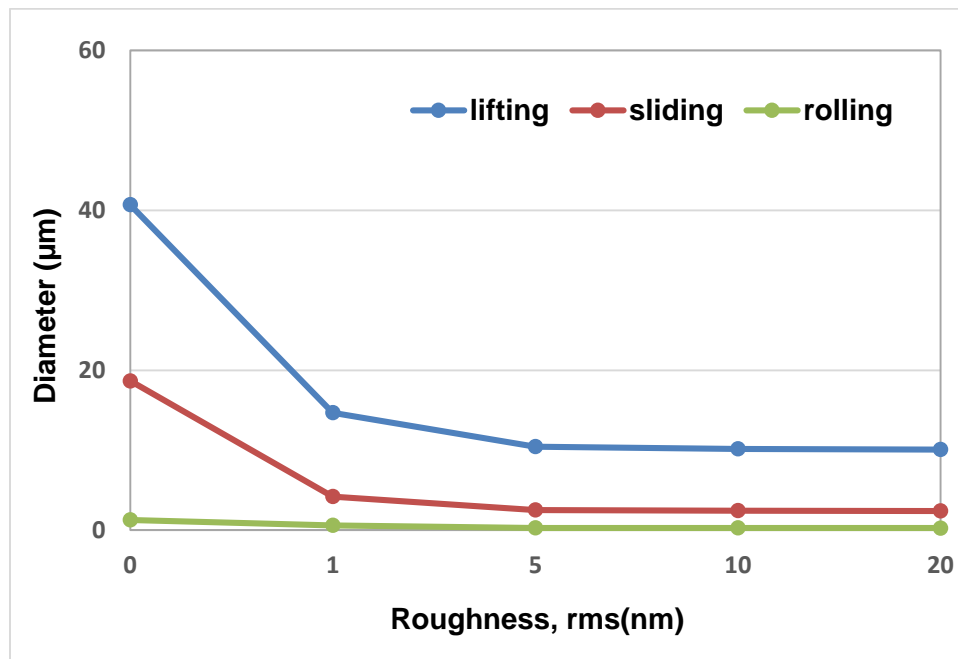


Figure 7.21. Critical sizes of particles which could be removed from different rough surfaces by shear stresses from slowly moving water. Modified Rabinovich model.

The simulation results of critical sizes of particles which could be removed by lifting (as an example) from rough surfaces with increasing rms_2 are shown in Fig. 7.22. Corresponding to Fig. 6.8 in chapter 6.5, the critical diameter of the particles was a constant equal to about 84.6 μm from the Hamaker method and independent of the surface roughness. From the Rumpf and Rabinovich methods, the critical diameter is non-monotonically and monotonically decreasing, respectively. Both of them exhibit a

remarkable decrease in the critical diameter of particles when the surface has nanoscale roughness characteristics. The critical diameters predicted using the modified Rabinovich model exhibited a rapid reduction when the nanoscale roughness of the substrate surface (rms_2) is smaller than 1 nm. Then the reduction of the critical diameters becomes less significant when rms_2 is larger than 1 nm.

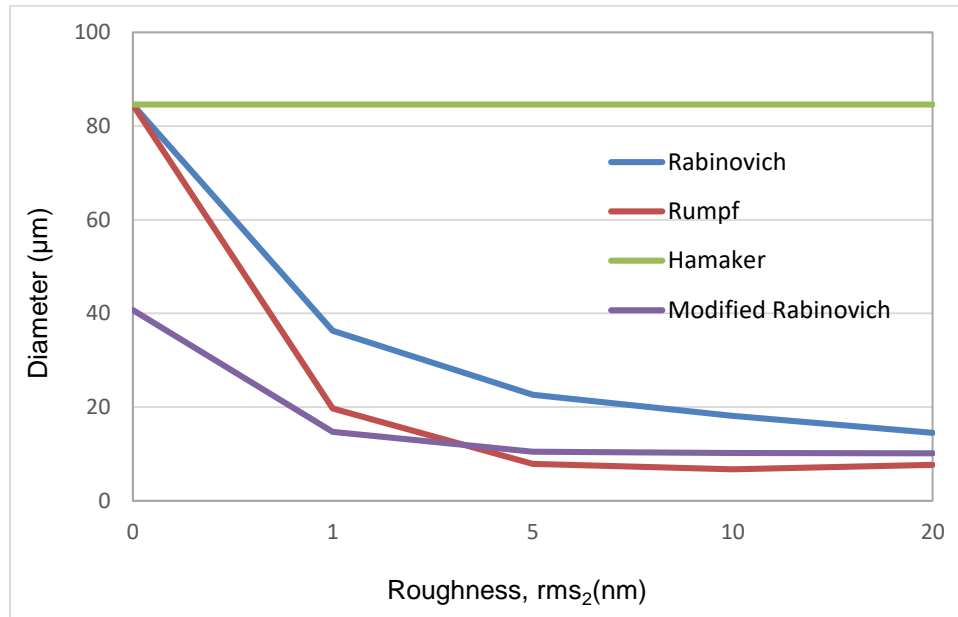


Figure 7.22. Critical sizes of particles which could be removed by lifting from different rough surfaces subjected to gravitational water flow. Various models.

7.7 Summary

In this chapter, adhesion forces on nano/micro hierarchical structure surfaces were calculated using the Rumpf and Rabinovich models. Simulation results show that adhesion forces calculated following the Rumpf model with nano-level asperities on substrate surfaces are significantly smaller than the forces on flat epoxy surfaces from the JKR and Hamaker models (Chapter.6). According to the simulation results from the Rabinovich model, the roughness effect of secondary asperities on adhesion forces is

much larger than that of primary asperities. Therefore, regardless of adhering particle sizes, the nano surface structures on the top of micro surface structures contribute much more to the global adhesive forces than just the micro surface irregularities.

It was also shown in this research that adhesion forces decreased when the nanoscale roughness of irregular particles and irregular substrates increased. In addition, nanoscale asperities of particles are much more influential on adhesion forces than nanoscale asperities of substrates. Removal of irregular particles from uneven surfaces by slowly moving water flow was finally reconsidered. The critical size of particles which could be removed by water flows from rough surfaces was found to be significantly smaller than from flat surfaces.

Chapter 8: Conclusions

- Unidirectional GRP composites develop significantly different degradation mechanisms with strong synergistic effects when exposed to individual and cyclic UV radiation, water condensation and temperature. The average weight losses under cyclic conditions for all six tested GRP composites were found to be about 100% larger than the weight gains from the simple superposition of the UV and condensation environments for the same composites.
- The sums of the individual UV and water condensation aging effects on weight changes are positive with weight gains, whereas the weight changes under the cyclic combined conditions are negative with weight losses for all six tested GRP composites.
- A comparison of degradation by UVA and UVB indicate that UVB caused more severe damage and higher degradation rates in the GPR composites.
- Surface yellowing shows that composite degradation caused by UV light only occurred in the surface layer of the composites with a thickness around 10 μm .

- FTIR analysis shows that photodegradation of VE resin led to a decrease of C-O, C-O-C, C-CO-O groups in VE polymer chain.
- In the polymer degradation experiments, it has been shown that all tested pure polymers except PVC when exposed to individual and cyclic UV radiation, water condensation and temperature do not develop significantly strong synergistic degradation.
- UV degradation of polymeric surfaces is strongly dependent on UV wavelength, intensity and exposure time.
- It is also shown that UV intensity and inclinations determine the local degradation rates of the material which can be numerically simulated from the global degradation rates for a material determined experimentally.
- The initial irregular, sinusoidal surface of the material eventually degraded to a flat surface under a long period of exposure to UV radiation regardless of the irradiation angle. Although the simulations were performed in the setting of sinusoidal surfaces, the methodology is equally applicable to any irregular surfaces.
- Surface shape effects show that polymer surfaces with high amplitudes and high frequencies degrade faster under UV than the surfaces with low amplitudes and

low frequencies. Furthermore, surface frequency affects degradation rates more than surface amplitude.

- The UV planarization effect on irregular polymeric surfaces observed numerically was finally experimentally verified in this work by the UV testing of neat epoxy specimens at elevated temperature. The surface roughness of the specimens was reduced by about 12.5% after 1000 hours of UV exposure.
- Hydrodynamic modeling was performed to estimate the viscous shear stresses generated by slowly moving water on polymer and GRP surfaces affected by synergistic aging by UV and water flows.
- It has been shown that when the surface roughness of the specimens increases, the average viscous shear stress decreases negatively affecting the efficiency of particle removal. On the other hand, when the inclination of the surface increases, the average viscous shear stress increases positively affecting the efficiency of particle removal.
- The movement of polymer particles on polymer surfaces strongly depends on particle size, water flow rate, surface morphology, and the viscous shear stresses caused by the moving water.

- It was also shown in this research that depending on particle sizes and magnitudes of viscous shear stresses, small particles could be moved by rolling only, and large particles could be cleared by a combination of rolling, sliding and lifting.
- The particle removal by water model was verified experimentally by showing that the average size of epoxy particles moved by water on a GRP surface increases in the direction of the water flow.
- Adhesion forces simulated by the Rumpf model with nanoscale asperities on the surface are three orders of magnitude smaller than those on a flat epoxy surface either predicted by either the JKR or Hamaker method.
- According to the simulation results using the Rabinovich model, the roughness effect of secondary asperities on adhesion forces is much larger than that of primary asperities. Therefore, regardless of adhering particles sizes, the nano structures on the top of micro structures are more critical in affecting the adhesion force than the micro structure in the hierarchical structure.
- The investigation of adhesion forces with multiple asperities in contact using Kumar's model indicated that the number of contacts dominates the magnitude of the adhesion force with a large nanoscale surface roughness. When the surface

becomes smooth, particle sizes rather than the number of contacts affect the adhesion forces.

- Comparing adhesion forces of the Rumpf, Rabinovich, Hamaker and the modified Rabinovich models, the modified Rabinovich model obtained the smallest interaction when substrate surfaces are flat ($rms_2 = 0$ nm) due to the reduction of adhesion forces caused by the rough surface of the irregular particles.
- Comparing adhesion forces affected by nano asperities on irregular particles and irregular substrates, nanoscale asperities of irregular particles are more important in affecting the adhesion forces than the nanoscale asperities of the substrates.
- When both particles and substrate surfaces are irregular, particles adhered to a nanoscale rough surface can be cleared is much smaller compared to particles adhered to a flat surface by the same value of viscous shear stress.

References

- [1] Akovali Güneri. Handbook of Composite Fabrication. Rapra Technology LTD 2001.
- [2] TP Sathishkumar, S Sathishkumar, J NaveenS. Glass Fiber-Reinforced Polymer Composites - A Review. Journal of Reinforced Plastics and Composites, 33(13). (2014) 1258-1275.
- [3] Ru-Min Wang, Shui-Rong Zheng and Ya-Ping Zheng. Polymer Matrix Composites and Technology. Woodhead Publishing 2011.
- [4] Klara Aniskevich, Olesja Starkova, Juris Jansons, Andrej Aniskevich. Long-term Deformability and Aging of Polymer Matrix Composites. Nova Science Publishers 2012.
- [5] Y. Hu, X. Li, A.W. Lang, Y. Zhang, S.R. Nutt, Water Immersion Aging of Polydicyclopentadiene Resin and Glass Fiber Composites, Polym. Degrad. Stab. 124 (2016) 35-42.
- [6] J. Park, P. Shin, Z. Wang, D. Kwon, J. Choi, S. Lee, K. L. DeVries. The Change in Mechanical and Interfacial Properties of GF and CF Reinforced Epoxy Composites after Aging in NaCl Solution, Compos. Sci. Technol. 122 (2016) 59-66.
- [7] J. Wang, H. GangaRao, R. Liang, D. Zhou, W. Liu, Y. Fang. Durability of Glass Fiber-Reinforced Polymer Composites under the Combined Effects of Moisture and Sustained Loads, J. Reinf. Plast. Compos. 34 (21) (2015)1739-1754.
- [8] M. Evans, A Statistical Degradation Model for the Service Life Prediction of Aircraft Coatings: With a Comparison to an Existing Methodology, Polym. Test. 31 (1) (2012) 46-55.
- [9] S.G. Croll, Application and Limitations of Current Understanding to Model Failure Modes in Coatings, J. Coat. Technol. Res. (2012) 15-27.
- [10] S. Kiil. Model-based Analysis of Photoinitiated Coating Degradation under Artificial Exposure Conditions, J. Coat. Technol. Res. 9 (4) (2012) 375-398.
- [11] Brian Hinderliter, Stuart Croll. Monte Carlo Approach to Estimating the Photodegradation of Polymer Coatings, JCT Research, 2 (2005) 483-491.

- [12] Jonathan W. Martin, T. Nguyen, Eric Byrd, Brian Dickens, Ned Embree. Relating Laboratory and Outdoor Exposures of Acrylic Melamine Coatings I. Cumulative Damage Model and Laboratory Exposure Apparatus. *Polymer Degradation and Stability*, (2002) 193-210.
- [13] Jonathan W. Martin. A Stochastic Model for Predicting the Service Life of Photolytically Degraded Poly(methyl methacrylate) Films. *Applied Polymer*, (1984) 777-794.
- [14] T. Lu, E. Solis-Ramos, Yun-Bo Yi, M. Kumosa. Synergistic Environmental Degradation of Glass Reinforced Polymer Composites, *Polym. Degrad. Stab.* 131 (2016) 1-8.
- [15] T. Lu, E. Solis-Ramos, Y. Yi, M. Kumosa. Particle removal Mechanisms in Synergistic Aging of Polymers and Glass Reinforced Polymer Composites under Combined UV and Water, *Compos. Sci. Technol.* 153 (2017) 273-281.
- [16] B.G. Kumar, R.P. Singh, T. Nakamura. Degradation of Carbon Fiber-Reinforced Epoxy Composites by Ultraviolet Radiation and Condensation, *J. Compos Mater.* 36 (2002) 2713-2721.
- [17] D.E. Mouzakis, H. Zoga, C. Galiotis. Accelerated Environmental Ageing Study of Polyester/Glass Fiber Reinforced Composites (GFRPCs), *Composites Part B* 39 (2008) 467-475.
- [18] C. Dubois, L. Monney, N. Bonenet, A. Chambaudet, Degradation of an epoxy-glass-fibre laminate under photo-oxidation/leaching complementary constraints, *Composites Part A* 30(1999) 361-368.
- [19] A. F. Heude, E. Richaud, E. Desnoux, X. Colin. Influence of Temperature, UV-Light Wavelength and Intensity on Polypropylene Photothermal Oxidation, *Polym. Degrad. Stab.* 100 (2014) 10-20.
- [20] J.W. Martin, Quantitative Characterization of Spectral Ultraviolet Radiation-Induced Photodegradation in Coating Systems Exposed in the Laboratory and the Field, *Prog. Org. Coat.* 23 (1) (1993) 49-70.
- [21] George Wypych. *Handbook of UV Degradation and Stabilization*, ChemTec Publishing 2011.
- [22] Sabu Thomas Joseph, Sant Kumar Malhotra, Koichi Goda, Meyyarappallil Sadasivan SreekalaKuruvilla. *Polymer Composites*. Singapore Wiley 2012.

- [23] D. Chung, L. Deborah. Composite Materials: Science and Applications. Springer 2010.
- [24] Composite materials. Advancing the Chemical Sciences:
<http://www.rsc.org/Education/Teachers/Resources/Inspirational/resources/4.3.1.pdf>
- [25] Avila Paulo, C.M., Santos, D.B., A.F. Polymer Degradation and Stability. Materials Characterization, (2003) 281-291.
- [26] Bunsell A.R. Fiber Reinforcements for Composite Materials. Amsterdam: Elsevier 1988.
- [27] W. D. Callister, John Wiley. Materials Science and Engineering: An Introduction 2nd Edition. New York: J. Wiley and Sons Inc. 1991.
- [28] D.Hull, T.W.Clyne. An Introduction to Composite Materials Second Edition. New York: Cambridge University Press 1996.
- [29] Bingham T. Wallenberger, Paul A. Frederick. Fiberglass and Glass Technology: Energy-Friendly Compositions. Springer (2010).
- [30] Biron Michel. Thermosets and Composites. UK: William Andrew 2014.
- [31] Ratna Debdatta. Handbook of Thermoset Resins. UK: Lightning Source Inc. 2009.
- [32] Hanna Dodiuk, H. Goodman Sidney. Handbook of Thermoset Plastics Thrid Edition. USA: William Andrew 2014.
- [33] Donenov Zhubanov, B.K.B.A. Polymer Science, (1992) 819.
- [34] Tien-Cuong Nguyen Bai, Xiao-Ling Zhao, Riadh Al-Mahaidi Yu. Effects of Ultraviolet Radiation and Associated Elevated Temperature on Mechanical Performance of Steel/CFRP Double Strap Joints. Composite Structures, (2012) 3563-3573.
- [35] Vistasp M. Karbhari. Durability of Composites for Civil Structural Applications. Woodhead and CRC Press 2007.
- [36] Lide R David. CRC Handbook of Chemistry and Physics 76th Edition. CRC Press 1995.
- [37] Pauling L. General Chemistry 3rd ed. W. H. Freeman and Company 1970.

- [38] Chi-Hung Shen, George S. Springer. Environmental Effects on the Elastic Moduli of Composite Materials, *Journal of Composite Materials*, (1977) 250-264
- [39] L. Kumosa Benedikt, D. Armentrout, M. Kumosa B. Moisture Absorption Properties of Unidirectional Glass/polymer Composites Used in Composite (non-ceramic) Insulators. *Composites: Part A*, (2004) 1049-1063.
- [40] S. Roy, W. X. Xu, S. J. Park, K. M. Liechti. Anomalous Moisture Diffusion in Viscoelastic Polymers: Modeling and Testing, *Journal of Applied Mechanics*, (1999) 391-396.
- [41] S. P. Phifer. *Hygrothermal Evaluation of Pultruded Polymer Composite Laminates — Experimentation, Analysis, and Prediction*. Blacksburg: VA: Virginia Tech; 2003.
- [42] Shen CH, Springer GS. *Moisture Absorption and Desorption of Composite Materials, Environmental Effects on Composite Materials*. Westport, CT: Technomic Publishing Company 1981.
- [43] M.W. Myer, C.T. Herakovich, S.M. Milkovich, J.S. Short. Temperature Dependence of Mechanical and Thermal Expansion Properties of T300/5208 Graphite/Epoxy. *Composites*, 14 (3) (1983) 276-280.
- [44] D.L. Hiemstra, N.R. Sottos. Thermally Induced Interfacial Microcracking in Polymer Matrix Composites, *Journal of Composite Materials*, 27 (10) (1993) 1030-1051.
- [45] Tao Xua, Su-Seng Li, Guoqiang Pang. Effects of Ultraviolet Radiation on Morphology and Thermo-mechanical Properties of Shape Memory Polymer Based Syntactic Foam. *Composite Part A*, 42 (10) (2011) 1525-1533.
- [46] J.E. Guillet. Fundamental Processes in the UV Degradation and Stabilization of Polymers, *Chemical Transformations of Polymers*, (1972) 135-144.
- [47] Henry R. Phelps, Edward R. Long, Jr. Property Changes of a Graphite/Epoxy Composite Exposed to Nonionizing Space Parameters, *Journal of Composite Materials*, 14 (4) (1980) 334-341.
- [48] Alfred Tcherbi-Narteh, Mahesh Hosur, Eldon Triggs, Shaik Jeelani. Thermal Stability and Degradation of Diglycidyl Ether of Bisphenol A Epoxy Modified with Different Nanoclays Exposed to UV Radiation, *Polymer Degradation and Stability*, 98 (3) (2013) 759-770.

- [49] P. Davies, F. Mazéas, P. Casari. Sea Water Aging of Glass Reinforced Composites: Shear Behaviour and Damage Modelling. *Journal of Composite Materials*, 35 (15) (2001) 1343-1372.
- [50] Fritz Larsson. The Effect of Ultraviolet Light on Mechanical Properties of Kevlar 49 Composites. *Journal of Reinforced Plastics and Composites*, 5 (1) (1986) 19-22.
- [51] W.B. Liao F.P.Tseng. The Effect of Long-Term Ultraviolet Light Irradiation on Polymer Matrix Composites. *Polymer Composites*, (1998) 440-445.
- [52] Bénédicte Mailhot, Sandrine Morlat-Thérias, Mélanie Ouahioune, Jean-Luc Gardette. Study of the Degradation of an Epoxy/Amine Resin, 1. *Macromolecular Chemistry and Physics*, 206 (5) (2005) 575-584.
- [53] R. Scaffaro, N. Tzankova Dintcheva, F.P. La Mantia. A New Equipment to Measure the Combined Effects of Humidity, Temperature, Mechanical Stress and UV Exposure on the Creep Behaviour of Polymers. *Polymer Testing*, 27 (1) (2008) 49-54.
- [54] Edson Cocchieri Botelho, José Carlos Bravim Júnior, Michelle Leali Costa, Maria Candida Magalhaes de Faria. Environmental Effects on Thermal Properties of PEI/Glass Fiber Composite Materials. *Journal of Aerospace Technology and Management*, (2013) 241-254.
- [55] Marcos A.J. Batista, Raul P. Moraes, Jayne C.S. Barbosa, Pedro C. Oliveira, Amilton M. Santos. Effect of the Polyester Chemical Structure on the Stability of Polyester–Melamine Coatings When Exposed to Accelerated Weathering, *Progress in Organic Coatings* 71 (2011) 265-273.
- [56] J. Nicholas, M. Mohamed, G.S. Dhaliwal, S. Anandan, K. Chandrashekhara. Effects of Accelerated Environmental Aging on Glass Fiber Reinforced Thermoset Polyurethane Composites. *Compos B Eng*, 94 (2016) 370-378.
- [57] Alexandre de Souza Rios, Wanderley Ferreirade Amorim Júnior, Elineudo Pinhode Moura, Enio Pontes de Deus, Judith Pessoad e Andrade Feitosa. Effects of Accelerated Aging on Mechanical, Thermal and Morphological Behavior of Polyurethane/Epoxy/Fiberglass Composites. *Polymer Testing*, 50 (2016) 152-163.
- [58] I.B.C.M. Rocha, S. Raijmaekers, R.P.L. Nijssen, F.P. van der Meer, L.J. Sluys. Hygrothermal Ageing Behaviour of A Glass/Epoxy Composite Used in Wind Turbine Blades. *Composite Structures*, 174 (2017) 110-122.
- [59] Marialaura Clausi, M. Gabriella Santonicola, Luigi Schirone, Susanna Laurenzi. Analysis of Ultraviolet Exposure Effects on the Surface Properties of

- Epoxy/Graphene Nanocomposite Films on Mylar Substrate. *Acta Astronautica*, 134 (2017) 307-313.
- [60] Noamen Guermazi, Amira B. Tarjem, Imen Ksouri, Hassine F. Ayedi. On the Durability of FRP Composites for Aircraft Structures in Hygrothermal Conditioning. *Composites Part B: Engineering*, 85 (2016) 294-304.
- [61] S.G. Croll, B.R. Hinderliter, S. Liu. Statistical Approaches for Predicting Weathering Degradation and Service Life. *Progress in Organic Coatings*, (2006) 75-87.
- [62] Stuart Croll, Hinderliter Brian. A Framework for Predicting the Service Lifetime of Composite Polymeric Coatings. *J Mater Sci*, (2008) 6630-6641.
- [63] Enrique Guzmán, Jo ð Cugnoni, Thomas Gmür. Multi-Factorial Models of a Carbon Fibre/Epoxy Composite Subjected to Accelerated Environmental Ageing. *Composite Structures*, 111 (2014) 179-192.
- [64] F. Tian, Z. Zhong, Y.H. Pan. Modeling of Natural Fiber Reinforced Composites under Hygrothermal Ageing. *Composite Structures*, (2018) 144-152.
- [65] Kurt A. Woodde, Ségolène de Robien. *A Quantitative Model for Weathering-induced Mass Loss in Thermoplastic Paints*. Springer. 2009.
- [66] S. Kiil. Mathematical Modeling of Photoinitiated Coating Degradation: Effects of Coating Glass Transition Temperature and Light Stabilizers. *Progress in Organic Coatings*, (2013) 1730-1737.
- [67] T. Lu. Degradation of High Voltage Glass Fiber-Reinforced Polymer Matrix Composites by Aggressive Environmental Conditions. MS thesis, University of Denver, Denver Colorado, August 2014.
- [68] Zhi Chen, Lifei Zheng, QingpingJin, Xiaoqing Li. Durability Study on Glass Fiber Reinforced Polymer Soil Nail via Accelerated Aging Test and Long-Term Field Test, *Polymer Composites*. (2015) 1-11.
- [69] P. B öer, L. Holliday, Thomas H.K. Kang. Independent Environmental Effects on Durability of Fiber-Reinforced Polymer Wraps in Civil Applications: A Review, *Construction and Building Materials*. 48 (2013) 360-370.
- [70] G. Carra, V. Carvelli. Ageing of Pultruded Glass Fibre Reinforced Polymer Composites Exposed to Combined Environmental Agents, *Compos. Structure*. 108 (2014) 1019-1026.
- [71] B.G. Kumar, R.P. Singh, T. Nakamura. Degradation of Carbon Fiber-Reinforced Epoxy Composites by Ultraviolet Radiation and Condensation, *J. Compos Mater*. 36 (2002) 2713-2721.

- [72] Dionysis E. Mouzakis, Helen Zoga, Costas Galiotisa. Accelerated Environmental Ageing Study of Polyester/Glass Fiber Reinforced Composites (GFRPCs), *Composites: Part B*. 39 (2008) 467–475.
- [73] Wiki: UV light <https://en.wikipedia.org/wiki/Ultraviolet>.
- [74] Alexandre François-Heude, Emmanuel Richaud, Eric Desnoux, Xavier Colin. Influence of Temperature, UV-Light Wavelength and Intensity on Polypropylene Photothermal Oxidation, Polymer Degradation and Stability. 100 (2014) 10-20.
- [75] B. Ranby, J.F. Rabek. Photodegradation, Photo-Oxidation and Photostabilization of Polymers. John Wiley and Sons, London. 1975.
- [76] Andrew W Signor, Mark R VanLandingham, Joannie W Chin. Effects of Ultraviolet Radiation Exposure on Vinyl Ester Resins: Characterization of Chemical, Physical and Mechanical Damage, Polymer Degradation and Stability. 79(2003) 359-368.
- [77] Dan Rosu, Liliana Rosu, Constantin N. Cascaval. Effect of Ultraviolet Radiation on Vinyl Ester Network Based on Bisphenol A, *Journal of Photochemistry and Photobiology A: Chemistry*. 194 (2008) 275-282.
- [78] L. Gautier, B. Mortaigne, V. Bellenger. Interface Damage Study of Hydrothermally Aged Glass Fibre-Reinforced Polyester Composite, *Composites Science and Technology*. 59 (1999) 2329-2337.
- [79] S. Pavlidou, C.D. Papaspyrides. The Effect of Hygrothermal History on Water Sorption and Interlaminar Shear Strength of Glass/Polyester Composites with Different Interfacial Strength, *Composites: Part A*. 34 (2003) 1117-1124.
- [80] Z.A. Mohd Ishak, A. Ariffin, R. Senawi. Effects of Hygrothermal Aging and a Silane Coupling Agent on the Tensile Properties of Injection Molded Short Glass Fiber Reinforced Poly(butylene terephthalate) Composites, *EurPolym J.* (2001) 35-47.
- [81] Carol L. Schutte. Environmental Durability of Glass-Fiber Composites. *Materials Science and Engineering*, (1994) 265-324.
- [82] E. Solis-Ramos, M. Kumosa. Synergistic Effects in Stress Corrosion Cracking of Glass Reinforced Polymer Composites, *Polymer Degradation and Stability*. 136 (2017) 146-157.
- [83] Marcos A.J. Batista, Raul P. Moraes¹, Jayne C.S. Barbosa, Pedro C. Oliveira, Amilton M. Santos. Effect of the Polyester Chemical Structure on the Stability of Polyester–Melamine Coatings When Exposed to Accelerated Weathering, *Progress in Organic Coatings*. 71 (2011) 265-273.

- [84] J K. Fink, High Performance Polymers, Elsevier. (2008) 347-390.
- [85] Ollier-Dureault, V, Bosse, B. Photooxidation of Anhydride-Cured Epoxies: FTIR Study of the Modifications of the Chemical Structure, *J. Appl. Polym. Sci.* 70 (1998) 1221-1237.
- [86] H.A. Al-Turaif, Surface Morphology and Chemistry of Epoxy-based Coatings after Exposure to Ultraviolet Radiation, *Prog. Org. Coat.* 76 (4) (2013) 677-681.
- [87] Dupuis, F. Perrin, A.U. Torres, J. Habas, L. Belec, J. Chailan. Photo-Oxidative Degradation Behavior of Linseed Oil Based Epoxy Resin, *Polym. Degrad. Stab.* 135 (2017) 73-84.
- [88] S. Commereuc, H. Askanian, V. Verney, A. Celli, P. Marchese, C. Berti. About the End Life of Novel Aliphatic and Aliphatic-Aromatic (co)polyesters after UV-weathering: Structure/Degradability Relationships, *Polym. Degrad. Stab.* 98 (7) (2013) 1321-1328.
- [89] A. Ghasemi-Kahrizsangi, H. Shariatpanahi, J. Neshati, E. Akbarinezhad. Degradation of Modified Carbon Black/Epoxy Nanocomposite Coatings under Ultraviolet Exposure, *Appl. Surf. Sci.* 353 (2015) 530-539.
- [90] Z. Chen, L. Zheng, Q. Jin, X. Li. Durability Study on Glass Fiber Reinforced Polymer Soil Nail via Accelerated Aging Test and Long-term Field Test, *Polym. Compos.* 2015 1-11.
- [91] B. Hinderliter, S. Croll, Predicting Coating Failure Using the Central Limit Theorem and Physical Modeling, *ECS Trans.* 24(1) (2010) 1-26.
- [92] E. Yousif, R. Haddad. Photodegradation and Photostabilization of Polymers, Especially Polystyrene: Review, *Springerplus* 2 (1) (2013) 398.
- [93] T.T.X. Hang, N.T. Dung, T.A. Truc, N.T. Duong, B.V. Truoc, P.G. Vu, T. Hoang, D.T.M. Thanh, M. Olivier. Effect of Silane Modified Nano ZnO on UV Degradation of Polyurethane Coatings, *Prog. Org. Coat.* 79 (2015) 68-74.
- [94] H. Makki, K.N.S. Adema, E.A.J.F. Peters, J. Laven, L.G.J. van der Ven, R.A.T.M. van Benthem, G. de With, A Simulation Approach to Study Photo-Degradation Processes of Polymeric Coatings, *Polym. Degrad. Stab.* 105 (2014) 68-79.

- [95] V.C. Malshe, G. Waghoo. Weathering Study of Epoxy Paints, *Prog. Org. Coat.* 51 (4) (2004) 267-272.
- [96] V.C. Malshe, G. Waghoo. Chalk Resistant Epoxy Resins, *Prog. Org. Coat.* 51 (3) (2004) 172-180.
- [97] P. Incropera, D. P. Dewitt, T.L. Bergman, A.S. Lavine, *Fundamentals of Heat and Mass Transfer*, 6th Edition, Hoboken, 2006.
- [98] T. Lu, E. Solis-Ramos, Yun-Bo Yi, M. Kumosa. UV Degradation Model for Polymers and Polymer Matrix Composites, *Polym. Degrad. Stab.* 154 (2018) 203-210.
- [99] B. Carnahan, H. A. Luther, J.O. Wilkes, *Applied Numerical Methods*, Wiley, New York, 1969.
- [100] Iman Goldasteh, Goodarz Ahmadi, Andrea R. Ferro. Monte Carlo Simulation of Micron Size Spherical Particle Removal and Resuspension from Substrate under Fluid Flows, *Journal of Aerosol Science.* 8 (7) (2013) 62-71.
- [101] Hubbe, Martin A. Theory of Detachment of Colloidal Particles from Flat Surfaces Exposed to Flow, *Colloids and Surfaces.* 12 (1984) 151-178.
- [102] M. Soltani, G. Ahmadi, On Particle Adhesion and Removal Mechanisms in Turbulent Flows, *Journal of Adhesion Science and Technology.* 8 (7) (1994) 763-785.
- [103] M.B. Ranade, Adhesion and Removal of Fine Particles on Surfaces, *Aerosol Science and Technology.* 7 (2) (1976) 161-176.
- [104] J. Visser, Adhesion of Colloidal Particles. In: Matijevic E., *Surface and Colloid Science*, John Wiley & Sons. New York, 1976.
- [105] H.C. Hamaker, The London-Van Der Waals Attraction Between Spherical Particles, *Physical IV.* 11 (23) (1937) 1058-1072.
- [106] G özinger, M. and Peukert, W. Particle Adhesion Force Distributions on Rough Surfaces, *Langmuir.* 20 (13) (2004) 5298-5303.
- [107] Q. Li, V. Rudolph, W. Peukert. London-van Der Waals Adhesiveness of Rough Particles, *Powder Technology.* 161 (2006) 248-255.
- [108] J. Visser, Particle Adhesion and Removal: A Review, *Particulate Science and Technology.* 13 (1995) 169-196.

- [109] G.M. Burdick, N. S. Berman, S.P. Beaudoin, Describing Hydrodynamic Particle Removal from Surfaces, *Thin Solid Films*. 488 (2005) 116-123.
- [110] G.M. Burdick, N. S. Berman, S.P. Beaudoin, Describing Hydrodynamic Particle Removal from Surfaces Using the Particle Reynolds Number, *Nanoparticle Research*. 3 (5) (2001) 455-467.
- [111] M.L. Zoetewij, J. C. J. van der Donck, R. Versluis. Particle Removal in Linear Shear Flow: model Prediction and Experimental Validation, *Adhesion Sci. Technol.* 23 (6) (2009) 899-911.
- [112] K.L. Johnson, K. Kendall, A.D. Roberts. Surface Energy and the Contact of Elastic Solids, *Proceedings of the Royal Society of London A: Mathematical, Physical and Engineering Sciences*. 324 (1971) 301-313.
- [113] Goodarz Ahmadi, Shiguang Guo, Xinyu Zhang. Particle Adhesion and Detachment in Turbulent Flows Including Capillary Forces, *Particulate Science and Technology*. 25(2007) 59–76.
- [114] Iman Goldasteh, Goodarz Ahmadi, Andrea Ferro. A Model for Removal of Compact, rough, Irregularly Shaped Particles from Surfaces, *The Journal of Adhesion*. 88(9) (2012) 766-786.
- [115] B.V. Derjaguin, V.M. Muller, and Y.P. Toporov, On the Role of Molecular Forces in Contact Deformations (critical remarks concerning Dr. Tabor's report), *Journal of Colloid and Interface Science*, 67(2) (1978) 378-379.
- [116] Zhang, Xinyu, and Goodarz Ahmadi, Effects of Capillary Force and Surface Deformation on Particle Removal in Turbulent Flows, *Journal of Adhesion Science and Technology* 21.16 (2007) 1589-1611.
- [117] D. Tabor, Surface Forces and Surface Interactions, *Journal of Colloid and Interface Science*. 58(1) (1977) 2-13.
- [118] D.E. Packham, Work of Adhesion: Contact Angles and Contact Mechanics. *International Journal of Adhesion and Adhesives*, 16(2) (1996) 121-128.
- [119] A.H.I. Essawey, Microparticle Detachment from Surfaces by Fluid Flow. Doctoral dissertation, University of Notre Dame, Notre Dame, Indiana, January 2004
- [120] Comsol 4.3, *Comsol Multiphysics User's Guide*. Burlington.

- [121] Norbert Riefler, et al., Particle Deposition and Detachment in Capillary Sphere Packings, *Chemical Engineering*. 174 (1) (2011) 93-101.
- [122] O'Neill, M. E. A Sphere in Contact with a Plane Wall in a Slow Linear Shear Flow, *Chem. Eng. Sci.* 23 (1968) 1293-1298.
- [123] Soltani, M. and Ahmadi, G. On Particle Adhesion and Removal Mechanisms in Turbulent Flows, *Journal of Adhesion Science and Technology*, 8 (7) (1994) 763-785.
- [124] C. Ozalp, A. Pinarbasi, B. Sahin, Experimental Measurement of Flow Pass Cavities of Different Shapes, *Experimental Thermal and Fluid Science*. 34 (5) (2010) 505-515.
- [125] G. Lomboy, S. Sundararajan, K. Wang, S. Subramaniam, A Test Method for Determining Adhesion Forces and Hamaker Constants of Cementitious Materials Using Atomic Force Microscopy, *Cement and Concrete Research*. 41 (2011) 1157–1166.
- [126] J.H. Clint, A.C. Wicks, Adhesion under Water: Surface Energy Considerations. *International Journal of Adhesion and Adhesives*. 21 (4) (2001) 267-273.
- [127] K.L. Johnson, *Mechanics of Adhesion*, *Tribology International*. 31 (8) (1998) 413-418.
- [128] M. Götzinger, and W. Peukert, Particle Adhesion Force Distributions on Rough Surfaces, *Langmuir*. 20 (13) (2004) 5298-5303.
- [129] W.C. Wake, *Adhesion and the Formulation of Adhesives*, second ed. Applied Science Publishers, London, 1982.
- [130] Fabio L. Leite, Carolina C. Bueno, Alessandra L. Da Róz, Ervino C. Ziemath, Osvaldo N. Oliveira Jr. Theoretical Models for Surface Forces and Adhesion and Their Measurement Using Atomic Force Microscopy, *International Journal of Molecular Sciences*. 13 (2012) 12773-12856.
- [131] J. N. Israelachvili, *Intermolecular and Surface Forces*. Academic Press, New York, 1985.
- [132] Kevin Kendall. Adhesion: Molecules and Mechanics, *Science*. 263(5154) (1994) 1720-1725.

- [133] K.L. Johnson, K. Kendall, A.D. Roberts. Surface Energy and the Contact of Elastic Solids, Proc. R. Soc. London, A. 324 (1971) 301–313.
- [134] K. Fuller, D. Tabor. The Effect of Surface Roughness on the Adhesion of Elastic Solids. Proc. R. Soc. Lond. A. 345 (1975) 327–342.
- [135] H. Rumpf. Particle Technology. Chapman and Hall, New York. 1990.
- [136] Yakov I. Rabinovich, Joshua J. Adler, Ali Ata, Rajiv K. Singh, Brij M. Moudgil. Adhesion between Nanoscale Rough Surfaces I. Role of Asperity Geometry, Journal of Colloid and Interface Science. 232 (2000) 10–16.
- [137] Yakov I. Rabinovich, Joshua J. Adler, Ali Ata, Rajiv K. Singh, Brij M. Moudgil. Adhesion between Nanoscale Rough Surfaces II. Measurement and Comparison with Theory, Journal of Colloid and Interface Science. 232 (2000) 17–24.
- [138] Y. Lu. Fabrication of a Lotus Leaf-Like Hierarchical Structure to Induce an Air Lubricant for Drag Reduction, Surf Coat Technol. 331 (2017) 48–56.
- [139] Hans J. Ensikat, Petra Ditsche-Kuru, Christoph Neinhuis, Wilhelm Barthlott. Superhydrophobicity in Perfection: the Outstanding Properties of the Lotus Leaf, J. Nanotechnol. 2(2011) 152-161.
- [140] M. Götzinger, W. Peukert. Dispersive Forces of Particle-Surface Interactions: Direct AFM Measurements and Modelling, Powder Technol. 130(2003) 102-109.
- [141] J. N. Israelachvili. Intermolecular and Surface Forces 3rd ed. Academic Press, Boston 2011.
- [142] J. Lim, K. Hippalgaonkar, S. C. Andrews, A. Majumdar, P. Yang. Quantifying Surface Roughness Effects on Phonon Transport in Silicon Nanowires, Nano Lett. 12 (2012) 2475-2482.
- [143] Polina Prokopovich, Stefano Perni. Multiasperity Contact Adhesion Model for Universal Asperity Height and Radius of Curvature Distributions, Langmuir. 26 (22) (2010) 17028-17036.
- [144] Aditya Kumar, Thorsten Staedler, Xin Jiang. Role of Relative Size of Asperities and Adhering Particles on the Adhesion Force, Journal of Colloid and Interface Science. 409 (2013) 211-218.

- [145] Casey Q. LaMarche, Stuart Leadley, Peiyuan Liu, Kevin M. Kellogg, Christine M. Hrenya. Method of Quantifying Surface Roughness for Accurate Adhesive Force Predictions, *Chemical Engineering Science*. 158(2017) 140-153.
- [146] Tinh Nguyen, Bastien T. Pellegrin, Coralie Bernard, Xiaohong Gu, Justin M. Gorham, Paul E. Stutzman, Alexander J. Shapiro, Walter E. Byrd, Joannie W. Chin. Degradation and Nanoparticle Release of Nanocomposite Coatings Exposed to UV Radiation. *Coatings Science International*, (2010) 16-21.
- [147] ASTM D578/D578 M-05 (Reapproved 2011), Standard Specifications for Glass Fiber Strands, ASTM, West Coshohocken, PA, 2011.
- [148] J. Qiu, Y.B. Yi, X. Guo. Computational Prediction of Electrical and Thermal Conductivities of Disklike Particulate Composites. *International Journal of Computational Materials Science and Engineering* 4(3) (2015) 1-18.
- [149] K. Boyer, H. Chen, J. Chen, J. Qiu, R. Dewri. Characterization of the Mass Surveillance Potential of Road Traffic Monitors. *International Conference on Information Systems Security*. Springer, Cham, (2018) 3-23.
- [150] J. Qiu, Y.B. Yi. Random Walk Simulation Model of Diffusion in Circular and Elliptical Particulate Composites. *International Journal for Multiscale Computational Engineering* 16(2018) 131-142.
- [151] J. Qiu. Computational Prediction of Conductivities of Disk-Shaped Particulate Composites. University of Denver, 2014.
- [152] J. Qiu. Computational Modeling of Percolation Conduction and Diffusion of Heterogeneous Materials. University of Denver, 2017

Appendix: Acronyms and symbols

A-glass	Alkali-glass
AFM	Atomic force microscopy
C-glass	Chemical-glass
D-glass	Dielectric-glass
E-glass	Electrical-glass
ECR-glass	Electrical Corrosion Resistance-glass
FTIR	Fourier transforms infrared spectroscopy
GFRP	Glass fiber reinforced polymer matrix composite
GPC	Glass fiber-reinforced polymer composite
L-glass	Low-loss-glass
MMCs	Metal matrix composites
M-glass	Modulus-glass
PMCs	Polymer matrix composites
PEEK	Polyether ether ketone
RTV	Room temperature vulcanization silicone
R-glass	Resistance-glass
S-glass	Strength-glass
SEM	Scanning Electron Microscope
T-glass	Thermal-glass
UPE	Unsaturated polyesters
UV	Ultraviolet

VE	Vinyl esters
ZnO	Zinc oxide
PVC	Polyvinyl chloride
HDPE	High-density polyethylene
PC	Polycarbonate
UHMWPE	Ultra-high-molecular-weight polyethylene
PEEK	Polyether ether ketone